Lappeenranta
University of Technology

Marja-Leena Kääriäinen

ATOMIC LAYER DEPOSITED TITANIUM AND ZINC OXIDES; STRUCTURE AND DOPING EFFECTS ON THEIR PHOTOACTIVITY, PHOTOCATALYTIC ACTIVITY AND BIOACTIVITY

Thesis for the degree of Doctor of Science (Technology) to be presented with due permission for public examination and criticism in the Chamber Music Hall, Mikaeli Concert and Conference Hall, Mikkeli, Finland, on the 18th of June, 2013, at noon.

Acta Universitatis
Lappeenrantaensis 521

Supervisor Professor David Cameron
Advanced Surface Technology Research Laboratory
LUT Energy
School of Technology
Lappeenranta University of Technology
Mikkeli, Finland

Reviewers Professor Jaan Aarik
Institute of Physics
University of Tartu
Estonia

Professor Peter Kelly
Dalton Research Institute
Manchester Metropolitan University
UK

Opponent Professor Peter Kelly
Dalton Research Institute
Manchester Metropolitan University
UK

ISBN 978-952-265-424-3
ISBN 978-952-265-425-0 (PDF)
ISSN-L 1456-4491
ISSN 1456-4491

Lappeenranta University of Technology
Yliopistopaino 2013

ABSTRACT

Marja-Leena Kääriäinen

Atomic layer deposited titanium and zinc oxides; structure and doping effects on their photoactivity, photocatalytic activity and bioactivity

Lappeenranta 2013
74 pages
Acta Universitatis Lappeenrantaensis 521
Diss. Lappeenranta University of Technology
ISBN 978-952-265-424-3
ISBN 978-952-265-425-0 (PDF)
ISSN-L 1456-4491
ISSN 1456-4491

Titanium dioxide and zinc oxide are widely studied semiconductor materials with various useful properties and several applications. They both are photoactive, photocatalytically active, and antibacterial. Hence they can be used in self-cleaning surfaces, water and air purification, and bactericidal coatings against microbes. Atomic layer deposition (ALD) is a surface controlled gas phase chemical process. High quality nanometer films can be created since ALD provides pin-hole free conformal films with accurate thickness control.

The crystal structure and its modification by doping of TiO_2 and ZnO thin films have been studied in order to find out their effect on photoactivity, photocatalytic properties, and bioactivity. Atomic layer deposition was used to deposit titanium and zinc oxide thin films on glass and silicon substrates at various temperatures. Films with various film thicknesses were grown to investigate the changes in the polycrystalline structure. The effect of majority carrier polarity was examined in order to understand the photoactivity and photocatalytic nature of TiO_2. Zinc dissolution tests were performed in order to understand the mechanism in antibacterial effect. In addition the buffering effect of aluminum oxide on zinc release has been measured.

In TiO_2 studies the best photoactivity and photocatalytic activity was found at a 15 nm thickness where the anatase film contained a small fraction of rutile crystallites. The film thickness was found to be significant only because it had an effect on the anatase/rutile ratio. Based on the majority carrier polarity measurements the anatase or anatase-dominant films were found to be p-type whereas the rutile films were n-type. It was proposed that the superior photocatalytic property of anatase dominant films were due to the formation of p-n junctions in the TiO_2 which causes carrier separation and hence a reduction in recombination. Nitrogen doping was found to reduce the photoactivity especially in rutile dominant films. However the doping improved the photocatalytic activity significantly. The film resistivity measurements demonstrated that the doped TiO_2 series had higher conductivity than the undoped TiO_2 films.

Zinc release was found to take place from ALD grown ZnO films in deionized water and in phosphate buffered saline solution. ZnO films were found to be highly antibacterial in dark conditions needing no photoirradiation. It was suggested that the most important cause of the antibacterial effect is the influence of Zn^{2+} -ions. ALD grown Al_2O_3 film has proven to be an efficient buffer layer for zinc dissolution. The thickness of the Al_2O_3 layer can determine the onset of the bactericidal activity. These results also indicate that a multilayer nanolaminate structure of alternating ZnO and Al_2O_3 films could be used to tailor a complex sequence of high and low antibacterial activity which would be useful in medical applications

Keywords: titanium dioxide, zinc oxide, atomic layer deposition, photoactivity, photocatalytic activity, bioactivity

UDC 546.82/.83:546.47/.49:539.23:621.794

PREFACE

The research work for this thesis was carried out in the Advanced Surface Technology Research Laboratory (ASTRaL), LUT Energy, School of Technology, at Lappeenranta University of Technology.

My intention in the beginning of this work was to complete a one-year project with a popular photocatalyst, titanium dioxide. I figured it would be a nice and easy material to practice runs with our new and shiny ALD reactor. Since ALD technology made it simple to generate very thin films, and I had not seen a paper where a 3 nm thick TiO_2 film would have been deposited; I wanted to try to create a series of TiO_2 films with different thicknesses. Soon I realized I would be stuck with ALD deposited TiO_2 for years to come. Despite of thousands of articles written on TiO_2, researchers still seemed to know fairly little of TiO_2. In this work I tell you a tiny bit more. In addition, I will introduce another very interesting and trendy material, zinc oxide.

My deepest gratitude goes to my supervisor Prof. David Cameron. He is a true scientist and his valuable advice has made a great impact on this work. I would also like to express my gratitude to the reviewers of my thesis Prof. Jaan Aarik and Prof. Peter Kelly for their contribution and valuable comments.

I want to acknowledge Mr. Markku Heinonen from the Department of Physics and Astronomy at University of Turku for performing the XPS measurements. I also want to thank Mr. Michael Steiert at the Max Planck Institute for Polymer Research in Mainz for carrying out the ICP-OES measurements. I would also like to thank colleagues and co-authors at MPIP for collaboration and for allowing me to pay a research visit there.

Moreover I would like to acknowledge all collaborators in ASTRaL, at LUT, MAMK, and other universities. Special thanks for MUC and Miktech personnel for friendship and support. Many thanks to Beneq people for fruitful collaboration. I am grateful to Dr. Milja Mäkelä whose endless enthusiasm and passion for ALD and life in general inspired numerous moments during these years; we will always remember you.

Thanks for all my friends for fun and support. Thanks for Haidong Gumdo group for joyous moments on the path of sword.

I would like to thank my whole family for love and support. Especially I want to express my gratitude for my parents Hilkka and Sulo Kosonen. This thesis is dedicated for my mother who passed away in June 2012.

I am deeply grateful for my children Emil, Elsa, and Elias - you are so great and beautiful, and äiti loves you! My most loving thanks go to my dearest colleague and best friend, my husband Tommi – I love you.

Mikkeli, May 2013

Marja-Leena Kääriäinen

LIST OF PUBLICATIONS

The dissertation is based on the summary and following original three peer-reviewed publications and one manuscript referred in the text by the Roman numerals I-V.

I **M.-L. Kääriäinen**, T. Kääriäinen, D.C. Cameron, "TiO_2 thin films and doped TiO_2 nanolaminates, their structure and its effect on their photoactivity and photocatalytic properties", 50th Annual Technical Conference Proceedings, Society of Vacuum Coaters (2007), 335-339.

II **M.-L. Kääriäinen**, T.O. Kääriäinen, D.C. Cameron, "Titanium dioxide thin films, their structure and its effect on their photoactivity and photocatalytic properties", Thin Solid Films 517 (2009) 6666–6670.

III **M.-L. Kääriäinen**, D.C. Cameron, "The importance of the majority carrier polarity and p-n junction in titanium dioxide films to their photoactivity and photocatalytic properties", Surface Science 606 (2012) L22–L25.

IV **M.-L. Kääriäinen**, D.C. Cameron, "Nitrogen doping in atomic layer deposition grown titanium dioxide films by using ammonium hydroxide", Thin Solid Films 526 (2012) 212–217.

V **M.-L. Kääriäinen**, C.K.Weiss, S. Pütz, S. Ritz, D.C. Cameron, V. Mailänder, K. Landfester, "Zinc release from atomic layer deposited zinc oxide thin films and its bactericidal effect on *Escherichia Coli*", *Submitted to Applied Surface Science.*

The original publications are reprinted with the permission of the copyright holders.

AUTHOR'S CONTRIBUTION IN THE PUBLICATIONS

I The author performed the literature survey, most of the experimental and analysis work, and wrote the first manuscript of the paper.

II The author performed the literature survey, all the experimental and analysis work, and wrote the first manuscript of the paper.

III The author performed the literature survey, all the experimental and analysis work, and wrote the first manuscript of the paper.

IV The author performed the literature survey, all the experimental and analysis work excluding XPS measurements, and wrote the first manuscript of the paper.

V The author performed the literature survey, most of the experimental and analysis work excluding the ICP-OES measurements and antibacterial tests, and wrote the first manuscript of the paper.

OTHER PUBLICATIONS BY THE SAME AUTHOR

Related to the current field of study

M.-L. Kääriäinen, T.O. Kääriäinen, D.C. Cameron, M. Mäkelä, Structure of ALD grown transition metals and nitrogen doped TiO_2 nanolaminates and its effect on photoinduced hydrophilicity, BALD, Oslo, Norway, 19-20 June 2006.

M.-L. Kääriäinen, T.O. Kääriäinen, D.C. Cameron, Nitrogen doped ALD-grown titanium dioxide films, AVS 7th International Conference on Atomic Layer Deposition, San Diego, CA, 24-27 June 2007.

M.-L. Kääriäinen, T.O. Kääriäinen, D.C. Cameron, ALD-grown titanium dioxide thin films, their structure and its effect on their photoactivity and photocatalytic properties, MRS San Francisco, CA, 24-28 March, 2008.

M.-L. Kääriäinen, T.O. Kääriäinen, D.C. Cameron, Titanium dioxide thin films, their crystallinity and its effect on their photoactivity and photocatalytic properties, AVS 8th International Conference on Atomic Layer Deposition, Bruges, Belgium, 29 June- 2 July, 2008.

M.-L. Kääriäinen, T.O. Kääriäinen, D.C. Cameron Titanium Dioxide Thin Films, Their Structure and its Effect on their Photoactivity and Photocatalytic Properties, 52nd Annual Technical Conference Proceedings, Society of Vacuum Coaters Santa Clara, CA, May 9–14, 2009, 461-466.

M.-L. Kääriäinen, T.O. Kääriäinen, D.C. Cameron, The synergy between anatase and rutile phase in the photocatalytically active titanium dioxide films, AVS 9th International Conference on Atomic Layer Deposition, 19-22 July, Monterey, CA, 2009.

S. Vilhunen, M. Bosund, **M.-L. Kääriäinen**, D. Cameron, M. Sillanpää, Separ. Sci. Technol. 66 (2009) 130.

M.-L. Kääriäinen, D.C. Cameron, Mechanism for enhancement of photocatalysis in nitrogen doped titanium dioxide thin films grown by atomic layer deposition, 12 September, PSS, MMU, Manchester, UK, 2011.

M.-L. Kääriäinen, D.C. Cameron, The importance of majority carrier polarity and p-n junction in titanium dioxide films to their photoactivity and photocatalytic properties, 55th Annual Technical Conference Proceedings, Society of Vacuum Coaters, Santa Clara, CA April 28–May 3, 2012, 278-282.

Other publications

T.O. Kääriäinen, **M.-L. Kääriäinen**, R.P. Gandhiraman, D.C. Cameron, Atomic layer deposition of TiO_2 films at low temperatures using tetrakis-dimethyl-amido-titanium and ozone, AVS 7th International Conference on Atomic Layer Deposition, 24-27 June, San Diego, CA, 2007.

G. Natarajan, O. Kilpelä, **M.-L. Kääriäinen**, D.C. Cameron, Influence of growth parameters and post annealing on the electrical properties of atomic layer deposited SnO_2 films, AVS 7th International Conference on Atomic Layer Deposition, 24-27 June, San Diego, CA, 2007.

T.O. Kääriäinen, **M.-L. Kääriäinen**, D.C. Cameron, Plasma-assisted atomic layer deposition of oxides at low temperature: growth characteristics and interaction between plasma and polymer substrate, AVS 9th International Conference on Atomic Layer Deposition, 19-22 July, Monterey, CA, 2009

T.O. Kääriäinen, P. Maydannik, **M.-L. Kääriäinen**, D.C. Cameron, P. Johansson, K. Lahtinen, J. Kuusipalo, Continuous Atomic Layer Deposition Process, 15th Technology Summit & Technology Platform, 26-27 November, New Delhi, India, 2009.

T.O. Kääriäinen, S. Lehti, **M.-L. Kääriäinen**, D.C. Cameron, Optimization of Plasma Characteristics in Plasma-Assisted Atomic Layer Deposition: Effect on Film Structure and Process Enhancement Prospects 54th Annual Technical Conference Proceedings, Society of Vacuum Coaters, Chicago, IL 16-21 April 16–21, 2011, 357-361.

T.O. Kääriäinen, S. Lehti, **M.-L. Kääriäinen**, D.C. Cameron, Surf. Coat. Tech. 205 (2011) S475.

P. Jalkanen, S. Kulju, L. Antila, P. Myllyperkiö, T. Ihalainen, T. Kääriäinen, **M.-L. Kääriäinen**, J. Korppi-Tommola, Thin Solids Films 519 (2011) 3835.

T.O. Kääriäinen, **M.-L. Kääriäinen**, D.C. Cameron, New Design and operation of Photon Energy Source for the Low Temperature Atomic Layer Deposition Process; Deposition of TiO_2 on Polymer Substrates, 55th Annual Technical Conference Proceedings, Society of Vacuum Coaters Santa Clara, CA, April 28–May 3, 2012, 85-88.

T. Ivanova, T. Hoder, **M.-L. Kääriäinen**, D.C. Cameron, Enhancement of VOC removal from air by combining atmospheric plasma and photocatalytic porous dielectric coated by atomic layer deposition, 13th International Conference on Plasma Surface Engineering, Garmisch-Partenkirchen, Germany, September 10-14, 2012.

TABLE OF CONTENTS

ABSTRACT 3

PREFACE 5

LIST OF PUBLICATIONS 7

AUTHOR'S CONTRIBUTION IN THE PUBLICATIONS 8

OTHER PUBLICATIONS BY THE SAME AUTHOR 9

TABLE OF CONTENTS 11

NOMENCLATURE 13

1. Introduction 15

1.1 Titanium Dioxide 16

1.2 Zinc Oxide 18

1.3 The fabrication of thin films by atomic layer deposition (ALD) 18

2. Structure and Properties of TiO_2 and ZnO and their deposition by ALD 19

2.1 Structure of TiO_2 19

2.1.1 Surface structure of TiO_2 23

2.1.2 Water on TiO_2 surface 26

2.2 Electrical properties of TiO_2 28

2.3 ALD grown TiO_2 thin films 29

2.4 Photoactivity and photocatalytic properties of TiO_2 30

2.4.1 Nitrogen doping of TiO_2 35

2.4.2 Nitrogen doping in ALD-grown thin films 39

2.5 Structure of ZnO 39

2.6 Properties of ZnO 41

2.7 ALD grown ZnO thin films 42

3. Experimental methods 45

3.1 Film deposition 45

3.2 Film characterization 46

3.2.1 Film thickness 46

3.2.2 X-ray diffraction (XRD) 46
3.2.3 Scanning electron microscopy (SEM) 47
3.2.4 Atomic force microscopy (AFM) 47
3.2.5 X-ray photoelectron spectroscopy (XPS) 48
3.2.6 UV-Vis spectroscopy 48
3.2.7 Band gap evaluation 48
3.2.8 Electrical measurements 49
3.3 Photoactivity and Photocatalytic measurements 49
3.3.1 Contact angle measurement 49
3.3.2 Methylene blue degradation test 50
3.4 Antibacterial studies 50
3.4.1 Bacterial attachment 50
3.4.2 Antibacterial activity 51
4. Results and Discussion 51
4.1 The effect of film thickness and structure on TiO_2 photoactivity and photocatalytic properties 52
4.2. The effect of majority carrier polarity on photoactivity and photocatalytic activity of TiO_2 films 54
4.3 Nitrogen doping of ALD grown TiO_2 films 56
4.4 Zinc release from ALD-grown ZnO thin films and its bactericidal effect on *Escherichia Coli* 57

5. Conclusions 60
References 63

NOMENCLATURE

Abbreviations

AFM	Atomic force microscopy
ALD	Atomic layer deposition
CFU	Colony forming unit
CSP	Crystallographic shear plane
CVD	Chemical vapor deposition
DEZ	Diethyl zinc
ICP-OES	Inductively coupled plasma mass spectroscopy
MB	Methylene blue
PBS	Phosphate buffered saline
PEALD	Plasma enhanced atomic layer deposition
PVD	Physical vapor deposition
R	Bacteria reduction
RBS	Rutherford backscattering spectroscopy
RRALD	Roll-to-roll atomic layer deposition
SEM	Scanning electron microscopy
SHE	Standard hydrogen electrode
STM	Scanning tunneling microscopy
TFEL	Thin film electroluminescent display
XPS	X-ray photoelectron spectroscopy
XRD	X-ray diffraction
XRF	X-ray fluorescence

List of symbols

α	Absorption coefficient
c	Speed of light
e^-	Electron
E_F	Fermi level
E_g	Band gap
E_{cb}	Conduction band
E_{vb}	Valence band
h	Planck's constant
h^+	Hole
$h\nu$	Photon energy
λ	Wavelength
ν	Frequency
O_i	Interstitial oxygen
O_v	Oxygen vacancy
Zn_i	Interstitial zinc
Zn_o	Zinc antisite

1. Introduction

Due to their multiple applications and variety of properties titanium and zinc oxide have been among the most scrutinized materials. Metal oxides have been manufactured and investigated widely by atomic layer deposition (ALD). Accordingly, the number of studies of ALD grown titanium dioxide (TiO_2) and zinc oxide (ZnO) have been increasing during the last decade. High quality nanometer films can be created since ALD provides pin-hole free films with accurate thickness control and conformality.

TiO_2 has been especially popular due to its photoactivity and photocatalytic activity. Most of the studies have been carried out with various particles but investigation of films has been rising rapidly. The comparison between the research results has been difficult due to the multiple production methods which provide materials with variable quality. The most common requirements for the high performance of a photocatalytic TiO_2 material have been claimed to be high surface area or adequate film thickness without mentioning the quality of the material. Despite the fact that TiO_2 has several polymorphs and multiple crystal orientations it has been often discussed as one similar material. Nevertheless some investigations have generated valuable knowledge on the atomic and crystalline structure of TiO_2. Surface properties and functions of the TiO_2 polymorph rutile and recently also anatase have been modeled. This has provided important information in understanding photoactivity and photocatalytic activity in various environments.

ZnO has been long known for its bactericidal effect. Alike with TiO_2 much of the research has been performed with particles or powder ZnO but lately numerous studies have been performed on films. The mechanism for antibacterial behavior is still unknown and several theories have been proposed. The emergence of nanotechnology has brought new aspects to the research studies since nanomaterial has been discovered to behave differently from bulk ZnO. Subsequently surface and crystal structure of ZnO and their effect on the antibacterial properties needs more understanding.

The aim of this work has been to create various TiO_2 and ZnO thin films with ALD processes in order to understand the effect of film structure in photoactivity, photocatalytic activity, and bioactivity. The effect of film thickness in the growth of TiO_2 and ZnO films has been

scrutinized. The anatase-rutile ratio in TiO_2 and its effect in photoactivity and photocatalytic properties has been investigated. The influence of majority carrier polarity has been examined in order to understand the photoactivity and photocatalytic nature of TiO_2. The nitrogen doping effect on the structure and properties of TiO_2 has been investigated. ZnO films have been applied in dissolution examinations in order to understand the zinc release from the films. Additionally ZnO has been coated with various thicknesses of ALD grown aluminum oxide. The buffering effect of aluminum oxide in zinc release has been measured. Finally antibacterial studies were performed with ZnO films.

1.1 Titanium Dioxide

Titanium dioxide is an extensively investigated material due to its vast variety of practical features. TiO_2 possesses good chemical and physical stability and it is insoluble in water, hydrochloric, nitric, and diluted sulfuric acid. It dissolves slowly in hydrofluoric acid and hot concentrated sulfuric acid [1]. Due to its inertness and high refractive index it is the most widely used pigment to give whiteness and opacity for paints, pastes, coatings, cosmetics, food, and medicine. In addition TiO_2 is a semiconductor possessing high dielectric constant and good transmission in the visible range which is why it can be used in multiple optical and sensing applications. The most common polymorphs of TiO_2 are rutile and anatase. The band gaps of rutile and anatase are 3.0 eV and 3.2 eV, respectively. Titanium dioxide is also photocatalytic. This property was realized already in 1930s but only a few research articles were produced during the next three decades [2-6]. In paints the phenomenon was recognized as a *chalking* problem caused by UV light which in the present of TiO_2 degrades the polymer binder in the paint. It was not until 1972 when photocatalytic TiO_2 received further attention due to the discovery of splitting of water by Fujishima and Honda [6]. Consequently titanium dioxide's photocatalytic properties, mechanisms, and surface reactions have been under extensive scrutiny until today [7-12].

Titanium dioxide's characteristic as a superhydrophilic coating was discovered in 1995 [13,14] which excited the research and increased the number of applications of photocatalytic and photoactive TiO_2 especially in Japan. In environmental purposes TiO_2 coatings and particles have been utilized in self-cleaning, anti-fogging, and antibacterial surfaces [15-17].

In applications such as indoor and outdoor construction cements, ceramic tiles, and windows, titanium dioxide's function has been to reduce fouling and decompose pollutants such as volatile organic compounds and nitrogen oxides [15,16]. Antibacterial properties make it also potentially useful in hospitals, bathrooms and places where microbes cause problems. During the last two decades TiO_2 has been comprehensively studied in waste water and air purification, in dye sensitized solar cells [18,19], gas sensors, optical applications, and microelectronics [20-39].

Since nanotechnology started to develop, TiO_2 has been fabricated in various forms such as different nanoparticles, nanorods, nanowires, and nanoscale thin films [40]. The definition for a nanoscale material is that at least one of its dimensions is sized from 1 – 100 nm. There are multiple methods to fabricate nanosized TiO_2 such as sol-gel, hydrothermal method, direct oxidation method, chemical vapor deposition (CVD), physical vapor deposition (PVD), and atomic layer deposition (ALD) to name a few.

Nanometer scale has changed the research work and applications since new physical and chemical properties have appeared. For instance in semiconductor materials such as TiO_2, movement of electrons and holes has been found to be affected by quantum confinement. Also the size and shape of the material have an effect on the transport of photons and phonons. The band gap (E_g) of TiO_2 has been noticed to increase when the grain size reaches a certain critical value [41]. This occurs due to the quantum confinement effect which takes place when the diameter of the grain equals the magnitude of the wavelength of the electron wave function. Yet, there are disagreements on the critical grain size or whether the quantum size effect applies to TiO_2 [42-45]. Additionally, specific surface area and surface-to-volume ratio in nanomaterials is radically larger than in the bulk. These both result in an increased number of excitons and chemical reactions on the TiO_2 surface which further can enhance the efficacy of photocatalytic activity. A negative aspect of nanoparticulates is their biological toxicity if they get into human cells [46]. In water and air purification there is a risk that nanoparticles remain in the filtered product. Nanoparticulates may also penetrate through skin from cosmetics, medical or self-cleaning products [46]. A non-toxic option is to use TiO_2 solid thin films which have been deposited onto various supports where surface area can be increased by using porous materials as substrates.

1.2 Zinc Oxide

Zinc oxide, ZnO, is an inorganic compound. Typically ZnO is a white powder that is insoluble in water. It is commonly used as an additive in numerous materials and products including pigments, plastics, ceramics, glass, cement, lubricants, paints, adhesives, and in foods as a source of Zn mineral [47]. In nature ZnO can be found as zincite mineral. However, most of the zinc oxide is produced synthetically.

In materials science ZnO is a direct wide band gap semiconductor. Its band gap is 3.37 eV and close to that of TiO_2. In fact the characteristics of TiO_2 and ZnO are similar. Like TiO_2 ZnO is also photoactive and bactericidal hence it can be applied in air and water purification and in medical applications [48-50]. ZnO has a good transparency, high electron mobility, and a strong room-temperature luminescence. Thus it has many applications in optical, electronic and optoelectronic devices such as thin-film transistors, light-emitting diodes, transparent conductors in liquid crystal displays and solar cells and gas sensors [51-60]. It addition ZnO can be used in heat blocking and/or energy saving windows, and in surface acoustic wave devices [61-63]. Since ZnO also possesses a high refractive index of 2.0 and absorbance in the UV region it can be used as a UV-blocker.

1.3 The fabrication of thin films by atomic layer deposition (ALD)

The concept of the Atomic Layer Deposition (ALD) process was first published by Prof. V.B. Aleskovskii in the Soviet Union in 1950s [64]. The actual invention and the first patent for ALD technology was launched by Prof. Tuomo Suntola and his coworkers in the 70s in Finland [65]. Their work led to the first industrial application, the manufacturing of thin film electroluminescent (TFEL) flat-panel displays starting from the mid 80s. Interest in ALD has increased gradually thereafter and in the 2000s the first noble metals were deposited with ALD keeping the focus on silicon-based electronics. During recent years ALD has been applied in preparation of various passivation and buffer layers for solar cells and anti-tarnishing layers for silver products. ALD is also a potential technology in flexible plastic displays, organic LEDs, flexible and paper-based electronics and high performance packaging in creating barrier layers against water vapor and oxygen diffusion. The development of roll-

to-roll processes (RRALD) is essential for economic production of active flexible devices [66].

ALD is a surface controlled gas phase chemical process where thin films can be deposited in a layer by layer manner [67]. Typically, in the growth of binary compounds such as metal oxides, a reaction cycle consists of two reaction steps. However during the initial pulse, chemisorption is needed to occur between the first precursor and the substrate surface. Usually the first precursor is an oxidizing precursor which forms hydroxyl groups on the surface. In the second step the metal precursor reacts with the hydroxyl groups and the first layer of metal oxide is formed. Between the steps a purge gas, usually nitrogen or argon, is applied to remove the excess of precursor and the reaction by-products and only those atoms or molecules which remain on the surface will react. Hence the film growth in Atomic Layer Deposition is self-controlled contributing several advantages. The thickness of the films can be controlled by controlling the number of reaction cycles, therefore enabling the controlled growth of ultra thin layers. The growth control can be as fine as ~0.01 nm per cycle. The precursors form stoichiometric films with large area uniformity and conformality even on complex surfaces with deformities. Layer-by-layer growth allows one to change the material abruptly after each step. This gives the possibility of depositing multicomponent films such as nanolaminates or mixed oxides. ALD can be used to deposit several types of thin films, including various oxides, nitrides, sulfides, metals, and hybrid organic-inorganic layers aka *metallocones* [68-71].

2. Structure and Properties of TiO_2 and ZnO and their deposition by ALD

2.1 Structure of TiO_2

In nature TiO_2 is typically found in ilmenite ($FeTiO_3$) but also as naturally occurring rutile. TiO_2 is refined from ilmenite in a sulfate process and from rutile ore in a chloride process. In addition TiO_2 can be manufactured into different types of particles and films by applying

various techniques [72]. The most common minerals of titanium dioxide are rutile (tetragonal), anatase (tetragonal), and brookite (orthorhombic). From these three, rutile is the most stable polymorph exhibiting the highest refractive index. Anatase and brookite are metastable and transform irreversibly into rutile at elevated temperatures. Brookite is a rare mineral compared to rutile and anatase. It is also much more difficult to fabricate. All the most common polymorphs of TiO_2 rutile, anatase, and brookite are birefringent ie. double refractive. The refractive indices of rutile are n_o=2.61 and n_e=2.90. For brookite they are n_o=2.58 and n_e=2.70 hence both are optically positive. Anatase is optically negative and possesses refractive indices of n_o=2.56 and n_e=2.49 [72].

Rutile and anatase have been the most studied polymorphs in TiO_2 applications. They both possess a tetragonal crystal structure. The unit cell parameters for rutile are a = b= 0.4584 nm, c = 0.2953 nm and for anatase a = b= 0.3782 nm, c = 0.9502 nm. The bulk structure of rutile and anatase consists of titanium atom surrounded by an octahedron of 6 oxygen atoms. In both structures the octahedral configuration is slightly distorted. Anatase possesses a more noticeable deviation from 90° between Ti-O –bonds than rutile [73]. In rutile each octahedron is sharing a corner with a neighbor along the [110] direction and they are stacked with their [010] axis alternating by 90°. In anatase the octahedra that are sharing corners form the (001) plane. The unit cells with octahedral structures of rutile and anatase are shown in Figure 1.

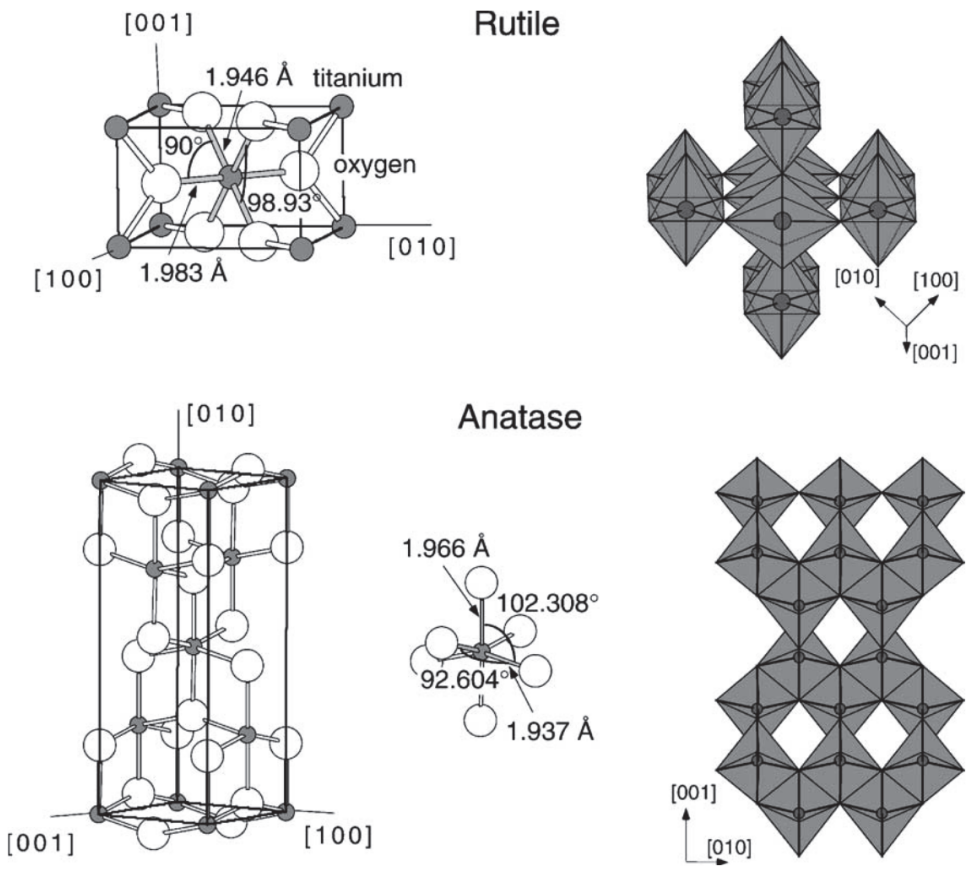

Figure 1. Bulk structures of rutile and anatase unit cell structure (left). Stacking of octahedral structures is shown on the right [74]. *Reprinted with permission from Elsevier © 2003*.

Of all the TiO_2 surfaces rutile (110) surfaces are thought to possess the highest thermodynamic stability. In anatase the (101) surface is thermodynamically most stable [74]. In surface science the rutile (110) surface has been widely studied and it has become a prototypical surface among metal oxides [75,76]. However, in the late 1990s comparatively small numbers of studies were conducted on the anatase structure despite its technological importance. The lack of knowledge was mainly due to lack of appropriate single-crystal samples. In nature the rutile mineral is found in high-temperature and high-pressure metamorphic and igneous rocks [77]. The rutile mineral is presented in Figure 2. The anatase phase of TiO_2 is formed at lower temperatures than rutile. Many double pyramid anatase

crystals have been found in St Christophe-en-Oisans, France. Microscopic sized crystals can be found in sedimentary rocks, such as sandstones, clays, and slates. A second type anatase mineral has numerous pyramidal faces and has been discovered in the Alps [78]. A double pyramid anatase mineral is presented in Figure 3.

Figure 2. Rutile mineral crystal from Binn Valley, Wallis (Valais), Switzerland. (110) plane is marked [77]. *© Rob Lavinsky, iRocks.com – CC-BY-SA-3.0*

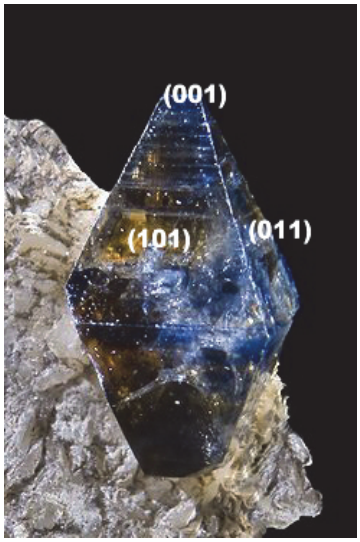

Figure 3. Anatase mineral crystal from St Christophe-en-Oisans, Rhône-Alpes, France. Typical cleavages of (101) and (011) on the sides and (001) on top are shown [78]. © *Didier Descouens, Creative Commons Attribution 3.0 Unported license.*

2.1.1 Surface structure of TiO_2

Accurate surface studies need pure single-crystalline materials. Rutile is a common mineral and its (101) face has become the most investigated single-crystalline surface in the surface science of metal oxides. The bulk-truncated (1x1) surface has been well scrutinized both with experimental and theoretical methods [73,74]. The stoichiometric characteristics as well as defects have been studied since they all affect the surface chemistry of TiO_2 [79,80].

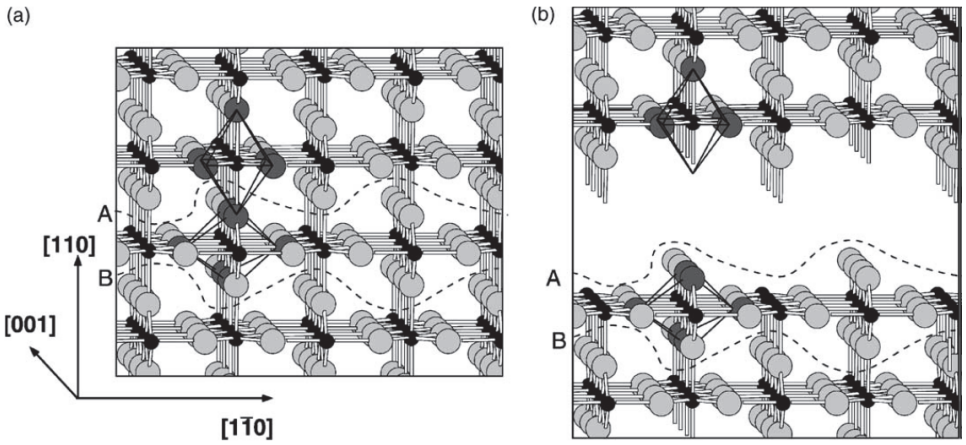

Figure 4. A bulk-terminated rutile surface [74]. *Reprinted with permission from Elsevier ©2003.*

A bulk-terminated rutile surface structure is presented in Figure 4 [73]. Six-fold coordinated and five-fold-coordinated Ti atoms alternate along the [001] direction. Two dissimilar oxygens are bonded to Ti atoms. The oxygen atoms on the main surface are three-fold-coordinated as in the bulk. So called bridging oxygens are only two-fold-coordinated and due to their undersaturation they are prone to be removed by thermal annealing. The oxygen loss can further cause bulk oxygen vacancies and titanium interstitials in the bulk [74]. The effect can ultimately lead to a defect called a crystallographic shear plane (CSP) [74]. The CSP is formed when a normally edge-sharing octahedra is transformed into a face-sharing arrangement. Other common defects are step edges and impurities. Steps edges may be adsorption sites for molecules or nucleating locations for metals when deposited on oxides [73,74,81-83]. Yet step-edges have not been found to play a major role in affecting surface chemistry. [73]. Impurities have been found to segregate to the surface when TiO_2 is annealed in high temperatures [84]. The quantity and quality of impurities vary in crystalline specimens since they are dependent on the synthesis and manufacturing methods.

Figure 5 presents a scanning tunneling microscopy (STM) image of TiO_2 (110) surface point defects [85]. The investigators suggested that the bright defects were oxygen vacancies. The dark point defects were unknown to the investigators.

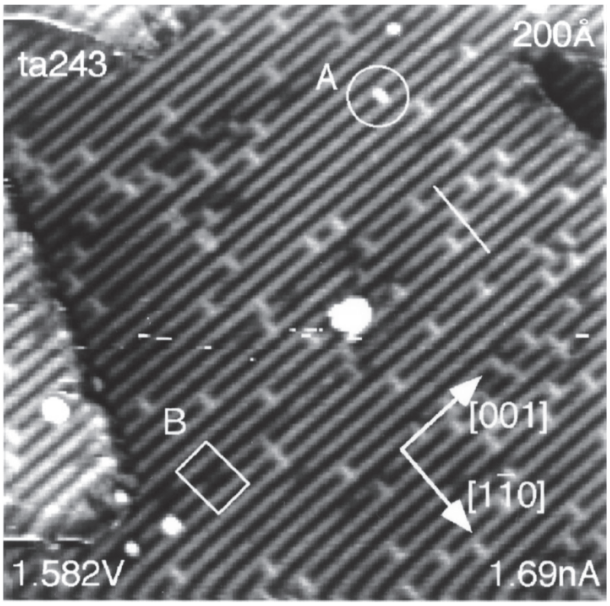

Figure 5. STM image of 200Åx200Å of a TiO_2 surface. Point defects are marked with an "A" and "B". Points with "A" have been assigned as oxygen vacancies [85]. *Reprinted with permission from Elsevier © 1998.*

Anatase is a rarer TiO_2 mineral than rutile. Pure anatase crystals have been hard to acquire in order to execute accurate surface studies. However due to the growing interest in highly photoactive anatase its surface properties have been under scrutiny during the last decade [74]. Anatase (101) has been found to possess the highest thermodynamic stability [86-88,74]. Based on *ab initio* density-functional calculations Lazzeri *et al.* [89,90] found that the anatase (101) surface is corrugated with a characteristic sawtooth profile perpendicular to the [010] direction. The first STM study of single-crystalline anatase was performed by Hebenstreit *et al.* [91]. A ball-stick model of anatase (101) and a STM image of a characteristic terrace-step structure of anatase (101) are presented in Figure 6.

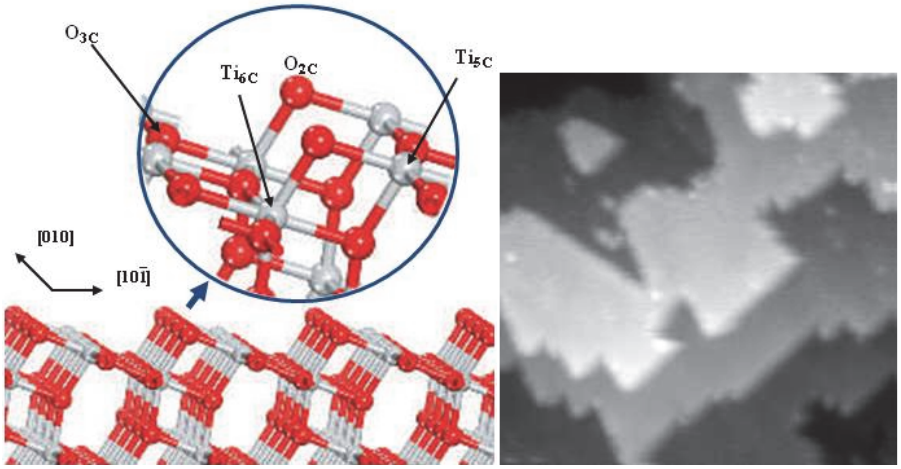

Figure 6. Ball-stick –model of anatase (101) (left) and a scanning tunneling microscopy (STM) image of terrace-step structure of anatase (101) (right) [92]. *Reprinted with permission from the Nature Publishing Group © 2006.*

The left image of the Figure 6 presents a ball-stick model of the anatase (101) surface showing fully coordinated six-fold titanium atoms (Ti_{6C}) bonded to three-fold oxygen atoms (O_{3c}) and undercoordinated five-fold titanium atoms (Ti_{5C}) bonded to two-fold-coordinated bridging oxygen atoms (O_{2C}). The STM image in Figure 6 (right) shows the characteristic terrace-step structure of anatase (101) [92].

In contradiction to what had been earlier thought, Lazzeri *et al.* [89,90] reported that anatase is more stable than rutile and the difference in cohesive energy between the two phases was calculated to be 0.10 eV/TiO_2. Based on the calculations of Beltran *et al.* the cohesive energy of anatase was approximately 0.14 eV/TiO_2 higher than that of rutile's [93].

2.1.2 Water on TiO_2 surface

The rutile TiO_2 (110) -water interface is the most widely studied model system. Rutile has been found to be reduced more easily with H_2 or vacuum annealing than anatase [94]. Schaub *et al.* studied water on rutile (110) surface with STM imaging and DFT calculations [95]. They discovered that water eagerly dissociates on oxygen vacancies (O*v*) to form pairs of

nearby bridging hydroxyl (OH) groups. The adsorption of water was found to be different on anatase (101) surfaces. Based on DFT calculations Vittadini *et al.* presented that water adsorbs molecularly on anatase (101) surfaces [96]. The adsorption energy for undissociative water molecules on anatase (101) was found to be ΔH_{H2O} ~0.7 eV whereas the same for dissociative water was $\Delta H_{H,OH}$ ~0.3 eV. This result was in agreement with the experimental estimate of 0.5-0.7 eV by Egashira *et al.* [97]. The investigators considered this as proof that molecular adsorption is mostly favored on anatase (101). Further STM studies of anatase (101) showed that anatase has a much smaller defect density than rutile (110) [91]. The same result was obtained later in another study [98]. The investigators concluded that the major difference between rutile and anatase was related to the difficulty in forming oxygen vacancy defects on anatase (101) as opposed to forming them on rutile (110). Since the defect sites cannot be formed on anatase (101) the adsorbed water is assumed to remain molecular.

Yet there is still a controversy whether water is dissociative even on rutile (110). According to recent studies that were conducted using DFT calculations water does not dissociate on rutile (110) within the 0.5 monolayer to multilayer regime [99]. The investigators defined one monolayer as equal to one water molecule per five-fold coordinated Ti site. The first contact layer of water on TiO_2 was found to contain slow moving water molecules whereas the second layer moved faster. The investigators found hydrogen bonding between the first and second layer molecules. In addition the first and second layer molecules were able to exchange positions between the layers.

The general understanding has been that hydroxyl radicals formed from water molecules by holes have an important role in photocatalytic reactions. However some studies have emphasized the role of oxygen. It has been suggested that oxygen (O_2) would not adsorb onto neutral TiO_2 [100-102]. Its adsorption seems to need a negatively charged surface for instance a defect site such as an oxygen vacancy. Based on recent DFT calculations Muhich *et al.* proposed that O_2 adsorption and the resulting highly oxidative species would be the major factor in the degradation of pollutants [103]. They suggested that water molecules would only serve as hole acceptors and ultimately not be involved in degradation processes.

2.2 Electrical properties of TiO_2

Unlike metals which have continuums of electronic states; semiconductors have a void region between the filled valence band and the vacant conduction band where (in principle) no electron can exist. This region is called a band gap. TiO_2 is a semiconductor with band gaps of 3.2 eV for anatase and 3.0 eV for rutile. The greater band gap of anatase is assumed to result from a lower material density which causes weaker bonding and less band dispersion. Anatase is also found to possess an indirect bandgap where rutile has a direct band gap [104].

Investigators have found significant differences between the electrical properties of anatase and rutile. Sputtered anatase and rutile films were studied by Forro *et al.* [105]. They found that anatase films possessed low donor levels and high electron mobility. Confirmed by another study, anatase possessed a smaller electron effective mass and shallower donor energies than rutile [106]. Additionally the exciton states were found to be self trapped on anatase while in rutile they were free.

DFT calculations were performed on the electron transport in stoichiometric anatase and rutile phases [107]. In contrast with the earlier studies [105] Deskins and Dupuis found that intrinsic electron transfer was faster in bulk rutile compared to bulk anatase. The differences between the studies may be due to defects, applied voltage, or photoexcitation which can have an effect on the mobility of charge carriers. Later the same investigators reported that holes are thermodynamically more stable in the rutile phase, while electrons are more stable in the anatase phase [108].

The charge carrier type of TiO_2 has been also under scrutiny. Generally TiO_2 has been found to be n-type and this behavior has been observed both in rutile and anatase structures [109,110]. There are a few contradictory results where n-type anatase and p-type rutile have been fabricated from titania powder [111] or p-type anatase that was made by sol-gel technique to be tested in gas sensors [112]. In another study anatase was reported to change its polarity depending on the energy of light irradiation [113]. The conductivity of TiO_2 depends on its polymorph and impurities. It can be modified by doping or by oxygen vacancies. In various vacuum techniques oxygen vacancies may be created by decreasing the partial pressure of the oxidizing agent [114] or post annealing can be performed to reduce

TiO_2 with hydrogen [115]. It has been discovered that electrical conductivity is not that dependent on the intrinsic free carriers in TiO_2 but that conductivity occurs mostly due to hopping through impurity centers [116]. The conductivity has also been found to be affected by the grain size in TiO_2 thin films which has been noticed to increase with increasing deposition temperature [117]. Accordingly minor changes in TiO_2 structure may significantly change its electrical properties.

2.3 ALD grown TiO_2 thin films

TiO_2 films have been created by various ALD processes. Halides, alkoxides, alkylamides, and heteroleptic precursors have been used within a temperature range of 100-600°C [118-147]. Using plasma-enhanced (PEALD) processes a temperature range as low as 50-70°C has been applied [148]. However in order to achieve crystalline TiO_2 films a temperature above 200°C has been required in ALD processes [141,142]. TiO_2 ALD-processes have been discussed recently more comprehensively elsewhere [71,149]. The most common halide process is presented in the following section.

Titanium tetrachloride ($TiCl_4$) has been a typical precursor for TiO_2 due to its good volatility, reactivity with water, inexpensiveness, and stability.

For the tetrachloride and water process the basic reaction mechanism is the following

$$TiCl_4\ (g) + 2\ H_2O\ (g) \rightarrow TiO_2\ (s) + 4\ HCl\ (g) \qquad (1)$$

Various reaction temperatures have been investigated with this process. One of the first studies applied a temperature range of 150-600°C with Corning 1733 glass as a substrate [118]. The growth rates varied between 0.035-0.045 nm/cycle depending on the deposition temperature. A growth rate of 0.052 nm/cycle at 500°C was achieved when using soda lime glass as a substrate. The residual chlorine analyzed by Rutherford Backscattering Spectrometry (RBS) was found to be 2 at-% at 150°C but was beyond the detection limit for 500°C deposited films. For an unknown reason the investigators did not succeed in depositing crystalline films on glass substrates. During the following years, studies showed that ALD

grown crystalline TiO_2 was possible to be deposited on amorphous substrates [121]. Aarik *et al.* confirmed that all the films above 165°C were crystalline and below 165°C, amorphous. Anatase appeared in all films between 165-350°C and rutile started to grow above 350°C becoming the dominating phase around 400°C. Another important observation was that the crystal phase and orientation depended on the film thickness. At 210°C the films were amorphous below a thickness of 10 nm whereas they were polycrystalline between 15-55 nm thicknesses. In addition the minimal film thickness when the crystallization started to appear decreased with increasing temperature. The growth and transformations of TiO_2 phases in thin films have not been scrutinized very intensively. In particle research there are several studies on the effect of size to the structure and various characteristics of TiO_2 [88,150-152]. Anatase to rutile transformation has been related to the grain size of TiO_2. Based on thermodynamical and experimental studies with nanoparticles, anatase was found to be most stable below a particle size of circa 14 nm [150]. In a later study where the transformations of three polymorphs (anatase, brookite, and rutile) were compared, anatase was thermodynamically most stable at sizes less than 11 nm [151].

In ALD deposition the transformation from anatase to rutile seems to occur around 350 °C [121]. Apparently the thin film thickness and the grain size of the grown crystalline film can affect the transformation between TiO_2 phases and crystal orientation.

2.4 Photoactivity and photocatalytic properties of TiO_2

Photoactivity is utilized in self cleaning surfaces and in dye-sensitized solar cells whereas photocatalytic activity is important in processes where the degradation of organic molecules is required. TiO_2 is a well accepted photocatalyst since it is inexpensive, chemically stable, and the photogenerated holes are highly oxidizing. Both anatase and rutile have proven to be photoactive and possess photocatalytic properties, but based on numerous investigations anatase has overcome rutile in both properties. The downsides of TiO_2 are recombination problems and its functionality in a narrow solar range. As mentioned already in Chapter 2.2 the bandgap of bulk anatase is E_g=3.2 eV, which corresponds to a wavelength of 388 nm whereas the bandgap of rutile is E_g=3.0 eV which is equivalent to 414 nm. Consequently anatase needs more energy for activation and both polymorphs absorb only UV light therefore being photoreactive only within 4% of the solar energy range. In addition TiO_2 suffers from

fast recombination of electrons and holes during the photoactivation which reduces its efficiency in both photoactivity and as photocatalytic material. A good understanding of photoactive materials' structure and electron/hole transport is essential to improve efficiency of photocatalytic reactions. There have been multiple attempts to decrease the recombination problem and to extend the narrow solar absorption range to visible region.

The photocatalytic process is presented in Figure 7. TiO_2 photoexcitation takes place when an electron (e^-) is excited by photon energy (hν) from valence band (VB) to conduction band (CB) and a hole (h^+) is formed into the valence band. After excitation there are several options that can occur [10]: the electron and the hole can recombine dissipating the input photon energy to heat, become trapped in metastable semiconductor surface states, or they can interact with electron donors and acceptors that are adsorbed on the TiO_2 surface. The recombination occurs in a few nanoseconds [153] if there is lack of scavengers that could trap the electrons or the holes. A trapped electron from the conduction band is a good reductant and a hole from the valence band is an outstanding oxidant enabling redox reactions to take place.

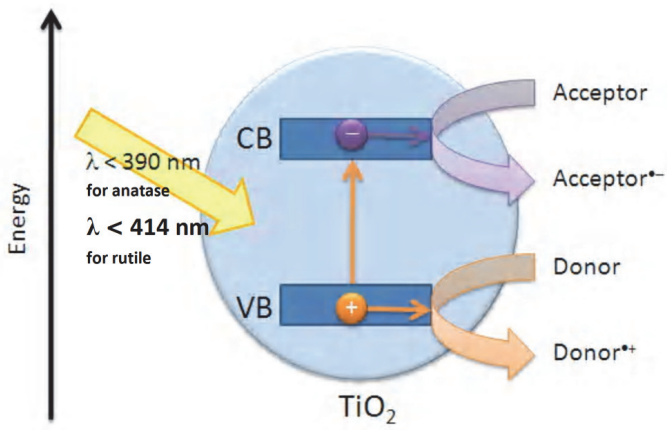

Process	Name
$TiO_2 + h\upsilon \rightarrow h_{VB}^+ + e_{CB}^-$	Charge Separation
$h_{VB}^+ + H_2O \rightarrow OH^\bullet$	$OH^\bullet$ Generation (VB)
$e_{CB}^- + O_2 \rightarrow O_2^{\bullet-} + H_2O \rightarrow OH^\bullet$	$OH^\bullet$ Generation (CB)

Figure 7. Schematic of photocatalytic process and the oxidative reactions [154]. *Adapted from Photochemistry Portal, Creative Commons Attribution-Non-Commercial-Share Alike 3.0 Unported License.*

The following basic mechanisms for the photogeneration of radicals in atmospheric and aqueous environments have been proposed when there are water and oxygen present on the TiO_2 surface [10,155,156]. The radicals further attack the organic matter and the decomposition begins.

a) $TiO_2 + h\nu \rightarrow h^+ + e^-$ (generation)

b) $h^+ + H_2O_{adsorbed} \leftrightarrow H^+ + {}^{\cdot}OH$ (reaction)

c) $h^+ + OH^- \leftrightarrow {}^{\cdot}OH$ (reaction)

d) $e^- + O_{2,adsorbed} \leftrightarrow {}^{\cdot}O_2^-$ (reaction)

e) ${}^{\cdot}O_2^- + 2HO^{\cdot} + H^+ \rightarrow H_2O_2 + O_2$ (reaction)

f) $HOOH \rightarrow HO^{\cdot} + {}^{\cdot}OH$ (reaction)

g) $h^+ + Ti^{4+}OH \rightarrow (Ti^{4+}OH^{\cdot})^+$ (hole trapping)

h) $e^- + Ti^{4+}OH \leftrightarrow Ti^{3+}OH$ (electron trapping)

Titanium dioxide's wide band gap and appropriate locations for valence and conduction band make it good material for photocatalytic reactions. Figure 8 shows a schematic of the TiO_2 band edges and the potentials for various redox processes. The redox potential for photogenerated holes is +2.53 V versus the standard hydrogen electrode (SHE) in pH 7 solution. After a hole (h^+) is generated (a) and it has reacted with water (b), it can produce a hydroxyl radical ($^{\bullet}OH$) (b,c). The redox potential for TiO_2 conduction band electrons is –0.52 V, which can reduce oxygen (O_2) to superoxide ($O_2^{\cdot -}$) or to hydrogen peroxide (H_2O_2) (d-f). Ti^{4+}(OH) can form Ti^{3+}OH by the capture of electrons serving as electron traps [157]. The shortcoming is that these groups may further attract holes forming recombination centers [158] and thus preventing potential degradation processes.

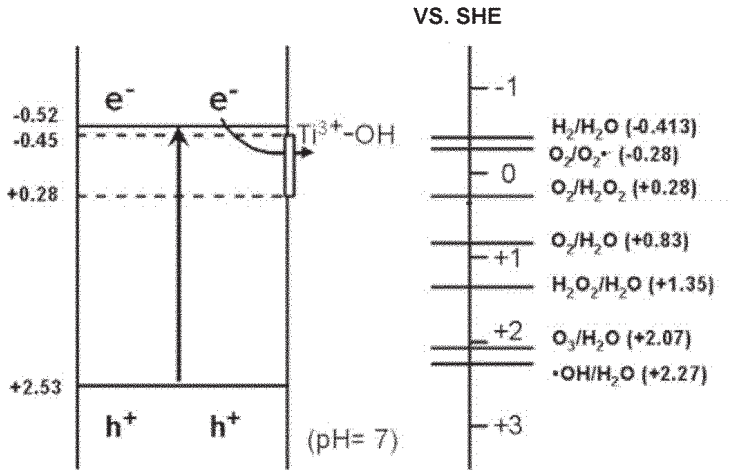

Figure 8. Potentials for various redox processes occurring on the TiO_2 surface at pH= 7. The band edge positions (left) and redox couples move to more negative potentials when the pH is increased. Adapted from [11]. *Copyright © 2006 Académie des Sciences, Elsevier Masson SAS.*

The superhydrophilicity of TiO_2 was discovered in 1995 [13,14]. Sakai *et al.* [159] suggested the mechanism for hydrophilic-hydrophobic changes under UV irradiation (Figure 9).

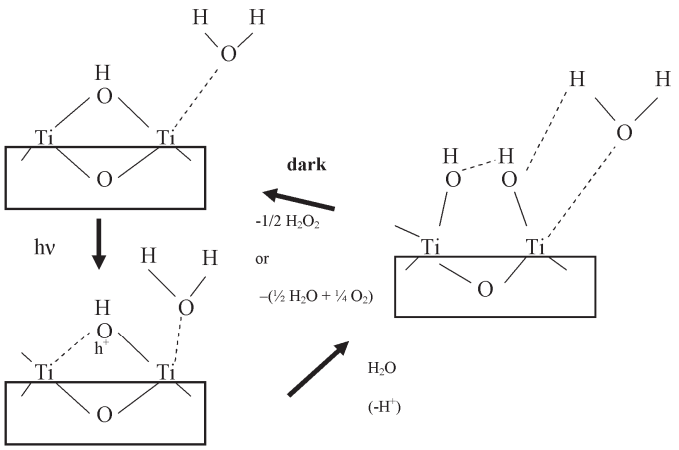

Figure 9. TiO_2 surface during the reversible hydrophilic changes. Adapted from [11]. *Reprinted with permission from (N. Sakai, A. Fujishima, T. Watanabe, K. Hashimoto, Quantitative Evaluation of the Photoinduced Hydrophilic Conversion Properties of TiO_2 Thin Film Surfaces by the Reciprocal of Contact Angle, J. Phys. Chem.B 107 (2003) 1028.) Copyright © 2003, American Chemical Society.*

Figure 9 shows the changes of hydrophilicity on a TiO_2 surface [11,159]. The upper illustration shows the situation in the dark. After UV illumination (below) photoexcited electrons are captured by molecular oxygen. At the same time they diffuse to the TiO_2 surface. Based on investigations the diffusion rates for both excited holes and electrons in bulk rutile and anatase have been recognized to be fast [107,108,160]. After diffusion to the surface the holes will get trapped at lattice oxygen atoms. Consequently, the hole trapping weakens the binding energy between the Ti atom and the lattice oxygen. Another adsorbed water molecule gets a chance to break this bond and new hydroxyl groups are formed (illustration on the right). In the dark the hydroxyl groups gradually desorb from the surface in the form of H_2O_2 or $H_2O + O_2$.

The photocatalytic activity of TiO_2 may be modified by changing its physicochemical properties such as crystallinity, crystal structure, particle size, defect density, film thickness, and surface area [161-164]. Several studies of TiO_2 particles have shown that there is a

synergistic effect on the photocatalytic properties between anatase and rutile and that both phases are needed in order to produce an efficient photocatalyst [165-179]. Bickley *et al.* [165] suggested that electrons transfer from anatase to the lower bandgap rutile crystals which serve as electron trapping sites and thus separate the electrons and holes. In a recent study Komaguchi *et al.* have demonstrated an electron transfer from the anatase phase to the rutile phase [178]. Kawahara *et al.* presented that a photoinduced interfacial electron transfer from anatase to rutile increases TiO_2 photocatalytic activity [169,170]. Liu *et al.* concluded that the photogenerated electrons in the rutile conduction band result in superoxide radicals and the holes in the anatase valence band contribute to oxidation reactions [179]. There are also contradictory studies which claim that the electron transfer occurs from rutile to anatase [168,173,174]. Ohno *et al.* studied commercial Degussa P-25 powder which contains anatase and rutile in a 3:1 ratio [168]. They suggested that the electron transfer takes place from rutile particles to anatase particles [168,171] since rutile contains Ti^{3+} ions which are electron donors. Hurum et al. [174] presented a theory of a catalytic "hot spot" between large anatase crystallites and small rutile crystallites. They explained that the electron transfer occurs from rutile to lower energy anatase trapping sites allowing more stable charge separation and hence higher photocatalytic efficacy.

Film thickness has been also discovered to have an effect on the photocatalytic activity [163,164]. Pore *et al.* accomplished the first study for the photocatalytic properties of ALD grown TiO_2 films [135]. Titanium tetramethoxide $Ti(OMe)_4$ and water were used as precursors. The ALD films were deposited at various temperatures and the film thicknesses were between 60-150 nm. The films grew as polycrystalline anatase above 250°C. The decomposition of methylene blue solution and stearic acid which had been spin coated on the film surface was studied. In both tests all crystalline films were found to be photocatalytically active.

2.4.1 Nitrogen-doping of TiO_2

The most common method to extend the photoresponse of TiO_2 to visible light area is doping with transitional metal-ions and/or non-metals [180-183]. In multiple studies doping has resulted in TiO_2 absorption edges red-shifting to wavelengths of 550 nm and higher. Doping may also result in inferior photocatalytic properties caused by increased recombination

centers or thermal instability [180]. The reasons for the doping effects are still unclear. Based on the DFT studies the band gap of TiO_2 decreases due to interactions between the dopant states and O 2p states of the valence band which cause the valence band edge to rise upward [180]. Other reports have proposed isolated dopant states located within the band gap through which the excitation of electrons takes place to the conduction band resulting in a red shift [184]. Asahi *et al.* produced substitutionally doped $TiO_{2-x}N_x$ films by sputtering and created photocatalytically active TiO_2 in the visible light region [185]. Since Asahi's work nitrogen doping has been considered to be the most effective approach to improve photocatalytic reactivity under visible light illumination.

Nitrogen can be incorporated in titanium dioxide by various methods. These can be oxidation of titanium nitride, chemical reaction processes (sol-gel, CVD, ALD), or with physical techniques (magnetron sputtering, ion implantation) [180,183]. The mechanism of nitrogen doping has been investigated by Di Valentin *et al.* [184,186]. They performed DFT-calculations considering two different doping models of substitutional and interstitial N-doping. Their results showed that in substitutional doping the nitrogen atom is bound to three Ti atoms and replaces lattice oxygen in TiO_2. This nitrogen atom is in a negative oxidation state (N^{2-}). In interstitial doping the nitrogen atom is bound to one lattice oxygen and therefore is in a positive oxidation state. The resulting NO species interacts with the lattice Ti atoms through its p-bonding states [184]. In preparing N-doped TiO_2 the experimental parameters will determine which doping type will dominate the structure. Interstitial doping will be preferred when there is an excess of nitrogen and oxygen in the process. In high-temperature oxygen-poor calcination processes N-doping will result in substitutional doping and oxygen vacancies. Figure 10 presents substitutional N-doping and interstitial N-doping structure in the TiO_2 anatase phase.

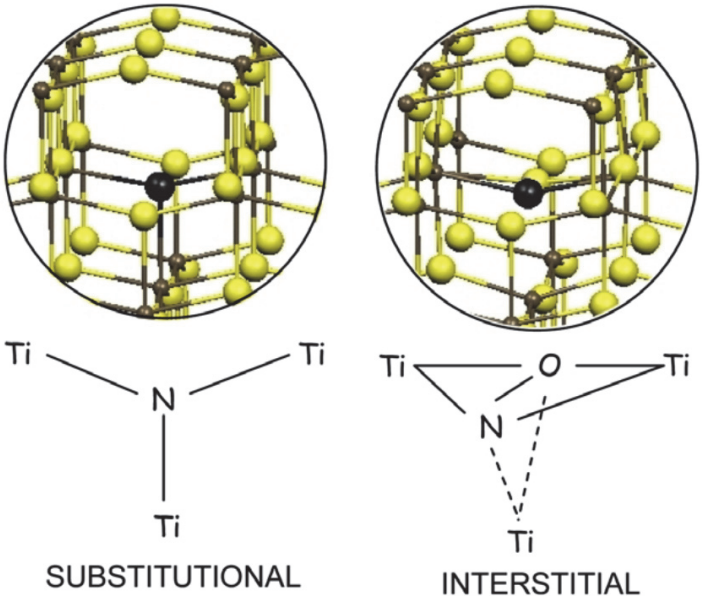

Figure 10. Model structures for substitutional and interstitial N-dopants in anatase TiO_2 phase [184]. *Reprinted with permission from (C. Di Valentin, G. Pacchioni, A. Selloni, S. Livraghi, E. Giamello, J. Phys. Chem. B, 109 (2005) 11414.). Copyright (2005) American Chemical Society.*

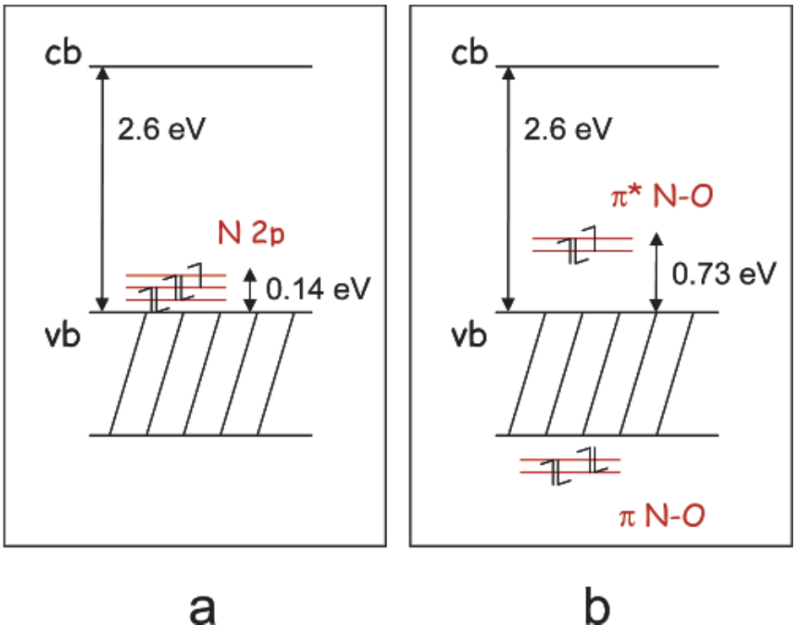

Figure 11. Electronic band structure for (a) substitutional and (b) interstitial N-doped anatase TiO_2, as given by PBE calculations at a low-symmetry *k*-point. The calculated value of the band gap 2.6 eV is lower than experimental values due to the well-known limitating effect from DFT-calculation [184]. *Reprinted with permission from (C. Di Valentin, G. Pacchioni, A. Selloni, S. Livraghi, E. Giamello, J. Phys. Chem. B, 109 (2005) 11414.). Copyright (2005) American Chemical Society.*

Figure 11 presents computed electronic band structures for both substitutional and interstitial N-doping systems [184]. In both systems the formation of localized states in the band gap are found. Substitutional nitrogen states (a) are situated above the valence band whereas interstitial nitrogen states (b) are placed higher in the gap. Excitation from these localized states to the conduction band may result in a narrower band gap and in a red shift towards the visible light region.

In addition Di Valentin *et al.* calculated a relative difference in core level shifts for N-doped TiO_2 samples and compared them with the experimental values based on X-ray photoelectron spectroscopy (XPS) measurements [184]. The investigators reported that the calculated core level shift between substitutional and interstitial doping was 1.6 eV which correlated well with the experimental values for 397 eV (attributed for substitutional N) and >399 eV (interstitial N).

2.4.2. Nitrogen doping in ALD-grown TiO_2 thin films

The first N-doping trial for TiO_2 with ALD method was accomplished by Pore *et al.* [187]. They combined ALD deposition of TiN and TiO_2 ALD-processes in order to achieve $TiO_{2-x}N_x$ films. TiN films can be grown from $TiCl_4$ and NH_3 precursors and TiO_2 films by using water as an oxidant. Different doping concentrations between 0.7-8.1 at-% were achieved by varying the relative amount of TiN and TiO_2 layers. All films were deposited at 500°C onto borosilicate glass substrates and the film thicknesses varied between 120-225 nm. Interestingly despite the high deposition temperature all the films were anatase or anatase dominating. The investigators noticed that the anatase phase was favored due to the conversion from TiN into TiO_{2x}-N_x. The results showed that $TiO_{2-x}N_x$ film with the highest nitrogen concentration produced the lowest band gap of 2.9eV. The photocatalytic reactivity in stearic acid degradation tests under UV light illumination showed that the doped samples performed more poorly than undoped films. Under visible light illumination both doped and undoped TiO_2 films were photocatalytic. The low photocatalytic reactivity was considered to be due to increased recombination of electrons and holes. In addition the investigators concluded that the doping decreased the superhydrophilicity of TiO_2 films. Another N-doping trial with ALD is discussed later in Chapter 4 (**I**, **IV**).

2.5 Structure of ZnO

ZnO can be found in three crystalline forms: hexagonal wurtzite, cubic zincblende, and rocksalt. Wurtzite is the most stable in ambient conditions and hence is more common than zincblende. Zincblende can be formed only in specific growth conditions. Rocksalt can only be formed in relatively high temperatures and pressures [188,189]. The unit cell parameters of wurtzitic ZnO are a=b= 0.325 nm and c= 0.521 nm. In the ZnO wurtzite structure tetrahedrally coordinated Zn and O atoms form planes which are alternately stacked along the c-axis. Figure 12 presents the ZnO wurtzite structure.

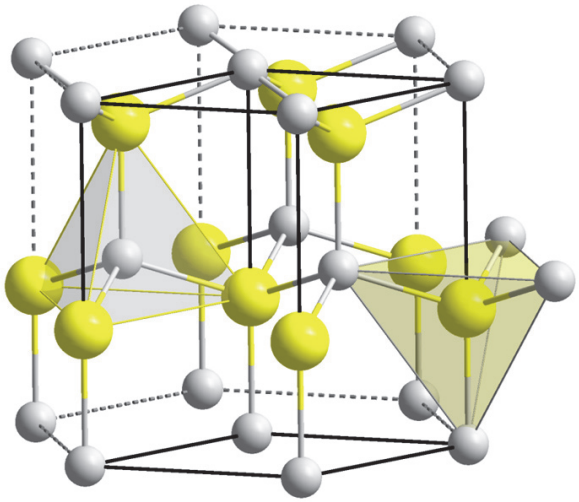

Figure 12. Structure of ZnO wurtzite crystal [190]. *Public Domain*

Wutzite ZnO has no inversion symmetry (a reflection from at any point in the crystal does not transform into itself). This property is related to the piezoelectric and pyroelectric characteristics of ZnO [191]. The lattice constant ratio c/a ~ 1.60 is close to the ideal value for hexagonal cell *c/a* = 1.633 [192]. The bonding between zinc atoms and oxygen atoms is ionic ($Zn^{2+} - O^{2-}$). The radius for Zn^{2+} is 0.074 nm and for O_2^- 0.140 nm. ZnO bonds are polar and therefore the planes of ZnO are electrically charged [191]. The most common polar surface on ZnO is (0001) plane. In one direction, the (0001) plane terminates with partially positive Zn lattice sites and in the other direction it terminates in partially negative oxygen lattice sites. This creates a positively charged Zn (0001) surface and a negatively charged O $(000\bar{1})$ surface in the [001] direction. Normally crystal planes tend to reconstruct in order to reach electrical neutrality but this has not been found to occur on ZnO surfaces. This anomaly is still under scrutiny [193-195]. The other common ZnO surfaces are $(2\bar{1}\bar{1}0)$ and $(01\bar{1}0)$ which are non-polar and possess lower energies than (0001). The polar hexagonal ZnO crystal is presented in Figure 13.

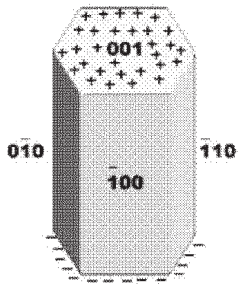

Figure 13. The structure of hexagonal polar ZnO crystal [196]. *Reprinted with permission from Springer © 2006.*

2.6 Properties of ZnO

The native doping form of ZnO is n-type. It has been suspected to arise from oxygen vacancies or interstitial Zn atoms but this knowledge has not been confirmed. Zinc oxide has been generally found to be an n-type semiconductor with a bandgap of about 3.37 eV being near the UVA area. The high exciton binding energy (60 meV) in ZnO crystals allows efficient excitonic emission at room temperature. The most common defects in the ZnO structure are oxygen vacancies (Ov), zinc interstitials (Zn_i), oxygen interstitials (O_i), zinc antisites (Zn_O), negative U-centers, extrinsic impurities and hydrogen related defects [197,198]. The causes for these defects are still divisive [199] but they have an evident effect on the properties of ZnO.

ZnO is an eminent material for its bactericidal properties. Recently ZnO nanoparticles have been studied widely in antibacterial testing. ZnO has shown a strong bactericidal effect against various bacteria [200-203]. The antibacterial mechanism of ZnO is still unclear and being currently scrutinized. Sawai *et al.* suggested that the photocatalytic generation of hydrogen peroxide was a principal mechanism for the antibacterial effect [200]. It has also been proposed that ZnO nanoparticles will penetrate the cell envelope and disorganize the bacterial membrane [203, 204]. The dissolution of Zn^{2+} ions has been successful but the mechanism is not clear [205,206]. ZnO has been dissolved under aqueous conditions to form

hydrated Zn^{2+} ions. Other studies have shown that the dissolution of Zn^{2+} was enhanced under acidic conditions and with the presence of biological components such as amino acids and peptides [207]. The effect of the ZnO particle size has been studied and the results have been contradictory [202,205]. All types of morphology in polycrystalline ZnO particles have performed well in antibacterial studies against *E.coli* and *S.aureus* [208].

2.7 ALD grown ZnO thin films

Zinc oxide (ZnO) thin films are an extensively studied area and there are several methods such as reactive magnetron sputtering, electron beam evaporation and chemical vapor deposition that have been used in their production. During recent years atomic layer deposition (ALD) has gained an immense interest for producing metal oxides and a large amount of studies have been conducted on ZnO.

Due to their high reactivity, diethyl zinc (DEZ) and water have been the most commonly used ZnO precursors in ALD.

The binary CVD reaction for ZnO deposition is

$$Zn(CH_2CH_3)_2\ (g) + H_2O\ (g) \rightarrow ZnO\ 8s) + 2C_2H_6\ (g) \quad (3)$$

this can be written in two ALD half-reactions [209]

$$OH^* + Zn(CH_2CH_3)_2 \rightarrow OZn(CH_2CH_3)^* + C_2H_6 \quad (4)$$

$$OZn(CH_2CH_3)^* + H_2O \rightarrow OZnOH^* + C_2H_6 \quad (5)$$

Diethyl zinc, DEZ is susceptible to thermal decomposition at higher temperatures [210,211]. The dissociation takes place between the Zn-C bond. The applied reaction temperatures are usually between 100 - 250°C.

Lim and Lee [212] studied the ZnO process over a temperature range of 100 – 250°C, depositing films on sapphire (0001) substrates. Pulse lengths for DEZ and H_2O were 0.2 s and 0.15 s, respectively. Purging time with nitrogen (N_2) was 2 s after each pulse. An ALD window was found for reaction temperatures between 130 – 180°C where the growth rate was about 0.26 nm/cycle. The crystalline orientation for the films was (002), which is also the thermodynamically favorable orientation for ZnO. The crystallinity was found to improve with increasing temperature. In another study the DEZ and ozone (O_3) process was compared with the DEZ – H_2O process [211]. The films were deposited on SiO_2/Si substrates over a temperature range of 230 – 300°C. At 250 °C the saturation limit was reached with 1 s DEZ pulsing time and the growth rate was 0.17 nm/cycle, which was lower than frequently reached value of 0.2 nm/cycle with the DEZ-H_2O process. In both precursor processes the preferred crystal orientation was (002). It is noticeable that the mobility, carrier concentration, and conductivity of ZnO were all lower when using the ozone process. The investigators expected this was due to Si diffusion from the substrate during the ozone process. Alternatively it is possible that the number of oxygen vacancies created is lower in the ozone process especially at higher temperatures.

Lim *et al.* compared ALD grown ZnO with sputtered ZnO [213]. DEZ and water were used at reaction temperatures between 100 – 250 °C using Ar as both purging and carrier gas. Corning 1737 glass and Si (001) were used as substrates. The growth rate increased with increasing temperature and decreased again at 175°C and higher temperatures. The films were polycrystalline at all temperatures with a dominant orientation of (002). The resistivity of the ZnO film was high and mobility low at low reaction temperatures and clearly higher when the temperature was increased. In contrast sputtered ZnO films had a much higher resistivity, and low mobility, compared to ALD grown films.

King *et al.* [209] showed that ZnO overlayers can be efficiently deposited on the surfaces of primary particles using ALD processing in a scalable fluidized bed reactor. The DEZ and water process was used at 177°C and the growth rate was found to be 0.2 nm/cycle. The substrate particles were SiO_2 spheres to be applied in UV blocking cosmetics.

Fong *et al* [214] used *in situ* synchrotron X-ray scattering and X-ray fluorescence (XRF) to study the initial nucleation stage and the growth during the first 16 cycles. The deposition was performed at 125°C onto Si(100) substrate and DEZ and water were used as precursors.

During the first 16 cycles ZnO remained amorphous and the growth was found to be substrate-inhibited [215] forming islands instead of a conformal film. The growth rate was 0.42 nm/c between 6-10 cycles and decreased to 0.3 nm/c after 10 cycles of growth.

ALD grown ZnO films were deposited over the temperature range of 100-300°C onto glass, silicon, and commercial GaN/Al_2O_3 substrates for electrical applications. The obtained films were polycrystalline with high mobility and low free electron concentration. [216-218]

In order to create conductive films onto cotton paper and fiber mat, ZnO was deposited at 115°C using diethylzinc (DEZ) and water as precursors [219]. ZnO on both cotton and paper showed effective conductivity of up to 24 Scm^{-1}. The results showed that ALD can be regarded as a feasible tool to attain well-controlled conductive and semiconductive coatings on various fiber materials.

3. Experimental methods

3.1 Film deposition

TiO_2 and ZnO films of thickness between 2.6 nm and 280 nm were grown by atomic layer deposition (ALD). The deposition was carried out in a TFS-500 ALD reactor (Beneq Oy) at 5 –10 mbar (5×10^2–1×10^3 Pa) pressure (**I-V**). The titanium dioxide/metaloxide (TiO_2/MeOx) nanolaminates (**I**) were deposited with F-120 ALD reactor (ASM Microchemistry Oy).

Bottled nitrogen (Oy AGA Ab) or generated nitrogen of 99.999% purity was used as a carrier and purging gas (INMATEC IMT-PN 1150, INMATEC GaseTechnologie GmbH & Co.KG). In the TiO_2 process titanium tetrachloride (99.0%, Fluka) and deionized water were used as precursors. The precursors were kept at 20°C during the deposition and their partial pressure was adjusted with needle valves. In addition, Si (100) wafers were used in all depositions in order to estimate the growth and the thickness of the films.

The precursors used for the TiO_2 process (**I-IV**) were titanium tetrachloride ($TiCl_4$) and deionized water. The reaction temperatures were 250°C and 350°C. The precursors were introduced into the reactor in a sequence of pulse ($TiCl_4$) – rinse (N_2) – pulse (H_2O) – rinse (N_2) of 0.6– 1–0.25–0.5 s. Soda-lime glass plates of 5 cm×5 cm were used as substrate materials. The grown thicknesses were between 2.6 nm – 260 nm. The nanolaminates were created by depositing the precursors in sequences. TiO_2/WO_3 was created in two different sequences: 9 x (200 x TiO_2 + 20 x WO_3) and 17 x (100 x TiO_2 + 10 x WO_3). All the other nanolaminates were deposited with 17 x (100 x TiO_2 + 10 x MeO_3) sequence. The growth rate for TiO_2/WO_3 was approximately 0.028 nm/cycle. The growth rate for TiO_2/In_2O_3, TiO_2/Fe_2O_3, and TiO_2/Ga_2O_3 was estimated to be 0.051 nm/cycle. The nitrogen doped titanium dioxide films were created by using titanium tetrachloride as a titanium source and ammonium hydroxide solution as an oxygen and nitrogen source (**IV**).

ZnO films (**V**) were grown by using diethylzinc ($Zn(C_2H_5)_2$) (DEZ) and deionized water as precursors at reaction temperatures of 120 °C and 200 °C. The sequence of the deposition were pulse (ZnO) – rinse (N_2) – pulse (H_2O) – rinse (N_2) of 0.7– 1.5–0.5–1.0 s. Borosilicate

glass plates of 5 cm x 5 cm were used as substrate materials. The thicknesses of the films were between 45 nm and 280 nm. Additional series of ZnO films at both temperatures were also created where aluminum oxide (Al_2O_3) films of 5, 10, and 15nm were deposited on top of the ZnO films. Trimethylaluminum and deionized water were used at 220° C during Al_2O_3 deposition.

3.2 Film characterization

The ALD deposited films were characterized by various methods. The film thickness was measured by two different methods. The crystalline structure of the films was studied by X-ray diffraction (XRD). The morphology was examined by scanning electron microscopy (SEM) and atomic force microscopy (AFM). Electrical resistivities were calculated from the sheet resistances measured with a four-point-probe system. The hot probe tests were performed for majority carrier polarity.

3.2.1 Film thickness

The film thicknesses were measured with a spectroscopic ellipsometer (M-2000FI, J.A.Woollam Co., Inc. and with an optical thin-film measurement system F-20 (Filmetrics, Inc.). Films that were deposited on Si(100) wafers were measured with the spectroscopic ellipsometer since films deposited on reflective surfaces are more reliably measurable by the ellipsometer. Films deposited on glass substrates were measured with an optical thin-film measurement system, from which the refractive index of the film was estimated.

3.2.2 X-ray diffraction (XRD)

In XRD the X-rays are diffracted from the sample crystals to many specific directions. The angles and intensities are detected and XRD pattern is formed which gives information about the crystalline phases and orientations of the film material. The films were characterized by X-ray diffractometer (XRD) (Phillips X'Pert) using CuKα radiation (λ=1.54 Å). The patterns

were acquired with a glancing angle of 0.2° for the incident beam for a 2θ range of 20–60° with a step size of 0.02°. Based on the XRD patterns, grain sizes were calculated using Scherrer's equation [220]. The Scherrer's equation relates the size of the particles of crystallites and diffraction peak broadening. In addition to the crystallite size effect a variety of reasons can contribute to the width of diffraction peak. The most usual factors are inhomogeneous strain and lattice imperfections which both have been neglected in the calculations. The correlation between the grain size calculated from the X-ray peak widths and the SEM measurements suggested that these strain effects were not significant and a clear difference was observed between different crystallite types. Together these justify neglecting strain and lattice effects.

3.2.3 Scanning electron microscopy (SEM)

The morphology of the films was studied with a Hitachi S4800 field emission scanning electron microscope with an operating voltage of 5 kV. In the SEM the sample surface is scanned in a raster pattern with a beam of energetic electrons. The electrons interact with the sample electrons producing various signals that can be detected and converted into image of surface topography. The resolution of the S4800 SEM is given as 1.6 nm.

3.2.4 Atomic force microscopy (AFM)

A tapping-mode AFM was used to determine morphology, surface roughness, and surface area of the films. AFM apparatus of CP-II Scanning Probe Microscope, Veeco Instruments was used in the studies. The AFM consists of a cantilever with a sharp tip that oscillates slightly above its resonant frequency. Above the sample surface, within a range of 1-10 nm, there are van der Waals forces which affect the resonance frequency. The changes in the frequency are then converted into images of the surface topography.

3.2.5 X-ray photoelectron spectroscopy (XPS)

The elemental composition and the chemical and electronic states of the elements within the film were measured with XPS. Aluminum or magnesium X-ray photons are used to irradiate the material from the surface to the depth of about 10 nm. X-rays of sufficient energy will eject electrons from the atoms and the kinetic energy and number of electrons will be analyzed by an electron spectrometer. In the measurements an XPS –system of PHI 5400 was used. A MgKα radiation (energy of 1253.6 eV) was applied at a pressure of $1 \cdot 10^{-9}$ Torr ($1.33 \cdot 10^{-7}$ Pa). Sputtering was performed using Ar^{+} ions with beam energy of 3 keV and a current of 2 μA. The beam was rastered over 3×3 mm^2 hence the mean beam current density was 0.22 $\mu A/mm^2$. Binding energy was referenced in all samples to carbon 1s line assuming energy of 284.8 eV. The resulting XPS peaks were fitted by using XPSPEAK4.1 software applying a Shirley type background and Gaussian peaks.

3.2.6 UV-Vis spectroscopy

A light wave can be absorbed, reflected or transmitted by the sample material. The absorption of UV or visible radiation is caused by the excitation of outer electrons of the sample material which are ejected from their ground state to an excited state. Absorption spectra were measured for methylene blue solution in order to determine degradation state of the molecules. Transmission spectra of the films were measured in order to estimate band gaps. A UV–VIS spectrophotometer Evolution 500 (Thermo Electron Corporation) was used in these measurements.

3.2.7 Band gap evaluation

The transmittances of the films were measured for a wavelength range of 200-900 nm and the band gaps were evaluated by Tauc's method [221,222]. The Tauc plot for a direct band gap was chosen first since rutile is found to have a direct band gap. However, the results showed unrealistically high band gaps. In addition amorphous and anatase films are found to possess

indirect band gaps. Consequently the indirect plot was chosen where the term $(\alpha h\nu)^{1/2}$ is plotted as a function of ($h\nu$), where α = absorption coefficient, h= Planck's constant, and frequency $\nu = c/\lambda$ where c = speed of light, and λ = wavelength. The optical band gap is estimated from the intersection of the linear extrapolated line with the horizontal axis ($h\nu$).

3.2.8 Electrical measurements

Resistivities of the films were calculated from the sheet resistances which were measured by a four-point-probe. The measured sheet resistance was multiplied with the film thickness in order to get the film resistivity. The measurements were performed with a Keithley Source meter and Cascade Microtech 4-point probe station. The polarity of the majority carriers within the films was determined using the hot probe measurement. The measurement is prepared by connecting a couple of wires to a sensitive electrometer. A heated probe, called a hot probe is connected to the positive terminal and the other, called a cold probe is connected to the negative terminal of the meter. When the probes are placed on an n-type semiconductor a positive potential is measured on the hot probe while when placed on a p-type semiconductor a negative potential is measured [223]. The polarity was measured after taking the samples from dark storage and again after 30 min of UV irradiation.

3.3 Photoactivity and Photocatalytic measurements

3.3.1 Contact angle measurement

The changes in the hydrophilicity were measured with water contact angles. TiO_2 films were irradiated under an 8W UV lamp with a wavelength of 254 nm. The films were kept 10 cm from the lamp. The water contact angles were measured immediately, and after 15 and 30 min of irradiation. The contact angles were measured with a contact angle measuring system DSA 10 (Krüss GmbH).

3.3.2 Methylene blue degradation test

Photocatalytic degradation measurements were conducted with methylene blue (MB) tests which were carried out as follows. Titanium dioxide films on a glass plate (5 cm×5 cm) were first photoactivated in air by UV irradiation for 45 min. An 8 W UV lamp with a wavelength of 254 nm was used as a UV radiation source. The distance of the sample from the lamp was 10 cm. After preactivation, titanium dioxide films were placed in a 1 L beaker with 100 mL of an aqueous solution of methylene blue with concentration of 1×10^{-5} mol/L, 2–3 mm from the liquid surface. The test system was kept under the UV lamp for 4 h in ambient temperature. The UV lamp was placed above the beaker and the distance from the lamp to the titanium dioxide films was 15 cm. The power flux of the UV lamp at distances of 10 – 20 cm was estimated to be 3.8 mW/cm^2. The absorption spectra of the MB solution samples were measured with the UV–VIS spectrophotometer. In order to eliminate the effect of possible methylene blue adsorbance the TiO_2 films were kept in the solution in darkness without photoactivation. The UV-Vis absorbance of the solution was measured before and after the test.

3.4 Antibacterial studies

3.4.1. Bacterial attachment

A fresh shake culture of *E.coli* was prepared in sterile LB medium by shaking at 37 °C and 200 rpm for 18 h. An exponential growing culture was obtained by dilution with sterile LB medium to an absorbance of 0.1 at 600 nm and shaking to an absorbance of 0.5 at 600 nm which correspond to a concentration of to 1.5 x 10^6 CFU mL^{-1}. Samples (2.5 cm x 2.5 cm, 6.25 cm^2) and silicon wafer control were placed in a 6-well culture plate (Greiner, Germany) and submerged with 2 mL bacteria dilution, covered with a lid, sealed with parafilm and incubated on a horizontal shaker (Innova 44, New Brunswick Scientific) at 37 °C for 24 h. Then the samples were placed in a fresh 6 well culture plate and washed 4 times with saline. Bacteria attaching to the films were stained with Live/Dead BacLight Bacterial Viability Kit

(Life Technologies, Germany) according to the supplier's protocol. The bacteria were imaged on an inverted microscope (Olympus IX-70) equipped with a 100 W mercury lamp, a 20x phase contrast objective and a CCD camera (F-View, Olympus) for digital imaging. Living bacteria stained with SYTO 9 (green) were excited with a band pass filter at 470 nm to 490 nm and the emission was detected by 520 nm. Dead bacteria cells stained with propidium iodide were excited with a band pass filter at 530 – 550 nm and the emission was detected by 590 nm. Image processing performed with CellSens Dimensions 1.5 (Olympus) and ImageJ (Fiji).

3.4.2. Antibacterial activity

ZnO films were used to determine their antibacterial activity in the darkness without photocatalytic effect. A fresh shake culture of *Escherichia coli* (*E.coli* K-12 wildtype, K-12 DSM 498, ATCC 23716) was prepared as described above and the bacteria were diluted with minimal LB to correspond to a concentration of 1.0 x 10^8 CFU mL^{-1}. The bacteria solutions were adjusted with KH_2PO_4 buffer (0.3 mM, pH 7.2, sterile) to ~2.5 x 10^5 CFU mL^{-1}. ZnO films (triplicate, 2.5 x 2.5 cm) were submerged in 7 mL bacteria dilution. Uncoated borosilicate glass (2.5 x 2.5 cm) served as control samples. All samples were incubated on a horizontal shaker (Innova 44, New Brunswick Scientific) at 37 °C and 150 rpm for 1 h. The bacteria concentration were determined at T_0 and T_{1h} by serial dilutions in saline (undiluted, 1:25, 1:125), plating of an 50 µL aliquot on agar plates and incubation for 24 h at 37 °C to give an estimate of viable cell count as CFU mL^{-1}. The mean value and standard deviation was calculated from the serial dilutions of each sample. The percent of bacterial reduction was calculated from treated sample (A) directly compared to untreated control (B) at T_{1h} where reduction is defined by R, % (CFU mL^{-1}) = ($B_{CFU\ mL^{-1}} - A_{CFU\ mL^{-1}}$)/$B_{CFU\ mL^{-1}}$ x 100.

4. Results and Discussion

The purpose of this work was to study the growth and crystalline structure of ALD deposited TiO_2 and ZnO thin films and understand their effect on the characteristics of the materials. The most important results are presented here and in detail in papers **I-V**. Undoped and doped

TiO_2 films have been studied and compared in paper **I**. The effect of film thickness and grain size on the growth and crystalline structure of ALD grown TiO_2 thin films is presented in paper **II**. In addition the crystalline structure and synergy between different phases have been found to produce enhanced photoactivity and photocatalytic properties [**II]**. Majority carrier polarity has been found to contribute to the performance in photoactivity and photocatalytic property [**III]** and p-n junctions in TiO_2 have been proposed to account for high photocatalytic property. Successful nitrogen doping TiO_2 films has resulted in improved photocatalytic performance [**IV]**. Dissolution of $Zinc^{2+}$ ion has been shown to take place from ALD grown ZnO films [**V]**. ALD grown ZnO films without photoactivation have shown immense performance in antibacterial studies. The result confirms that ZnO does not need photon energy for its bactericidal function [**V]**.

4.1 The effect of film thickness and structure on TiO_2 photoactivity and photocatalytic properties

A series of TiO_2 films with thicknesses of 2.6 nm-260 nm were deposited using the $TiCl_4$ and H_2O ALD-process [**I,II]**. According to the AFM images even the films with thickness of 2.6 nm was showing particle like growth. Nevertheless the first film where a crystal phase appears clearly in an XRD pattern is the 15 nm thick film. The XRD indicates only anatase (101) orientation but the AFM images show film growth with various shapes of grains. Rutile grains appear as facetted whereas the anatase grains are spherical (Fig. 14) [224-226].

The thermodynamical and experimental studies with nanoparticles concluded that the most stable particle size was ≤ 14 nm [150] and beyond that value anatase would transform into rutile. In this study the grain size of anatase in the 15 nm film where the first rutile phase had appeared was evaluated to be 13.3 nm which corresponds with the nanoparticle studies.

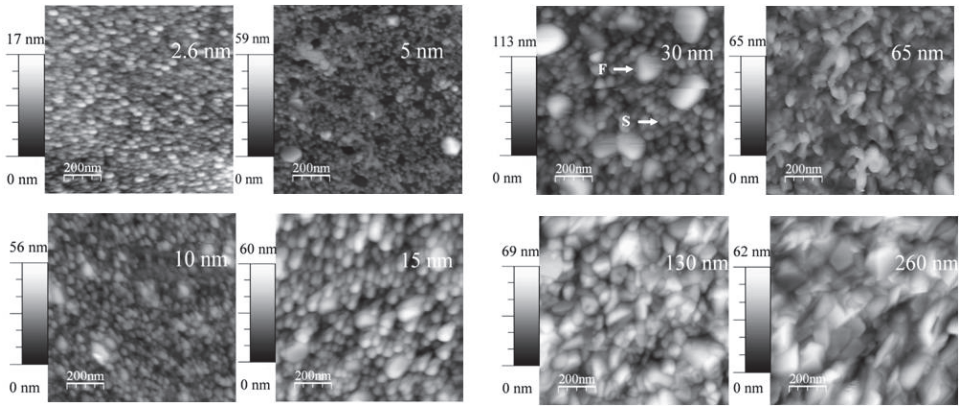

Figure 14. AFM tapping mode images of titanium dioxide films of various thicknesses. F and S indicate typical facetted and spherical grains, respectively [Fig3,**I**]. *Reprinted with permission from Elsevier ©2009.*

In the contact angle studies the 2.6 nm film showed poor photoactivity. This may be due to likelihood that the film did not cover the whole substrate surface, although the film appears continuous in the AFM image.

The thickest rutile dominating film possessed also weaker photoactivity than anatase or anatase-rutile –mixture films (Fig. 4, **II**). The difference between anatase and rutile may be due to different recombination rates. Anatase is an indirect band gap semiconductor and rutile has been found to possess a direct band gap [104]. The direct band gap has been proposed to cause the higher recombination rate preventing the formation of hydroxyl groups which would make the TiO_2 surface hydrophilic. Nevertheless in Chapter 4.3 (Table 2, **IV**) Tauc's method for the indirect band gap was used also for rutile since the direct method was found to present too high band gap values. This may be an indication that also rutile has an indirect band gap. Rutile has been found to be more prone to oxygen vacancies which attract water molecules and can dissociate them into pairs of nearby bridging hydroxyl groups [95]. It is possible that rutile in these ALD grown TiO_2 films is more defect free and the oxygen vacancy density is low. In addition there have also been controversial studies where DFT-calculations have shown that water does not dissociate on rutile at all [99]. Nonetheless the results show that photoactivity decreases with increasing amount of rutile phase within the film. The best photoactivity was found for the 15 nm film which consisted of anatase (101)

with a small amount of rutile (110) phase present. The best photocatalytic performance was also found with the 15 nm thick film. There have been several investigations which have shown that good photocatalytic activity is reached where there is anatase and rutile synergy. It has been claimed that the existence of anatase and rutile phases leads to a separation of photogenerated holes and electrons which reduces their recombination rate. The surface areas and grain sizes in all the films were similar and therefore had no effect on the photocatalytic activity (Tables 1,2, **II**). Additionally film thickness was only significant due to the changes in the crystalline structure of the TiO_2 films. The most important factor for high photoactivity and photocatalytic performance was the anatase/rutile phase ratio. In paper **I** TiO_2 films were doped with transition metals by creating TiO_2/MeO_3 nanolaminates and with nitrogen by using NH_4OH –solution as nitrogen and oxygen source. The results showed that all the nanolaminates films showed inferior photoactivity and photocatalytic activity than undoped TiO_2 films (**I**). The nitrogen doped films performed well in photoactivity tests and showed improved photocatalytic performance compared to undoped films.

4.2. The effect of majority carrier polarity on photoactivity and photocatalytic activity of TiO_2 films

Majority carrier polarity was studied on several TiO_2 films with different crystalline phases and orientations (**III**). Two series of TiO_2 films with various thicknesses were deposited at 250°C and 350°C reaction temperatures with the ALD $TiCl_4$-H_2O –process. The polarity was examined with a hot probe test [223]. The hot probe test was performed right after the TiO_2 films were taken from dark storage and after 30 min of UV irradiation. It was discovered that all the anatase or anatase dominating films were p-type before and after the irradiation [Table 1, **III**). The definition for a p-type semiconductor is that the charge carriers are holes and there are excess of holes in the TiO_2 structure. Since oxygen vacancies have been found to cause n-type doping in materials, it can be deducted that these ALD-grown anatase films are free of oxygen vacancies. This result coincides with the earlier findings that the formation of oxygen vacancies on anatase is difficult and therefore molecular water is found to adsorb on anatase surface [91,98]. Based on the hot probe tests rutile and rutile dominating films were n-type. In n-type material the charge carriers are electrons and there is an excess of electrons within the structure. The n-type doping is often caused by oxygen vacancies. Rutile is prone

to have oxygen vacancies since its surface structure contains two-fold coordinated (undersaturated) 'bridging' oxygens which are easily removed by thermal annealing [74].

The contact angle tests (Fig.2, **III**) showed clearly that p-type anatase outperformed n-type rutile in photoactivity. The rutile films that did not contain anatase phase maintained the highest contact angles even during UV-irradiation. The results showed a different trend when the photocatalytic activity was measured. All the TiO_2 films containing only anatase phase were inferior in photocatalytic tests. Also a film with rutile dominance acted more poorly than the anatase dominating films. The films which were anatase dominating with some growth of rutile phase seemed to possess the highest photocatalytic activity. It was proposed that p- type anatase and n-type rutile form p-n junctions in the TiO_2 which can cause carrier separations and therefore decrease the recombination rate (**III**). The proposed p-n junction is presented in Figure 15. A similar heterojunction has been proposed by Zhang *et al.* with p-type NiO/n-type ZnO [227].

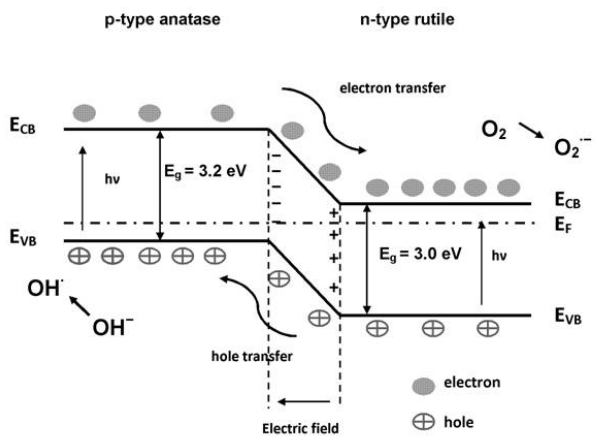

Figure 15. The electron-hole separation due to p-n junction during UV-irradiation of TiO_2 containing dominating anatase phase with small amount of rutile.

A p-n junction is formed when electron transfer takes place from n-type rutile to p-type anatase and hole transfer takes place from p-type anatase to n-type rutile. The carrier diffusion

continues until the system achieves equilibrium. At the same time an electric field is formed in the interface due to the carrier transfers. During UV-irradiation with sufficient photon energy to excite the electrons on both anatase and rutile, the electrons from the valence band (VB) will move to the conduction band (CB) and an equal amount of holes is generated. After excitation the electrons will transfer from the anatase conduction band to a lower energy rutile conduction band and in contrast the holes will transfer from the rutile valence band to the anatase valence band (Fig. 15). This results in the separation of electron-hole –pairs and in reduced recombination. The life span of charge carriers may therefore increase resulting in enhanced interactions with adsorbed species (H_2O, O_2).

4.3 Nitrogen doping of ALD grown TiO_2 films

TiO_2 films were grown using a $TiCl_4$ and ammonium hydroxide –water –solution (NH_4OH). NH_4OH was used as an oxidant and simultaneously as a nitrogen source for doping (**IV**). The results from XPS spectra showed that N1s peaks were found for doped samples at 398.9-399.1 eV which indicated interstitial N-doping (Fig.3A,**IV**). Interstitial doping has been found to occur when there is an excess of nitrogen and oxygen in the process [184]. In addition N-doping effect was possibly seen as a change in the band gap of 260 nm films. The undoped film had a band gap of 3.2 eV whereas the value for doped films was 3.1 eV.

Based on the hot probe measurements all N-doped and undoped anatase dominating films were p-type. All N-doped and undoped rutile dominating films were n-type. Consequently the N-doping had not influenced the majority carrier polarity (Table 3,**IV**).

The photoactivity was affected by the N-doping. The doping seemed to be deleterious especially for rutile films where the photoactivity decreased in all rutile dominating films when undoped and doped samples were compared (Fig.4,**IV**). Interstitial N-doping has been suspected of preventing the formation of oxygen vacancies which would otherwise dissociate water molecules into hydroxyl groups. In fact the XPS results indicated that the doped samples had less chemisorbed water on their surface and that the doping had affected the hydrophilicity of the rutile dominating films (Fig.3C,**IV**). The 15 nm thick doped A-sample showed superhydrophilicity and also anatase films in the B-series showed good photoactivity.

The best photocatalytic activity in all doped and undoped series was achieved with anatase dominated films with a small amount of rutile (Fig.5,**IV**). The photocatalytic activity increased to 260% when comparing the doped A-series and undoped series (Fig.16). Since the N-doping was found to increase the conductivity of the doped series (Fig.6,**IV**), it was concluded that the higher conductivity together with the existence of p–n junctions enabled the higher photocatalytic conductivity.

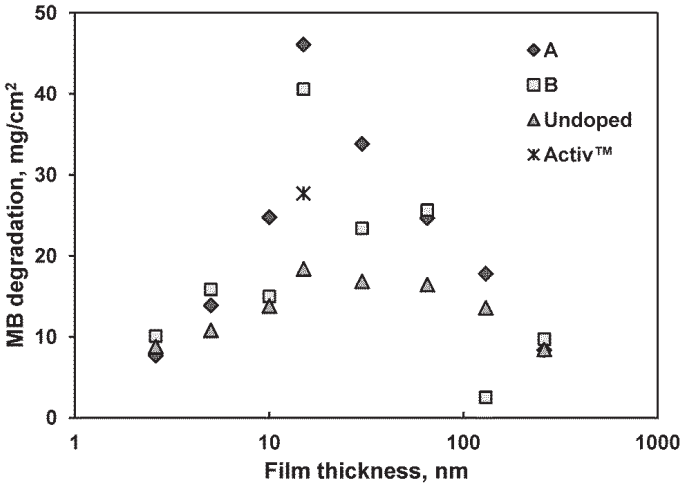

Figure 16. Methylene blue degradation of doped A-Series, doped B-series, and undoped series films (Fig.5,**IV**). *Reprinted with permission from Elsevier ©2009.*

4.4 Zinc release from ALD-grown ZnO thin films and its bactericidal effect on *Escherichia Coli*

ZnO films with various thicknesses were grown on borosilicate glass substrates by atomic layer deposition (ALD) using DEZ and deionized water as precursors at reaction temperatures of 120 °C and 200 °C. An additional series of films at both temperatures were coated with aluminum oxide (Al_2O_3) films of 5 nm, 10 nm, and 15 nm thicknesses (**V**). Trimethylaluminum and deionized water were used at 220°C in Al_2O_3 deposition by ALD. Zinc release from ZnO films was studied by immersing the samples in deionized water and

phosphate buffered saline solution (PBS) which is commonly used as body fluid simulant in biological studies. Two variable tests were performed. The first dissolution took 24 h and zinc containing elution was collected for concentration analysis. A long test took 38 days during elution samples were collected every 24 h. The zinc release was analyzed from the elute-containing solution with inductively coupled plasma mass spectrometry (ICP-OES). The results showed no evidence that the film thickness or ZnO crystal structure would affect the dissolution of zinc from ZnO films (Fig.2,**V**). Using the zinc film density and the sample area the released zinc mass was converted into a decrease in the ZnO film thickness (Figs.3,4,**V**). In figure 3, a plateau shows that the rate of elution has decreased almost to zero at approximately 10 days. It is possible that the 5 nm Al_2O_3 film does not produce complete conformal coverage of the underlying zinc oxide thus the zinc oxide is immediately exposed to the solution at certain points on immersion. The blocking effect becomes clear with 10 nm and 15 nm Al_2O_3 coatings. Aluminum oxide showed an effective buffering effect; only a 10 nm layer buffered the zinc release for 18 days in water and 16 days in PBS (Figs.3,4,**V**). The buffering effect of Al_2O_3 is presented in Figures 17 and 18.

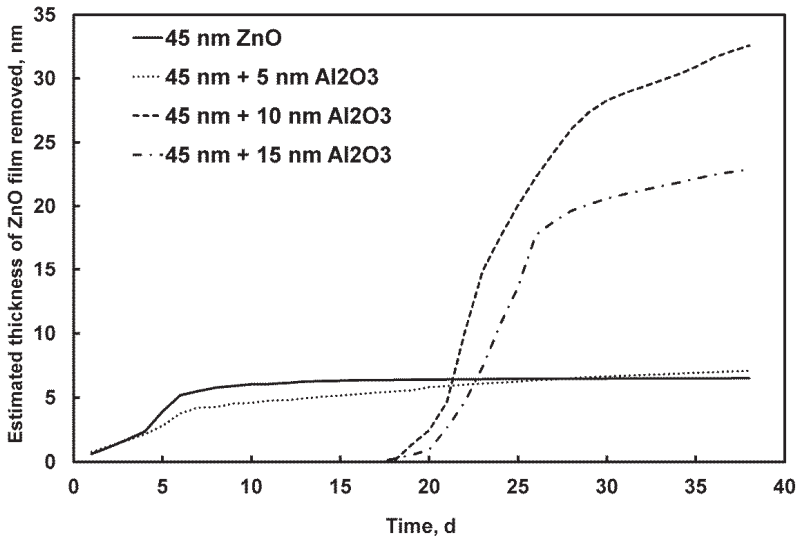

Figure 17. The decrease in ZnO film thickness during the dissolution test in deionized water (Fig.3,**V**).

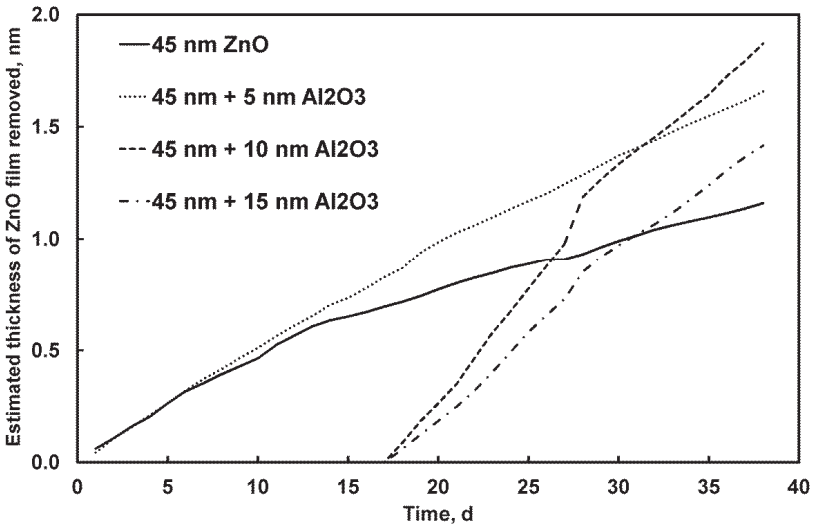

Figure 18. The decrease in ZnO film thickness during the dissolution test in PBS solution (Fig.4,**IV**).

Antimicrobial activity was studied in dark conditions by exposing two different zinc oxide films of 45 nm and 280 nm from 200 °C series for 24 h to a bacteria suspension of 1.5×10^6 CFU/ml of *Escherichia Coli* at 37 °C. The results showed that ZnO films were highly efficient and both 45 nm and 280 nm thick films destroyed *Escherichia Coli* by 99.7% and 99.5%, respectively (Fig.19). The results indicated that photoirradiation is not required for bactericidal effects. The result opposes other studies which have suggested that photocatalytic generation of hydrogen peroxide would be a principal mechanism for antibacterial effect [200,228]. ZnO nanoparticles have also been proposed to destroy bacteria by penetrating the cell envelope [203,204]. In other studies the dissolution of Zn^{2+} ions has been successfully applied [205,206]. Since ALD films do not produce any nanoparticles, the zinc ions are probably responsible for the antibacterial properties of ZnO thin films.

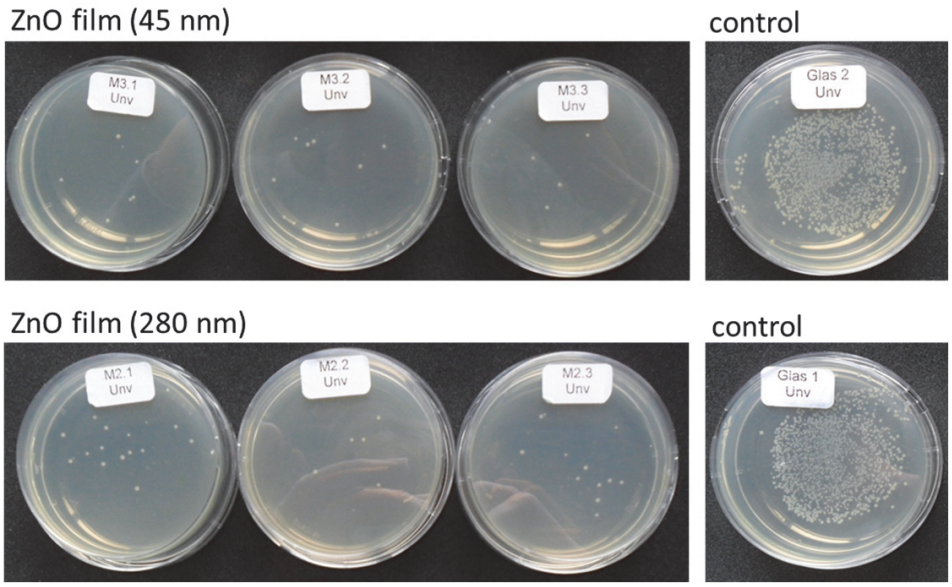

Figure 19. Antimicrobial activity of ZnO films. Images showing *E.coli* colonies (CFUs, colony forming units) on agar plates which have been in contact with ZnO films (45 nm and 280 nm) and borosilicate glass control for 24 h in the dark. (Fig.7,**IV**).

5. Conclusions

ALD grown titanium and zinc oxide thin films have been investigated in photoactivity, photocatalytic activity, and bioactivity measurements. The crystal structure has been shown to be a central factor in the photoactivity and photocatalytic properties of TiO_2. Beside the crystal structure electronic properties are important in determining the performance of a semiconductor. The TiO_2 structure can be modified by doping which cause changes in its resistivity, photoactivity, and photocatalytic performance. ALD grown ZnO films are highly antibacterial. Zinc release from the ZnO film can be the cause for bactericidal effect. Aluminum trioxide can be used as a buffer film to control zinc release from ZnO films efficiently.

The most critical factor for obtaining a highly active titanium dioxide photocatalyst is the optimization of the anatase/rutile phase ratio. The anatase/rutile ratio changes when TiO_2 film thickness increases. Consequently the film thickness is not important itself but significant due

to the effect on the TiO_2 crystal structure. The highest performance in both photoactivity and photocatalytic activity can be observed with films which consisted of preponderantly anatase phase and small amount of the rutile phase.

A relation between majority carrier polarity and crystal structure has been discovered. The polarity of the anatase-dominant films has been demonstrated to be p-type whereas the rutile dominant films are always n-type. It is proposed that the superior photocatalytic property of the anatase dominant mixture of phases is due to the formation of p-n junctions in the TiO_2. When the irradiation energy excites electrons to the anatase conduction band, the p-n junction then allows them to transfer to the rutile conduction band which is at a lower energy. In contrast the holes will transfer from the rutile valence band to the anatase valence band. This results in the spatial separation of electrons and holes and in reduced recombination.

Nitrogen doping has been found to improve the photocatalytic performance of TiO_2 films. However the photoactivity was reduced by N-doping especially in rutile dominant films. N-doping did not cause any changes in the majority carrier polarity of anatase and rutile. The film resistivity measurements showed that the doped TiO_2 films have higher conductivity than the undoped TiO_2 films.

Zinc release has found to take place from ALD grown ZnO films when immersed in water or PBS solution. ZnO films have proven to be highly antibacterial in dark conditions needing no photoirradiation. Therefore it is probable that the Zn^{2+} -ion is the major factor in the antibacterial mechanism. ALD grown Al_2O_3 film has proven to be an efficient buffer layer for zinc dissolution. A combination of controlled ZnO and Al_2O_3 thin films can be used to determine a time sequence of antibacterial activity and the onset of the activity can be delayed by the thickness of the Al_2O_3 layer. These results also indicate that a multilayer nanolaminate structure of alternating ZnO and Al_2O_3 films could be used to tailor a complex sequence of high and low antibacterial activity which would be useful in medical applications.

The results in this work show the importance of understanding the structure of materials and its relation to various properties. The applied ALD thin films are often on a nanometer scale which determines higher requirements for the testing and material characterization methods. Mathematical modeling for reconstructing material surfaces and structures are of great

support for understanding experimental results. In addition, comprehension of electrical properties and their relation to surface and bulk structure have become even more significant.

It is known that temperature and substrate material affect the growth and crystalline structure of ALD deposited films. This has been realized also in this work where different deposition temperatures and substrates have been applied for TiO_2 and ZnO films. Nevertheless there is a wide range of temperatures and substrate materials to be investigated more thoroughly in the near future. The low temperature deposition range has become important in recent years due to the applications in flexible and paper-based electronics. In addition air and water purification processes use often polymer or cellulose membrane materials where low temperature ALD-coatings can be applied. Antibacterial coatings and medical applications are another growing area where effective films are needed. ALD offers opportunities in a wide range of applications but concurrently each case needs intensive detailed research work.

References

1. Material Safety Data Sheet, Titanium dioxide MSDS, ScienceLab.com, viewed 15 December, 2012, http://www.sciencelab.com/msds.php?msdsId=9925268

2. C. Renz, Helv. Chim. Acta 15 (1932) 1077.

3. C.F. Goodeve, J.A. Kitchener, Trans. Faraday Soc. 34 (1938) 570.

4. K.V. Giri, G.D. Kalyankar, C.S. Vaidyanathan, Naturwissenschaften 40 (1953) 440.

5. A. Fujishima a, X. Zhang, D.A. Tryk, Surf. Sci. Rep. 63 (2008) 515.

6. A. Fujishima, K. Honda, Nature 238 (1972) 38.

7. M.A. Fox, M.T. Dulay, Chem. Rev. 93 (1993) 341.

8. A.L. Linsebigler, G. Lu, J.T. Yates Jr., Chem. Rev. 95 (1995) 735.

9. S.T. Martin, A.T. Lee, M.R. Hoffmann, Environ. Sci. Technol. 29 (1995) 2567.

10. M.R. Hoffmann, S.T. Martin, W. Choi, D.W. Bahnemann, Chem. Rev. 95 (1995) 69.

11. A. Fujishima, X. Zhang, C. R. Chimie 9 (2006) 750.

12. Y. Du, J. Rabani, J. Phys. Chem. B 107 (2003) 11970.

13. R.Wang, K. Hashimoto, A. Fujishima, M. Chikuni, E. Kojima, A. Kitamura, M. Shimohigoshi, T. Watanabe, Nature 388 (1997) 431.

14. A. Fujishima, K. Hashimoto, T. Watanabe, TiO2 Photocatalysis: Fundamentals and Applications, BKC, Tokyo, 1999.

15. A. Fujishima, T.N. Rao, D.A. Tryk, J. Photochem. Photobiol.C Rev. 1 (2000) 1–21.

16. Y. Taga, Thin Solid Films 517 (2009) 3167–3172.

17. L.-S. Zhang, K.-H. Wong, H.-Y. Yip, C. Hu , J.C. Yu, C.-Y. Chan, P.-K. Wong, Environ. Sci. Technol. 44 (2010) 1392.

18. B. O'Regan, M. Grätzel, Nature 353 (1991) 737.

19. M. Grätzel, Nature 414 (2001) 338.

20. D. Shchukin, S. Poznyak, A. Kulak, P. Pichat, J. Photochem. Photobiol. A 162 (2004) 423.

21. G. Li Puma, J.N. Knor, A. Brucato, Environ. Sci. Technol. 38 (2004) 3737.

22. G. Balasubramanian, D.D. Dionysiou, M.T. Suidan, I. Baudin, J.-M. Laîné, J. Mater. Sci. 38 (2003) 823.

23. M.A. Ferguson, J.G. Hering, Environ. Sci. Technol. 40 (2006) 4261.

24. A.W. Morawski, M. Janus, B. Tryba, M. Toyoda, T. Tsumura, M. Inagaki, Pol. J. Chem. Technol. 11 (2009) 46.

25. F. M. Monteiro Paschoal, G. Pepping, M.V. Boldrin Zahoni, M.A. Zahoni, Environ. Sci. Technol. 43 (2009) 7496.

26. A. Hagfeldt, M. Grätzel, Chem. ReV. 95 (1995) 49.

27. M. Grätzel, Nature 414 (2001) 338.

28. M. Grätzel, J. Photochem. Photobiol. C: Photochem. Rev. 4 (2003) 145.

29. M. Grätzel, Inorg. Chem. 44 (2005) 6841.

30.W. Yen, C. Hsieh, C. Hung, H.H.-W. Wang, M. Tsui, J. Chin. Chem. Soc. 57 (2010) 1162.

31. F. Wu, H. Lan, Z. Zhang, P. Cui, J. Chem. Phys. 137 (2012) 104702.

32. K.-S. Lee, J.-W. Lim, H.-K. Kim, T.L. Alford, G.E. Jabbour, Appl. Phys. Lett. 100 (2012) 213302.

33. U. Kirner, K.D. Schierbaum, W. Göpel, B. Leibold, N. Nicoloso, W. Weppner, D. Fischer, W.F. Chu, Sens. Actuators B 1 (1990) 103.

34. N. O. Savage, S. A. Akbar, P. K. Dutta, Sens. Actuators B 72 (2001) 239.

35. G. S. Devi, T. Hyodo, Y. Shimizu, M. Egashira, Sens. Actuators B 87 (2002) 122.

36. L. Zheng, M. Xu, T. Xu, Sens. Actuators B 66 (2000) 28.

37. O. Landau, A. Rothschild, Sens. Actuators B 171-172 (2012) 118.

38. B. Karunagaran, P. Uthirakumar, S.J. Chung, S. Velumani, E.-K. Suh, Mater. Charact. 58 (2007) 680.

39. H. Tang, K. Prasad, R. Sanjinès, P.E. Schmid, F. Lévy, J. Appl. Phys. 75 (1994) 2042.

40. Chen, S.S. Mao, Chem. Rev. **2007,** 107, 2891.

41. L. Brus, J. Phys. Chem. 90 (1986) 2555.

42. C. Kormann, D.W. Bahnemann, M.R. Hoffmann, J. Phys. Chem. 92 (1988) 5196.

43. Y. Li, T.J. White, S.H. Lim, J. Solid State Chem. 177 (2004) 1372.

44. K.M. Reddy, C.V.G. Reddy, S.V.J. Manorama, Solid State Chem. 158 (2001) 180.

45. S. Monticone, R. Tufeu, A.V. Kanaev, E. Scolan, C. Sanchez,
Appl. Surf. Sci. 162-163 (2000) 565.

46. C. Buzea, I.I. Pacheco Blandino, K. Robbie, Biointerphases 2 (2007) MR17.

47. Zinc oxide, viewed 16 December 2012, http://en.wikipedia.org/wiki/Zinc_oxide

48. C.F. Klingshirn, B.K. Meyer, A. Waag, a. Hoffmann, J. Geurts, *Zinc Oxide: From Fundamental Properties Towards Novel Applications*, Springer-Verlag, Berlin Heidelberg, 2010.

49. L. Wang, Y. Zheng , X. Li, W. Dong, W. Tang, B. Chen, C. Li, X. Li, T. Zhang, W. Xu, Thin Solid Films 519 (2011) 5673.

50. S.A. Ruffolo , M.F. La Russa , M. Malagodi, C. Oliviero Rossi , A.M. Palermo, G.M. Crisci, Appl Phys A 100 (2010) 829.

51. R. Theissmann, S. Bubel, M. Sanlialp, C. Busch, G. Schierning, R. Schmechel, Thin Solid Films 519 (2011) 5623.

52. A. Di Trolio, E. M. Bauer, G. Scavia, C. Veroli, J. Appl. Phys 105 (2009) 113109.

53. J. H. Shi, S. M. Huang, J. B. Chu, H. B. Zhu, Z. A. Wang, X. D. Li, D. W. Zhang, Z. Sun, W. J. Cheng, F. Q. Huang, X. J. Yin, J. Mater. Sci.: Mater Electron 21 (2010) 1005.

54. H. Cheun, C. Fuentes-Hernandez, J. Shim, Y. Fang, Y. Cai, H. Li, A.K. Sigdel, J. Meyer, J. Maibach, A. Dindar, Y. Zhou, J.J. Berry, J.-L. Bredas, A. Kahn, K. H. Sandhage, B. Kippelen, Adv. Funct. Mater. 22 (2012) 1531.

55. K. Nomura, H. Ohta, K. Ueda, T. Kamiya, M. Hirano, H. Hosono, Science 300 (2003) 1269.

56. S. J. Pearton, W. H. Heo, M. Ivill, D. P. Norton, T. Steiner, Semicond. Sci. Technol. 19, (2004) R59.

57. H.-W. Ryu, B.-S. Park, S. A. Akbar, W.-S. Lee, K.-J. Hong, Y.-Jin Seo, D.-C. Shin, J.-S. Park, G.-P. Choi, Sens. Actuator 717 (2003) B 96.

58. G. Sberveglieri, Sens. Actuator 103 (1995) B 23.

59. G.S.T. Rao, D.T.Rao, Sens. Actuator B 55 (1999) 166.

60. X. L. Cheng, H. Zhao, L. H. Huo, S. Gao, J. G. Zhao, Sens. Actuator B 102 (2004) 248.

61. K. Kato, H. Omoto, A. Takamatsu, Adv. Mater. Res.117 (2010) 69.

62. X.Y. Du, Y.Q. Fu, S.C. Tan, J.K. Luo, A.J. Flewitt, S. Maeng, S.H. Kim, Y.J. Choi, D.S. Lee, N. M. Park, J. Park, W.I. Milne, Journal of Physics: Conference Series 76 (2007) 012035.

63. Q.J. Wang, C. Pflügl, W.F. Andress, D. Ham, F. Capasso, M. Yamanishi, J. Vac. Sci. Technol. B 26 (2008) 6.

64. V. B. Aleskovskii, J. Appl. Chem. USSR. 47 (1974) 2207.

65. T. Suntola, J. Antson, U.S. Patent 4,058,430, 1977.

66. ASTRaL (Advanced Surface Technology Research Laboratory), viewed 2 March 2013, http://www.lut.fi/web/en/lut-savo-sustainable-technologies/astral

67. M. Ritala, M. Leskelä, in: H.S. Nalwa (Ed.), Handbook of Thin Film Materials, vol. 1, Academic Press, New York, 2002, p. 103.

68. R. Puurunen, J. appl. Phys. 97 (2005) 121301.

69. S.M. George, Chem. Rev. 110 (2010) 111.

70. V. Miikkulainen, M. Leskelä, M. Ritala, R. Puurunen, J. Appl. Phys. 113 (2013) 021301.

71. T. Kääriäinen, D. Cameron, M.-L. Kääriäinen, and A. Sherman, *Atomic Layer Deposition; Principles, Characteristics, and Nanotechnology Applications*, 2nd Ed. , Co-published by John Wiley & Sons, Inc. Hoboken, New Jersey, and Scrivener Publishing LLC, Salem, Massachusetts, 2013.

72. Titanium dioxide, viewed 11 January 2013, http://monographs.iarc.fr/ENG/Monographs/vol93/mono93-7A.pdf

73. U. Diebold, Appl. Phys. A 76 (2002) 1.

74. U. Diebold, Surf. Sci. Rep. 48 (2003) 53.

75. M. Ramamoorthy, D. Vanderbilt, Phys. Rev. B 49 (1994) 16721.

76. U. Martinez, J.Ø. Hansen, E. Lira, H.H. Kristoffersen, P. Huo, R. Bechstein, E. Lægsgaard, F. Besenbacher, B. Hammer, S. Wendt, Phys. Rev. Lett. 109 (2012) 155501.

77. File:Rutile-122157.jpg, viewed 20 December 2012, http://en.wikipedia.org/wiki/File:Rutile-122157.jpg

78. File:Anatase Oisans.jpg, viewed 20 December 2012, http://en.wikipedia.org/wiki/File:Anatase_Oisans.jpg

79. V.E. Henrich, P.A. Cox, The Surface Science of Metal Oxides, Cambridge Univ. Press, Cambridge, 1994.

80. H.J. Freund, Faraday Discuss. 114 (1999) 1-31.

81. G. Pacchioni, Surf. Sci. 281 (1993) 207.

82. S.C. Petitto, E.M. Marsh, M.A. Langell, J. Phys. Chem. B 110 (2006) 1309.

83. C.C. Chusuei, X. Lai, K. Luo, D.W. Goodman, Top. Catal. 14 (2001) 71.

84. L.P.Zhang, M. Li, U. Diebold, Surf. Sci. 412 (1998) 242.

85. U. Diebold, J. Lehman, T. Mahmoud, M. Kuhn, G. Leonardelli,W. Hebenstreit, M. Schmid, P. Varga, Surf. Sci. 411 (1998) 137.

86. R. Hengerer, B. Bolliger, M. Erbudak, M. Grätzel, Surf. Sci. 460 (2000) 162.

87. G.E. Jellison, L.A. Boatner, J.D. Budai, B.S. Jeong, D.P. Norton,J. Appl. Phys. 93 (2003) 9537.

88. S. Auvinen, M. Alatalo, H. Haario, J.-P. Jalava, R.-J. Lamminmäki, J. Phys. Chem. C 115 (2011) 8484.

89. M. Lazzeri, A. Vittadini, A. Selloni, Phys. Rev. B 63 (2001) 155409.

90. M. Lazzeri, A. Vittadini, A. Selloni, Phys. Rev. B 65 (2002) 119901.

91. W. Hebenstreit, N. Ruzycki, G.S. Herman, Y. Gao, U. Diebold, Phys. Rev. B 64 (2000) R16344.

92. X.-Q. Gong, A. Selloni, M. Batzill, U. Diebold, Nat. Mater. 5 (2006) 665.

93. A. Beltran, L. Gracia, J. Andres, J. Phys. Chem. B 110 (2006) 23417.

94. K. Komaguchi, T. Maruoka, H. Nakano, I. Imae, Y. Ooyama, Y. Harima, J. Phys. Chem. C 114 (2010) 1240.

95. R. Schaub, P. Thostrup, N. Lopez, E. Lægsgaard, I. Stensgaard, J.K. Nørskov, F. Besenbacher, Phys. Rev. Lett. 87 (2001) 266104.

96. A. Vittadini, A. Selloni, F.P. Rotzinger, M. Grätzel, Phys. Rev. Lett. 81 (1998) 2954.

97. M. Egashira, S. Kawasumi, S. Kagawa, T. Seiyama, Bull. Chem. Soc. Jpn. 51 (1978) 3144.

98. G.S. Herman, Y. Gao, Thin Solid Films 397 (2001) 157.

99. L.-M. Liu, C. Zhang, G. Thornton, A. Michaelides, Phys. Rev. B 82 R(2010) 161415.

100. F. Filippone, G. Mattioli, A.A. Bonapasta, Catal. Today 129 (2007)169.

101. U. Aschauer, J. Chen, A. Selloni, Phys. Chem. Chem. Phys. 12 (2010)12956.

102. L. Zhang, H. Ji, Y. Lei, W. Xiao, Appl. Surf. Sci. 257 (2011) 8402.

103. C.L. Muhich, Y. Zhou, A.M. Holder, A.W. Weimer, C.B. Musgrave, J. Phys. Chem. C 116 (2012) 10138.

104. N. Serpone, D. Lawless, R. Khairutdinov, J. Phys. Chem. 99 (1995) 16646.

105. L. Forro, O. Chauvet, D. Emin, L. Zuppiroli, H. Berger, F.Lévy, J. Appl. Phys. 75 (1994) 633.

106. H. Tang, F. Lévy, H. Berger, and P.E. Schmid, Phys. Rev. B **52** (1995) 7771.

107. N.A.Deskins and M. Dupuis, Phys. Rev. B 75 (2007) 195212.

108. N. A. Deskins and M. Dupuis, J. Phys. Chem. C 113 (2009) 346.

109. M.D. Earle, Phys. Rev. 61 (1942) 56.

110. C. Shifu, Z. Wei, L. Wei, Z. Sujuan, Appl. Surf. Sci. 255 (2008) 2478.

111. N. Savage, B. Chwieroth, A. Ginwalla, B.R. Patton, S.A. Akbar, P.K. Dutta, Sens. Actuators, B 79 (2001) 17.

112. F. Hossein-Babaei, M. Keshmiri, M. Kakavand, T. Troczynski, Sens. Actuators B 110 (2005) 28.

113. Q. Li, X. Wang, Z. Jin, D. Yang, S. Zhang, X. Guo, J. Yang, Z. Zhang, J. Nanopart. Res. 9 (2007) 951.

114. B.-S. Jeong, D.P. Norton, J.D. Budai, Solid State Electron. 47 (2003) 2275.

115. R.A. Palmer, T.M. Doan, P.G. Lloyd, B.L. Jarvis, N.U. Ahmed, Plasma Chem. Plasma P. 22 (2002) No. 3.

116. A. Yildiz, S.B. Lisesivdin, M. Kasap, D. Mardare, J. Non-Cryst. Solids 354 (2008) 4944.

117. N.A. Rasheid, M.K. Ahmad, M. Rusop, CP1136, *Nanoscience and Nanotechnology,* International Conference on Nanoscience and Nanotechnology, (NANO-Sci-Tech 2008), (eds.) M. Rusop and T. Soga, 2009 American Institute of Physics.

118. M. Ritala, M. Leskelä, E. Nykänen, P. Soininen, L. Niinistö, Thin Solid Films 225 (1993) 288.

120. M. Ritala, M. Leskelä, L. Niinistö, P. Haussalo, Chem. Mater. 5 (1993) 1174.

121. J. Aarik, A. Aidla, T.Uustare, V. Sammelselg, J. Crystal Growth 148 (1995) 268.

122. K.S. Finnie, G. Triani, K.T. Short, D.R.G. Mitchell, D.J. Attard, J.R. Bartlett, C.J. Barbe, Thin Solid Films 440 (2003) 109.

123. D.R.G. Mitchell, D.J. Attard, G. Triani, Thin Solid Films 441 (2003) 85.

124. R. Matero, A. Rahtu, and M. Ritala, Chem. Mater. 13(2001) 4506.

125. N. G. Kubala, P.C. Rowlette, C.A. Wolden, J. Phys. Chem. C 113 (2009) 16307.

126. N. G. Kubala, C. A. Wolden, Thin Solid Films 518 (2010) 6733.

127. K. Kukli, M. Ritala, M. Schuisky, M. Leskelä, T. Sajavaara, J. Keinonen, T.Uustare , A. Hårsta, Chem. Vap. Deposition 6 (2000) 303.

128. K. Kukli, A. Aidla, J. Aarik, M. Schuisky, A. Hårsta, M. Ritala and M. Leskela, Langmuir 16 (2000) 8122.

129. J. Aarik, A. Aidla, T. Uustare, K. Kukli, V. Sammelselg, M. Ritala, M. Leskelä, Appl. Surf. Sci. 193 (2002) 277.

130. M. Schuisky, J. Aarik, K. Kukli, A. Aidla and A. Hårsta, Langmuir 17 (2001) 5508.

131. V. Pore, T. Kivelä, M. Ritala, M. Leskelä, Dalton Trans. (2008) 6467.

132. V.R. Rai and S. Agarwal, J. Phys. Chem. C Lett. 112 (2008) 9552.

133. A. Niskanen, K. Arstila, M. Leskelä, M. Ritala, Chem. Vap. Deposition 13 (2007) 152.

134. J. Aarik, J. Karlis, H. Mändar, T. Uustare, V. Sammelselg, Appl. Surf. Sci. 181 (2001) 339.

135. V. Pore, A. Rahtu, M. Leskela, M. Ritala, T. Sajavaara, J. Keinonen, Chem. Vap. Deposition 10 (2004) 143.

136. I. Jõgi, M. Pärs, J. Aarik, A. Aidla, Matti Laan, J. Sundqvist, L. Oberbeck, J. Heitmann, K. Kukli, Thin Solid Films 516 (2008) 4855.

137. A.P. Alekhin, S.A. Gudkova, A.M. Markeev, A.S. Mitiaev, A.A.Sigarev, V.F. Toknova, Appl. Surf. Sci. 257 (2010) 186.

138. H. Y. Jeong, Y. I. Kim, J. Y. Lee, S. Y. Choi, Nanotechnology 21 (2010) 115203.

139. Q. Xie, Y.-L. Jiang, C. Detavernier, D. Deduytsche, and R. L. Van Meirhaeghe, G.-P. Ru, B.-Z. Li, X.-P. Qu, J. Appl. Phys. 102 (2007) 083521.

140. Q. Xie, J. Musschoot, D. Deduytsche, R. L. Van Meirhaeghe, C. Detavernier, S.Van den Berghe, Y.-L. Jiang, G.-P. Ru, B.-Z. Li, X.-P. Qu, J. Electrochem.Soc. 155 (2008) H688.

141. C.-S. Lee , J. Kim, J.Y. Son, W. Choi, H. Kim, Appl. Catal. B 91 (2009) 628.

142. C.-S. Lee, J. Kim, G.H. Gu, D.-H. Jo, C.G. Park, W. Choi, H. Kim, Thin Solid Films 518 (2010) 4757.

143. T.O.Kääriäinen, D.C. Cameron, M. Tanttari, Plasma Process. Polym. 6 (2009) 631.

144. A. Sarkar, S.E. Pitts, S.A. Rushworth, F. Roozeboom, M.C.M. van den Sanden, W.M.M. Kessels, ECS Transact. 33 (2010) 385.

145. J. Niinistö, T. Hatanpää, M. Kariniemi, M. Mäntymäki, L. Costelle, K. Mizohata, K. Kukli, M. Ritala, M. Leskela, Chem. Mat. 24 (2012) 2002.

146. I. Jõgi, J. Aarik, M. Laan, J. Lu, K. Kukli, H. Kaambre, T. Sajavaara, T. Uustare, Thin Solid Films 510 (2006) 39.

147. H.B. Profijt, S.E. Potts, M.C.M. van de Sanden, W.M.M. Kessels, J. Vac. Sci. Technol.A 29 (2011) 050801-1.

148. T.O. Kääriäinen, S. Lehti, M.-L. Kääriäinen, D.C. Cameron, Surf. Coat. Tech. 205, S475 (2011) S475.

149. V. Pore, 2010, *Atomic Layer Deposition and Photocatalytic Properties of Titanium Dioxide Thin Films*, PhD thesis, ISBN 978-952-10-6284-1 (PDF version).

150. H. Zhang, J.F. Banfield, J. Mater. Chem. 8 (1998) 2073.

151. H. Zhang, J.F. Banfield, J. Phys. Chem. B 104 (2000) 3481.

152. P.K. Naicker, P.T. Cummings, H. Zhang, J.F. Banfield, J. Phys. Chem. B 109 (2005) 15243.

153. Y. Nosaka, M.A. Fox, J. Phys. Chem. 92 (1988) 1893.

154. The Photochemistry Portal, viewed 15 January 2013, http://photochemistryportal.net/home/index.php/category/semi-conductor-photocatalysis/

155. D.W. Bahnemann, M. Hilgendorff, R. Memming, J. Phys. Chem. B 101 (1997) 4265.

156. J. Nelson, A.M. Eppler, I.M. Ballard, J. Photochem. Photobiol. A Chem. 148 (2002) 25.

157. R. Nakamura, Y. Nakato, J. Am. Chem. Soc. 126 (2004) 1290.

158. C. Di Valentin, G. Pacchioni, A. Selloni, Phys. Rev. Lett. 97 (2006) 166803.

159. N. Sakai, A. Fujishima, T. Watanabe, K. Hashimoto, J. Phys. Chem. B 107 (2003) 1028.

160. S. Kerisit, N.A. Deskins, K.M. Rosso, M. Dupuis, J. Phys. Chem. C 112 (2008) 7678.

161. B.L. Abrams and J.P. Wilcoxon, Crit. Rev. Solid State 30 (2005) 153.

162. X. Chen and S.S. Mao, Chem. Rev. 107 (2007) 2891.

163. H. Tada, M. Tanaka, Langmuir 13 (1997) 360.

164. M. Tazawa, M. Okada, K. Yoshimura, I. Ikezawa, Sol. Energy Mater. Sol. Cells 84 (2004) 159.

165. R.I. Bickley, T. Gonzalez-Carreno, J.T. Lees, L. Palmisano, R.J. Tilley, J. Solid State Chem. 92 (1991) 178.

166. A. Datye, G. Riegel, J.R. Bolton, M. Huang, M.R. Prairie, J. Solid State Chem. 115 (1995) 236.

167. Z. Ding, G.Q. Lu, P.F. Greenfield, J. Phys. Chem. B 104 (2000) 4815.

168. T. Ohno, K. Sarukawa, K. Tokieda, M. Matsumura, J. Catal. 203 (2001) 82.

169. T. Kawahara, Y. Konishi, H. Tada, N. Tohge, J. Nishii, S. Ito, Angew. Chem., Int. Ed. 41 (2002) 2811.

170. T. Kawahara, T. Ozawa, M. Iwasaki, H. Tada, S. Ito, J. Colloid Interf. Sci. 267 (2003) 377.

171. T. Ohno, K. Tokieda, S. Higashida, M. Matsumura, Appl. Catal., A 244 (2003) 383.

172. B. Sun, P.G. Smirniotis, Catal. Today 88 (2003) 49.

173. A.G. Agrios, K.A. Gray, E. Weitz, Langmuir 19 (2003) 1402.

174. D.C. Hurum, A.G. Agrios, K.A. Gray, J. Phys. Chem. B 107 (2003) 4545.

175. C.Y. Wu, Y.H. Yue, X.Y. Deng, W.M. Hua, Z.Gao, Catal.Today 93-95 (2004) 863.

176. S. Bakardjieva, J. Šubrt, V. Štengl, M.J. Dianez, M.J. Sayagues, Appl. Catal. B 58 (2005) 193.

177. M.C. Yan, F. Chen, J.L. Zhang, M. Anpo, J. Phys. Chem. B 109 (2005) 8673.

178. K. Komaguchi, H. Nakano, A. Araki, Y. Harima, Chem. Phys.Lett. 428 (2006) 338.

179. Z. Liu, X. Zhang, S. Nishimoto, M. Jin, D.A. Tryk, T. Murakami, A. Fujishima, Langmuir 23(2007) 10916.

180. S. Livraghi, M.C. Paganini, E. Giamello, A. Selloni, C. Di Valentin, G. Pacchioni, J. Am. Chem. Soc. 128 (2006) 15666.

181. X. Nie, S. Zhuo, G. Maeng, K. Sohlberg, Int. J. Photoenergy (2009), Art. ID 294042, 22 pages.

182. N. Serpone, A.V. Emeline, V.N. Kuznetsov, V.K. Ryabchuk, Chapter 3 in: Environmentally Benign Photocatalysts; Applications of Titanium Oxide-based materials, M. Anpo, P.V. Kamat (Eds.), Springer Science+Business Media, LLC 2010, pp. 35-111.

183. M. Pelaeza, N.T. Nolan, S.C. Pillai, M.K. Seery, P. Falaras, A.G. Kontos, P.S.M. Dunlop, J.W.J. Hamilton, J.A. Byrnee, K. O'Sheaf, M.H. Entezarig, D.D. Dionysioua, Appl. Catal. B-Environ. 125 (2012) 331.

184. C. Di Valentin, G. Pacchioni, A. Selloni, S. Livraghi, E. Giamello, J. Phys. Chem. B, 109 (2005) 11414.

185. R. Asahi, T. Morikawa, T. Ohwaki, K. Aoki, Y. Taga, Science 293 (2001) 269.

186. C. Di Valentin, E. Finazzi, G. Pacchioni, A. Selloni, S. Livraghi, M.C. Paganini, E. Giamello, Chem. Phys. 339 (2007) 44.

187. V. Pore, M. Heikkilä, M. Ritala, M. Leskelä, S. Areva, J. Photochem. Photobiol. A 177 (2006) 68.

188. S. Limpijumnong, S. Jungthawan, Phys. Rev. B 70 (2004) 054104.

189. J. Serrano, A.H. Romero, F.J. Manjón, R. Lauck, M. Cardona, A. Rubio, Phys. Rev. B 69 (2004) 094306.

190. File:Wurtzite polyhedra.png, viewed January 13 2013, http://en.wikipedia.org/wiki/File:Wurtzite_polyhedra.png

191. S. Baruah and J. Dutta, Sci. Technol. Adv. Mater. 10 (2009) 013001.

192. Zinc oxide, viewed January 13 2013, http://en.wikipedia.org/wiki/Zinc_oxide

193. S. Liang, H. Sheng, Y. Liu, Z. Hio, Y. Lu, H. Chen, J. Cryst. Growth 225 (2001) 110.

194. N. Saito, H. Haneda, T. Sekiguchi, N. Ohashi, I. Sakaguchi, K. Koumoto, Adv. Mater. 14 (2002) 418.

195. J.Y. Lee, Y.S. Choi, J.H. Kim, M.O. Park, S. Im, Thin Solid Films 403 (2002) 533.

196. A. Sugunan, H.C. Warad, M. Bomand, J. Dutta, J. Sol–Gel Sci. Technol. 39 (2006) 49.

197. Ü. Özgür, Y.I. Alivov, C. Liu, A. Teke, M.A. Reshchikov, S. Doğan, V.Avrutin, S.-J. Cho, H. Morkoç, J. Appl. Phys. 98 (2005) 041301.

198. Z.Q. Chen, K. Betsuyaku, A. Kawasuso, Phys. Rev. B 77 (2008) 113204.

199. H. Noor, P. Klason, O. Nur, Q. Wahab, M. Asghar, M. Willander, J. Appl. Phys. 105 (2009) 123510.

200. J. Sawai, J Microbiol. Methods 54 (2003) 177.

201. L.K. Adams, D.Y. Lyon, P.J.J Alvarez, Water Res. 40 (2006) 3527.

202. N. Jones,B. Ray,K.T. Ranjit, A.C. Manna, FEMS Microbiol. Lett. 279 (2008) 71.

203. Z. Huang, X. Zheng, D. Yan,G. Yin, X. Liao, Y. Kang, Y. Yao, D. Huang, B. Hao, Langmuir 24, (2008) 4140.

204. Y. Liu, L. He, A. Mustapha, H. Li, Z.Q. Hu, M. Lin, J. Appl. Microbiol. 107 (2009) 1193.

205. N.M Franklin, N.J. Rogers, S.C. Apte, G.E. Batley, G.E. Gadd, P.S. Casey, Environ. Sci. Technol. 41 (2007) 8484.

206. T. Xia, M. Kovochich, M. Liong, L. Madler, B. Gilbert, H. Shi, J.I. Yeh, J.I. Zink, A.E. Nel, ACS Nano 2 (2008) 2121.

207. J.W. Moreau, P.K. Weber, M.C. Martin, B. Gilbert, I.D. Hutcheon, J.F. Banfield, Science 316 (2007) 1600.

208. P. Bhadra, M.K. Mitra, G.C. Das, R. Dey, S. Mukherjie, Int. J. Eng. Sci. Technol. (2012) 4223.

209. D.M. King, X. Liang, C.S. Carney, L.F. Hakim, P. Li, A.W. Weimer, Adv. Funct. Mater. 18 (2008) 607.

210. Y.S. Kim, Y.S. Won, H. Hagelin-Weaver, N. Omenetto, T. Anderson, J. Phys. Chem. A 112 (2008) No. 18.

211. S.K. Kim, C.S. Hwang, S.-H. K. Park, S.J.Yun, Thin Solid Films 478 (2005) 103.

212. J. Lim, C. Lee, J. Alloys Compd. 449 (2008) 371.

213. S.J. Lim, S. Kwon, H. Kim, Thin Solid Films 516 (2008) 1523.

214. D.D. Fong, J.A. Eastman, S.K. Kim, T.T. Fister, M.J. Highland, P.M. Baldo, P.H. Fuoss, Appl. Phys. Lett. (2010) 191904.

215. R.L. Puurunen and W. Vandervorst, J. Appl. Phys. 96 (2004) 7686.

216. E. Guziewicz, M. Godlewski, T.A. Krajewski, Ł. Wachnicki, G. Łuka, W. Paszkowicz, J.Z. Domagała, E. Przezdziecka, E. Łusakowska, B.S. Witkowski, Acta Phys. Pol. A116 (2009) 814.

217. E. Guziewicz, M. Godlewski, T.A. Krajewsk, Ł. Wachnicki, G. Łuka, J.Z. Domagała, W. Paszkowicz. B.J. Kowalski, B.S. Witkowski, A. Dużyńska2, A. SuchockiPhys. Stat. Solid. B 247 (2010) No. 7.

218. E. Guziewicz, M. Godlewski, L. Wachnicki, T.A. Krajewski, G. Łuka, S. Gieraltowska, R. Jakiela, A. Stonert, W. Lisowski, M. Krawczyk, J.W. Sobczak, A. Jablonski, Semicond. Sci. Technol. 27 (2012) 074011.

219. J. Jur , W.J. Sweet III, C. J. Oldham , G.N. Parsons, Adv. Funct. Mater. 21 (2011) 1993.

220. P. Scherrer, Göttinger Nachrichten Gesell., 2 (1918) 98.

221. J. Tauc, R. Grigorovici, A. Vancu, Phys. Stat. Sol., 15 (1966) 627.

222. J. Tauc, A. Menth, J. Non-Cryst. Solids, 8-10 (1972) 569.

223. B. Van Zeghbroeck, Principles of Semiconductor Devices, viewed August 20th 2011, http://ecee.colorado.edu/~bart/book/.

224. W.E. Farneth, R.S. McLean, J.D. Bolt, E. Dokou, M.A. Barteau, Langmuir 15 (1999) 8569.

225. J. Sheng, L. Shivalingappa, J. Karasawa, T. Fukami, J. Mater. Sci. 34 (1999) 6201.

226. N. Savage, B. Chwieroth, A. Ginwalla, B.R. Patton, S.A. Akbar, P.K. Dutta, Sens. Actuators, B 79 (2001) 17.

227. Z. Zhang, C. Shao, X. Li, C. Wang, M. Zhang, Y. Liu, Appl. Mater. Interface. 2 (2010) 2915.

228. J. Sawai J. Ferment. Bioeng. 86 (1998) 521.

Paper I

TiO_2 thin films and doped TiO_2 nanolaminates, their structure and its effect on their photoactivity and photocatalytic properties

M.-L. Kääriäinen, T. Kääriäinen, D.C. Cameron, 50th Annual Technical Conference Proceedings, Society of Vacuum Coaters (2007), 335-339.

Reprinted with permission from the Society of Vacuum Coaters

TiO_2 Thin Films and Doped TiO_2 Nanolaminates, Their Structure and its Effect on Their Photocatalytic Properties

M.-L. Kääriäinen, T. Kääriäinen, and D.C. Cameron,
ASTRaL, Lappeenranta University of Technology, Mikkeli, Finland

ABSTRACT

Atomic Layer Deposition (ALD) has been used to deposit undoped, doped and nanolaminate structures based on titanium dioxide and the dependence of their photocatalytic activity on the film structure has been studied. The activity of undoped films has been found to reach its peak at a certain film thickness. The reason for this may be the quantum size effect. Titanium dioxide films have been also doped by transition metals and nitrogen. Nitrogen has proven to be the best dopant to increase the photocatalytic activity.

INTRODUCTION

The extensive interest in titanium dioxide has taken place due to its high photocatalytic activity, nontoxicity and physicochemical stability. Photocatalytic titanium dioxide thin films are important in processes where the degradation of organic molecules is required. Titanium dioxide is also a photosemiconductor and has been widely studied in solar cell and hydrogen production.

Atomic Layer Deposition (ALD)[1] is a surface controlled layer-by-layer process for the deposition of thin films with atomic layer accuracy. Each atomic layer formed in the sequential process is a result of saturated surface controlled chemical reactions. Commonly, in the growth of binary compounds such as metal oxides, a reaction cycle consists of two reaction steps. In one step the metal compound precursor is allowed to react with the surface, and in the other step it reacts with the oxygen precursor. Between the steps a purge is applied to remove the excess of precursor and the reaction by-products. The self-controlled growth mode of atomic layer deposition contributes several advantages. The thickness of the films can be controlled in a straightforward manner by controlling the number of reaction cycles, therefore enabling the controlled growth of ultra thin layers. The precursors form stoichiometric films with large area uniformity and conformality even on complex surfaces with deformities. Layer-by-layer growth allows one to change the material abruptly after each step. This gives the possibility of depositing multicomponent films (so called nanolaminates or mixed oxides, for example).

The photocatalytic activity of titanium dioxide may be modified by changing its physicochemical properties such as crystallinity, crystal structure, particle size, and surface area. Deposition of thinner, nanoscale films and perhaps films possessing smaller crystal sizes may also result in enhanced photoredox potential for photogeneration of electrons and holes. According to quantum theories the excitation energy of small semiconductor crystals is higher from that of a larger sized semiconductor[2]. This is based on the phenomenon that for semiconductor nanoparticles the conduction and valence bands may be shifted towards more negative and more positive potentials, respectively, accordingly increasing the band gap.

Although there are numerous studies performed on titanium dioxide films, a comprehensive study of the effect of film thickness on photoinduced oxidation and catalytic activity has not been made. Tada and Tanaka[3] conclude in their study that the rate of photoinduced oxidation increases with increasing thickness. Studies claim that the best photocatalytic properties occur at thicknesses of several hundreds of nanometers[4]. Generally the studies have concentrated on the films having thicknesses larger than 100nm. In this study we have deposited a series of thicknesses of titanium dioxide in order to investigate the photocatalytic properties of thinner films. The range of thicknesses has been between 2.6nm and 260 nm. The bandgaps have been calculated for all the films. The photoactivity and photocatalytic activity have been measured by contact angle and methylene blue degradation tests, respectively.

One widely used method for enhancing the photocatalytical properties of titanium dioxide has been to dope it with impurities. Transition metals and other materials like sulfur, carbon, calcium, phosphorus, nitrogen, fluorine, and samarium ion have been utilized in doping[5-21]. The anatase form of TiO_2 has been discovered to have the highest photoreactivity. The bandgap of bulk anatase is E_g= 3.2eV which corresponds to a wavelength of 388eV whereas the bandgap of rutile is lower, about E_g=3 eV (equivalent to 414nm). The goal has been to lower the bandgap of the anatase to the visible area. We have used transition metal oxides and nitrogen for doping. Doping of the films and incorporation of other oxides as nanolaminates have been tested in order to increase the photoactivity or increase the wavelength of photoactivation. The effect of the nanolaminate sequence and layer thickness on the photoactivity and photocatalytic activity has been scrutinized.

© **2007 Society of Vacuum Coaters** 505/856-7188

50th Annual Technical Conference Proceedings (2007) ISSN 0737-5921

EXPERIMENTAL

Materials and Deposition

The precursors for plain titanium dioxide deposition were titanium tetrachloride (99.0% Fluka) and ion exchanged water. For doped titanium dioxide films iron(III) chloride (99.99% Aldrich), indium(III) chloride (99.999% Aldrich), gallium(III) chloride (99.9% Aldrich), and ammonia in water (> 25% Aldrich) were used as precursors.

The titanium dioxide films were deposited in a TFS-500 ALD reactor (Beneq Oy, Vantaa, Finland). The doped titanium dioxide films were deposited in a flow-type F-120 ALD reactor (ASM Microchemistry Oy, Helsinki, Finland). Soda-lime glass plates of 5 cm x 5 cm and ø2mm glass balls were used as substrate materials. Nitrogen (99.999%, AGA) was used as a carrier and purging gas. The reactors were operated at 5-10 mbar pressure. The precursors were kept at 20°C during the deposition and the deposition temperature was 350°C.

Characterization of the structural and photoactive properties of the film

The film thicknesses above 50nm were measured by the optical thin-film measurement system F-20 (Filmetrics, Inc.). Thicknesses lower than 50nm were calculated by linear growth estimation. The crystallinity of the films was examined by microRaman spectrometer HR800 UV (Horiba Jobin Yvon) and with the x-ray diffractometer (XRD) using CuKα radiation (Phillips X'Pert).

The water contact angles were measured with a contact angle measuring system DSA 10 (Krüss GmbH). An 8W UV lamp with a wavelength of 254 nm was used as a radiation source.

Tapping mode atomic force microscopy (AFM) (CP-II Scanning Probe Microscope, Veeco Instruments) was used for morphology images and surface area determination. Absorption spectra of the films were measured with UV-VIS spectrophotometer evolution 500 (Thermo Electron Corporation). The bandgaps of the films were estimated using the Tauc theory for indirect bandgaps.

Photocatalytic degradation measurements were conducted with methylene blue (MB) tests. Titanium dioxide films on a glass plate (5cmx5cm) or on glass balls (600) of ø2mm were first photoactivated by UV irradiation for 45 min. The distance of the sample from the lamp was 10cm. Titanium dioxide films were then placed in a 1 L beaker with 100 ml of methylene blue with concentration of 1.0×10^{-5} mol/l, close to the surface (2-3mm). The test system was kept under the UV lamp for 4 or 6 hours in ambient temperature. The distance from the UV lamp to the titanium dioxide films was 15 cm. Absorption spectra of the MB solution samples was measured with a UV-VIS spectrophotometer.

RESULTS AND DISCUSSION

Film deposition

The plain titanium dioxide films were grown from titanium tetrachloride and water. From the thickness measurements the growth rate was estimated to be 0.55 Å/cycle. Eight films of various thicknesses were grown: 2.6nm, 5nm, 10nm, 15nm, 30nm, 65nm, 130nm, and 260nm.

The nanolaminates were created by depositing the precursors in sequences. TiO_2/WO_3 was created in two different sequences: 9 x (200 x TiO_2 + 20 x WO_3) and 17 x (100 x TiO_2 + 10 x WO_3). All the other nanolaminates were deposited with 17 x (100 x TiO_2 + 10 x MeO_3) sequence. The growth rate for TiO_2/WO_3 was approximately 0.28 Å/cycle. The growth rate for TiO_2/In_2O_3, TiO_2/Fe_2O_3, and TiO_2/Ga_2O_3 was estimated to 0.51 Å/cycle. The nitrogen doped titanium dioxide films were created by using titanium tetrachloride as a titanium source and ammonium hydroxide as an oxygen and nitrogen source.

Structure and morphology of the film

The microRaman spectrum in Figure 1 shows that the film structure for the thicknesses of 10nm-260nm is a mixture of anatase and rutile. It may be possible that the crystalline structure of the films of 2.6 and 5nm are not detected by Raman spectrometry due to nanocrystallinity. A microRaman spectrum was also taken on the doped titanium dioxide. The spectra showed that the crystal structure is anatase. This was also shown by the x-ray diffraction measurements.

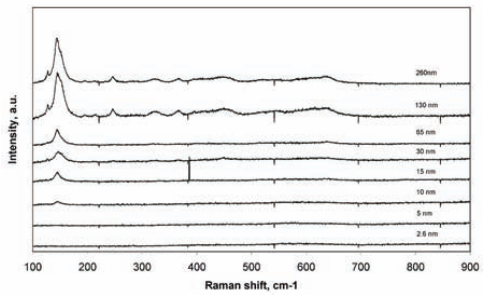

Figure 1: MicroRaman spectra for titanium dioxide films with various thicknesses.

Tapping-mode atomic force microscopy images were taken in order to study the morphology and surface area. The images were processed by WS&M[22] 4.0 software. Figure 2 shows the images of 5nm, 15nm, 65nm, and 260nm thick titanium dioxide films. It appears that the particle size starts to increase significantly after reaching the film thickness of 30nm. The image with 15nm shows some interesting formation of particle growth on top of previous particle layer. The AFM image of 2.6nm film is not shown in this paper but the image showed that the substrate surface was fully covered by titanium dioxide and the particle size distribution was wider

than in the 5nm film. The surface areas based on the AFM topography images are presented in Figure 4. The films with thicknesses of 2.6, 5, and 10nm seem to possess the same surface area. From 15nm up the surface area increases some amount but generally there is no trend or bigger changes in accordance to film thickness.

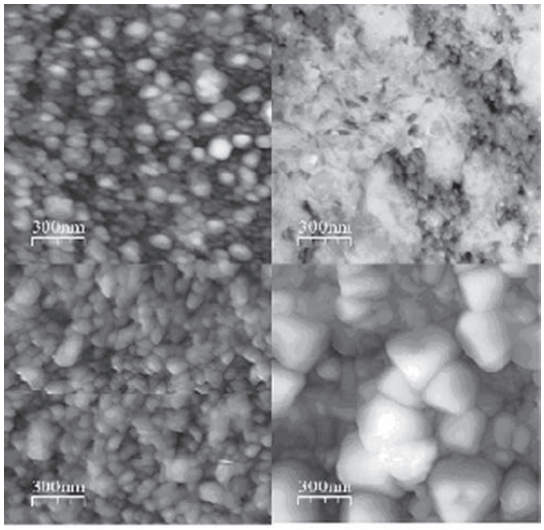

Figure 2: AFM tapping mode images of 5, 15nm (first row left to right) and 65, 260nm (second row left to right) thick titanium dioxide films.

Photoactivity and photocatalytic properties

Film Thickness

Water contact angle measurements were performed in order to study the photoactivity of the films. Titanium dioxide coated glass plates were irradiated with UV light. The results for the plain titanium dioxide films are presented in Figure 3. According to Figure 3 the photoactivity is smallest at the film thickness of 2.6nm and surprisingly biggest at the thickness of 15nm. The thicknesses of 5, 10, 65, and 130nm perform similarly but again unexpected is that the film thickness of 260nm performs worse than any of the 5 thinner films.

Next the photocatalytic activity of the films that were deposited onto glass balls has been tested by methylene blue (MB) degradation test. The test was run for 4 hours. The results of the MB degradation test are presented in Figure 4. Figure 4 shows the decrease of methylene blue concentration for several film thicknesses of titanium dioxide. The degradation test was also performed for the titanium dioxide plates that were not deposited at the same time with films on the balls. The results are shown in Figure 5 and it shows the first-order reaction kinetics for methylene blue degradation by photoactivated titanium dioxide film. Figure 5 presents also a result from a

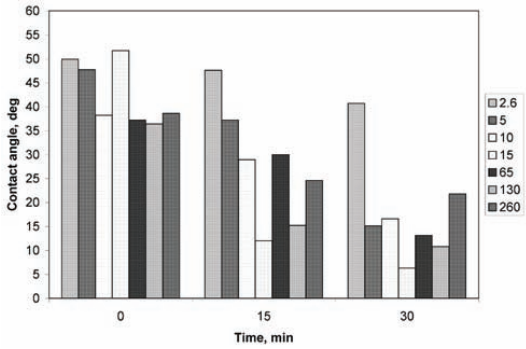

Figure 3: Water contact angles of titanium dioxide films with various thicknesses as a function of UV irradiation time.

test with nitrogen doped titanium dioxide film. This result is discussed later in the paper. From both Figures 4 and 5 we can see that the film with the thickness of 15nm is shows the highest photocatalytic activity which is in agreement with the contact angle results. The photocatalytic activity increases with the film thickness up to the point of 15nm and at 30nm it starts to decrease. The peak performance at 15nm thickness cannot be explained with the results of crystallinity and surface area which have been discussed earlier in this paper (Figures 1, 4). There is not enough information on the crystal size and crystallinity that could explain why this particular thickness area would be the most photoactive. Also according to Figure 4 the surface area does not show any peak at 15nm thickness which would explain the high photocatalytic activity. The reason may be in the AFM topography resolution so that the microscopy has not detected the smaller material particles resulting in false surface area values. The surface area vs. thicknesses (Figure 4) for all the films do not indicate why a certain thickness would be photocatalytically most active. Therefore further studies on the films have to be performed with careful scrutiny on the film structure has to be performed.

Doped Titanium Dioxide Films

Water contact angle measurements were conducted on the 100nm thick undoped titanium dioxide film, TiO_2/WO_3 (d=60nm), TiO_2/In_2O_3 (d=100nm), TiO_2/Fe_2O_3 (d=100nm), TiO_2/Ga_2O_3 (d=100nm) and $TiO_{2-x}N_x$ (d=100nm) films. Titanium dioxide coated doped glass plates were irradiated with UV light. The results are presented in Figure 6. Nitrogen doped titanium dioxide film shows the highest photoactivity. The other dopants have reduced the photoactivity of titanium dioxide. This can also be seen in Table 1 where the bandgaps of titanium dioxide doped with other elements have increased from the bulk anatase value of 3.2 eV. The nitrogen doped film has a clearly decreased bandgap of 2.8-2.9eV. These values correspond to visible light of wavelength λ=428-433nm.

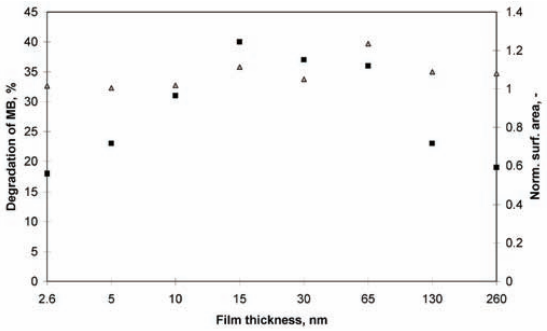

Figure 4: (i) Variation of degradation of methylene blue (MB) after 4hrs test (■) and (ii) normalized surface area with various thicknesses titanium dioxide films (▲).

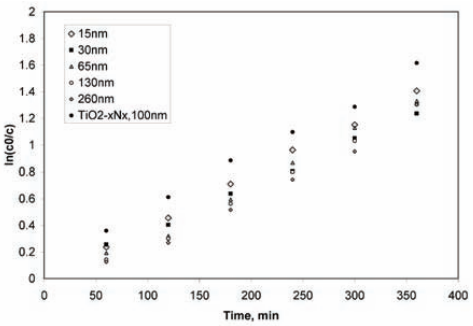

Figure 5: Methylene blue degradation with various plain titanium dioxide films and one nitrogen-doped film as a function of irradiation time.

Next the photocatalytic activity of the films that were deposited onto glass plates has been tested by the methylene blue (MB) degradation test. The tests have been run for 6 hours. As was expected based on Figure 6 the dopants which had decreased the photoactivity of the titanium film have performed inadequately in the methylene blue degradation test. Only the nitrogen doped titanium dioxide film has performed well. As seen in the Figure 6 the doping with nitrogen has been successful and Figure 5 shows that the photocatalytic activity has exceeded the activity of the best performing titanium dioxide film.

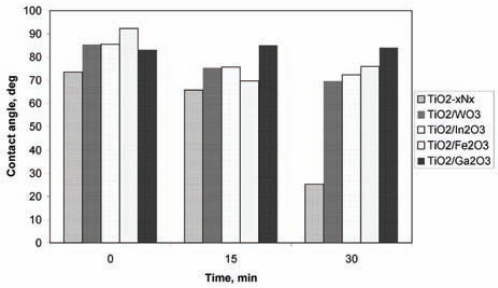

Figure 6: Water contact angles of doped titanium dioxide films as a function of UV irradiation time. All film thicknesses are 100nm, except TiO_2/WO_3 which is 60nm thick.

Table 1: Bandgaps and film thicknesses for plain titanium dioxide films and doped titanium dioxide films. A=TiO_2/WO_3, B=TiO_2/In_2O_3, C=TiO_2/Fe_2O_3, D=TiO_2/Ga_2O_3, E=$TiO_{2-x}N_x$, F=$TiO_{2-x}N_x$.

Undoped TiO_2							
d, nm	2.6	5	10	15	65	130	260
E_g, eV	3.7	3.7	3.7	3.65	3.4	3.3	3.2
Doped TiO_2	A	B	C	D	E	F	
d, nm	60	100	100	100	100	160	
E_g, eV	3.3	3.35	3.2	3.3	2.9	2.8	

CONCLUSIONS

In this study we have found enhanced photoactivity and photocatalytic activity within the nanoscale thickness of titanium dioxide films. This result has been explained by quantum effects. Film thickness of 15nm seems to possess the best photoactivity. The peak performance at certain nanoscale thickness cannot be explained yet and needs further scrutiny. Additionally we have doped titanium dioxide films and nitrogen doped titanium dioxide film has shown to be carrying the highest photocatalytic activity.

ACKNOWLEDGEMENTS

We want to thank our co-operators in Nanoscale Oy, Lahti, Finland. We also thank Miktech Oy and Mikkeli University Consortium, Mikkeli, Finland for funding this project.

REFERENCES

1. M. Ritala, M. Leskelä, in: H.S. Nalwa (Ed.), *Handbook of Thin Film Materials*, Vol.1, Academic Press, New York, 2002, pp. 103-159

2. C. Murphy and J. Coffer, "Quantum Dots: A Primer," *Applied Spectroscopy*, Vol. 56, No. 1, 2002, pp. 16A-27A

3. H. Tada and M. Tanaka, "Dependence of TiO_2 Photocatalytic Activity upon Its Film Thickness," *Langmuir*, Vol. 13, No. 2, 1997, pp.360-364

4. M. Tazawa, Okada, M, Yoshimura, K., Ikezawa, I., "Photocatalytic heat mirror with a thick titanium dioxide layer," *Solar Energy Materials & Solar Cells*, 84, (2004), pp. 159-170

5. H.-S. Lee, Hur, T., Kim, S., Kim, J.-H., Lee, H.-I., "Photocatalytic, antifogging mirror," *Catalysis Today*, 84, (2003), pp.173-180

6. S. Klosek, Raftery, D., "Visible Light Driven V-Doped TiO_2 Photocatalyst and Its Photooxidation of Ethanol," *J. Phy. Chem.* B, **2001**, 105, pp. 2815-2819

7. H. Shinguu, Bhuiyan, M., Ikegami, T, Ebihara, K, "Preparation of TiO_2/WO_3 multilayer thin film by PLD method and its catalytic response to visible light," *Thin Solid Films*, from the web

8. B. Wen, Liu, C., Liu, Y., "Bamboo-Shaped Ag-Doped TiO_2 Nanowires with Heterojunctions," *Inorg. Chem.*, **2005**, 44, pp. 6503-6505

9. B. Sankapal, Sartale, S., Lux-Steiner, M., Ennaoui, A., "Chemical and electrochemical synthesis of nanosized TiO_2 anatase for large-area photon conversion," *C.R.Chimie* 9, (2006), pp.702-707

10. J. Park, Kim, S., Bard, A., "Novel Carbon-Doped TiO_2 Nanotube Arrays with High Aspect Ratios for Efficient Solar Water Splitting," *Nano Letters*, Vol. 6, No. 1, (2006), pp. 24-28

11. R. Viitala, Langlet, M., Simola, J., Lindén, Rosenholm, "Aerosol-gel deposition of doped titania thin films," *J. Thin Solid Films*, 368, (2000), pp. 35-40

12. K. Rogers, Lane, D., Painter, J., Chapman, A., "Structural characterization of sprayed TiO_2 films for extremely thin absorber layer solar cells," *Thin Solid Films*, 466, (2004), pp. 97-102

13. H. Pathan, Min, S.-K., Desai, J., Jung, K.-D., Joo, O.-S., "Preparation and characterization of titanium dioxide thin films by SILAR method," *Materials Chemistry and Physics*, 97, (2006), pp.5-9

14. T. Morikawa, Asahi, R., Ohkawi, T., Aoki, K., Suzuki, K., Taga, Y., "Visible-light Photocatalyst – Nitrogen-doped Titanium Dioxide", *R&D Review of Toyota CRDL*, Vol. 40, No.3, (2005), pp.45-50

15. J. Premkumar, "Development of Super-Hydrophilicity on Nitrogen-Doped TiO_2 Thin Film Surface by Photoelectrochemical Method under Visible Light," *Chem. Mater.* **2004**, 16, pp. 3980-3981

16. A. Emeline, Furubayashi, Y., Zhang, X., Jin, M., Murakami, T., Fujishima, A., "Photoelectrochemical Behavior of Nb-Doped TiO_2 Electrodes," *J. Phys. Chem.* B **2005**, 109, pp. 24441-24444

17. V. Pore, Heikkilä, M., Ritala, M., Leskelä, M., Areva, S., "Atomic layer deposition of $TiO_{2-x}N_x$ thin films for photocatalytic applications," *Journal of Photochemistry and Photobiology* A: Chemistry 177 (2006), pp.68-75

18. M. Snyder, McCool, B., DiCarlo, J., Tripp, C., DeSisto, W., "An infrared study of the surface chemistry of titanium nitride atomic layer deposition on silica from $TiCl_4$ and NH_3," *Thin Solid Films*, 514, (2006), pp.97-102

19. S. Lange, Sildos, I., Kiisk, V., Aarik, J., "Energy transfer in the photoexcitation of Sm^{3+}-implanted TiO_2 thin films," *Materials Science & Engineering* B, 112, (2004), pp. 87-90

20. J. Sene, Zeltner, W., Anderson, M., "Fundamental Photoelectrocatalytic and Electrophoretic Mobility Studies of TiO_2 and V-Doped TiO_2 Thin-Film Electrode Materials," *J. Phys. Chem.* **2003**, 107, pp. 1597-1603

21. S. Sakthivel, Janczarek, M., Kisch, H., "Visible Light Activity and Photoelectrochemical Properties of Nitrogen-Doped TiO_2," *J. Phys. Chem.* B, **2004**, 108, pp. 19384-19387

22. I. Horcas et al, "WSXM 4.0," *Rev. Sci. Instrum.*, 78, 013705 (2007)

23. L. Brus., "Electronic Wave Functions in Semiconductor Clusters: Experiment and Theory," *J. Phys. Chem.* **1986**, 90, pp. 2555-2560

Paper II

Titanium dioxide thin films, their structure and its effect on their photoactivity and photocatalytic properties

M.-L. Kääriäinen, T.O. Kääriäinen, D.C. Cameron, Thin Solid Films 517 (2009) 6666–6670.

Reprinted with permission from Elsevier

Thin Solid Films 517 (2009) 6666–6670

Contents lists available at ScienceDirect

Thin Solid Films

journal homepage: www.elsevier.com/locate/tsf

Titanium dioxide thin films, their structure and its effect on their photoactivity and photocatalytic properties

M.-L. Kääriäinen *, T.O. Kääriäinen, D.C. Cameron

ASTRaL, Lappeenranta University of Technology, Prikaatinkatu 3E, FI-50100 Mikkeli, Finland

ARTICLE INFO

Article history:
Received 14 January 2009
Received in revised form 28 April 2009
Accepted 4 May 2009
Available online 11 May 2009

Keywords:
Titanium dioxide
Thin films
Atomic Layer Deposition
Photoactivity
Photocatalytic activity
X-ray diffraction
Atomic force microscopy

ABSTRACT

Atomic Layer Deposition has been used to deposit titanium dioxide thin films on soda-lime glass substrates. A series of films with thicknesses from 2.6 to 260 nm has been created and the film structure has been studied with X-ray diffraction. It has been observed that at a reaction temperature of 350 °C, titanium dioxide thin films initially grow as anatase but after a certain thickness, growth continues as rutile. The photoactivity and photocatalytic activity of the films have been found to reach their maximum at a film thickness of 15 nm. At this thickness, the film structure shows a small fraction of rutile crystallites in a largely anatase matrix indicating that both crystal phases are necessary for the maximum activity.

© 2009 Elsevier B.V. All rights reserved.

1. Introduction

There is extensive interest in titanium dioxide due to its high photocatalytic activity, nontoxicity and physicochemical stability [1,2]. Photocatalytic titanium dioxide thin films are important in processes where the degradation of organic molecules is required. Photocatalysis was performed with titanium dioxide already in the 1950s [3] but it took approximately two further decades to initiate scientific studies in the environmental area [2]. Titanium dioxide is also a photosemiconductor and has been widely studied in solar cell and hydrogen production [4–6].

Atomic Layer Deposition (ALD) [7] is a surface controlled layer-by-layer process for the deposition of thin films with atomic layer accuracy. Each atomic layer formed in the sequential process is a result of saturated surface controlled chemical reactions. Commonly, in the growth of binary compounds such as metal oxides, a reaction cycle consists of two reaction steps. In one step the metal compound precursor is allowed to react with the surface, and in the other step it reacts with the oxygen precursor. Between the steps a purge is applied to remove the excess of precursor and the reaction by-products. The self-controlled growth mode of Atomic Layer Deposition contributes several advantages. The thickness of the films can be controlled in a straightforward manner by controlling the number of reaction cycles, therefore enabling the controlled growth of ultra thin layers. The precursors form stoichiometric films with large area uniformity and conformality even on complex surfaces with deformities. Layer-by-layer growth allows one to change the material abruptly after each step. This gives the possibility of depositing multicomponent films (so called nanolaminates or mixed oxides, for example).

The photocatalytic activity of titanium dioxide may be modified by changing its physicochemical properties such as crystallinity, crystal structure, particle size, and surface area [8–11]. Deposition of thinner, nanoscale films possessing smaller crystal sizes may also result in changes in photocatalytic activity due to blue shifting of the band edge [12]. The anatase form of TiO_2 has commonly been shown to have the highest photoreactivity [13]. The bandgap of bulk anatase is $E_g = 3.2$ eV which corresponds to a wavelength of 388 nm whereas the bandgap of rutile is lower, about $E_g = 3.0$ eV (equivalent to 414 nm). Both anatase and rutile are photocatalytically active but the activity of anatase is higher and is clearly related to its ability to adsorb water and hydroxyl groups [14]. Nevertheless several studies of titanium dioxide particles have shown that there is a synergistic effect on the photocatalytic properties between anatase and rutile and that both phases are needed in order to generate an effective photocatalyst [15–18].

Although there have been numerous studies performed on titanium dioxide films, a comprehensive study of the film structure and its effect on photoinduced oxidation and catalytic activity has not been carried out, especially with low film thicknesses. Tada et al. studied the back face illumination of the TiO_2 film (using quartz as a substrate) and showed that the rate of photoinduced oxidation increased with increasing thickness up to about 100 nm [19]. They concluded that the result was accounted for only by the increasing amount of the light that was

* Corresponding author. Tel.: +358 40 536 2585.
E-mail address: marja-leena.kaariainen@lut.fi (M.-L. Kääriäinen).

0040-6090/$ – see front matter © 2009 Elsevier B.V. All rights reserved.
doi:10.1016/j.tsf.2009.05.001

absorbed by TiO_2. Based on the diffusion model they calculated the distribution of the photocarrier concentration within the film. They concluded that the photocatalytic activity is dependent on several parameters such as crystallinity, defect density of the titanium dioxide, film thickness, and the surface area. Other studies claim that the best photocatalytic properties occur at certain thicknesses, usually at several hundreds of nanometers [20,21]. Generally the studies have concentrated on the films having thicknesses larger than 100 nm. Kääriäinen et al. [22] deposited by ALD a series of titanium dioxide films with different thicknesses and concluded that the best photocatalytic property was found at a certain low film thickness. However, there have been no really systematic studies which have clarified the separate effects of thickness and crystal structure. In this study we have investigated the titanium dioxide films further in order to determine the relationship between the thickness, crystalline structure and both photoactive and photocatalytic properties of thinner films. The range of thicknesses has been between 2.6 nm and 260 nm. The photoactivity and photocatalytic activity have been measured by the water contact angle and methylene blue degradation tests, respectively.

2. Experimental section

The precursors for titanium dioxide deposition were titanium tetrachloride (99.0% Fluka) and ion exchanged water. The titanium dioxide films were deposited in a TFS 500 ALD reactor (Beneq Oy, Vantaa, Finland). Soda-lime glass plates of 5 cm × 5 cm were used as substrate materials. Nitrogen (99.999%, AGA) was used as a carrier and purging gas. The reactor was operated at 5×10^2–1×10^3 Pa pressure. The titanium dioxide films were grown at a reactor temperature of 350 °C. The precursors were kept at 20 °C during the deposition.

The film thicknesses were measured with a spectroscopic ellipsometer M-2000FI from J.A.Woollam Co., Inc. The structure and crystalline phases of the films were examined by X-ray diffractometer (XRD) (Phillips X'Pert) using CuKα radiation (λ = 1.54 Å). The XRD patterns were acquired with a glancing angle of 0.2° for the incident beam for a range 2Θ = 20–60° with a step size of 0.02°.

Morphology and surface area determination were conducted by tapping-mode atomic force microscopy (AFM) (CP-II Scanning Probe Microscope, Veeco Instruments). Absorption spectra of the films were measured with UV–VIS spectrophotometer Evolution 500 (Thermo Electron Corporation).

Water contact angles were measured with a contact angle measuring system DSA 10 (Krüss GmbH). An 8 W UV lamp with a wavelength of 254 nm was used as a UV radiation source.

Photocatalytic degradation measurements were conducted with methylene blue (MB) tests which were carried out as follows. Titanium dioxide films on a glass plate (5 cm × 5 cm) were first photoactivated in air by UV irradiation for 45 min. The distance of the sample from the lamp was 10 cm. After preactivation, titanium dioxide films were placed in a 1 L beaker with 100 mL of an aqueous solution of methylene blue with concentration of 1×10^{-5} mol/L, 2–3 mm from the liquid surface. The test system was kept under the UV lamp for 4 h in ambient temperature. The distance from the UV lamp to the titanium dioxide films was 15 cm. The absorption spectra of the MB solution samples were measured with the UV–VIS spectrophotometer. The adsorbance of methylene blue on to titanium dioxide films was tested with the same method as described above but without photoactivation as described in Section 3.

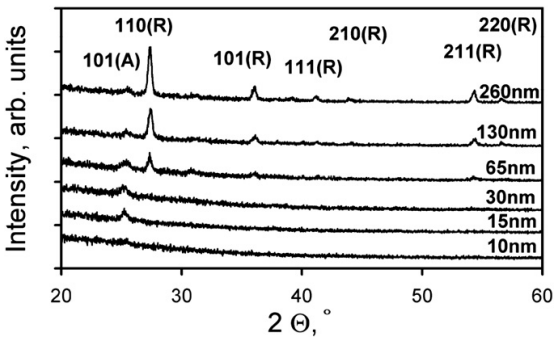

Fig. 1. X-ray diffraction spectra for titanium dioxide films with various thicknesses.

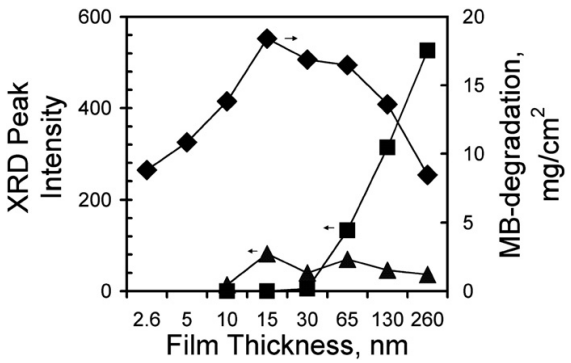

Fig. 2. X-ray diffraction intensity counts of anatase (▲) and rutile (■) peaks in the titanium dioxide films of different thicknesses and methylene blue degradation in 4 h test using the same films (◆).

3. Results

From the thickness measurements the growth rate was calculated to be 0.55 Å/cycle. Films of various thicknesses were grown, namely 2.6 nm, 5 nm, 10 nm, 15 nm, 30 nm, 65 nm, 130 nm, and 260 nm. XRD analyses for the films are shown in Fig. 1. No peaks are visible for films of thickness 2.6 nm and 5 nm due to the small size of the crystals and the very low intensity of the diffracted X-rays. Aarik et al. [23] observed using reflection high-energy electron diffraction that titanium dioxide films grown by ALD at 300 °C already showed polycrystalline anatase structure at a film thickness of 2 nm. Therefore we may assume that even the films with a few nanometer thicknesses possess some crystallinity. At a film thickness of 10 nm a tiny anatase (101) peak becomes visible (at 2Θ = 25.3°). At 15 nm the anatase (101) peak is clear and bigger. The anatase (101) peak does not grow any bigger for the 30 nm and 65 nm films and decreases for the 130 nm and 260 nm films. At 65 nm a clear rutile (110) peak has appeared (at 2Θ = 27.4°) and it increases for 130 nm and 260 nm films. Based on these results it appears that at 350 °C the titanium dioxide film begins the growth as anatase only. Between the thicknesses of 30 nm and 65 nm a phase transformation from anatase to rutile takes place. The intensity of the rutile peak increases with increasing film thickness while the anatase peak decreases after the rutile phase begins to grow. Fig. 2 shows the trends. This behavior can be explained as follows. Initially, the diffraction intensity from the anatase peak will increase due to the increasing film thickness. As growth continues and the rutile phase forms on top of the anatase, the peak from the underlying anatase region will appear to decrease because of its increasing attenuation by the upper rutile layers whereas the rutile diffraction peaks will grow due to the increasing thickness of rutile. Similarly Aarik et al. [24] observed that the rutile content increases at the film surface as the film thickness increases when depositing titanium dioxide from titanium tetrachloride and water onto silicon (111) substrates. However they added that the process is complicated since the critical thickness for the rutile growth

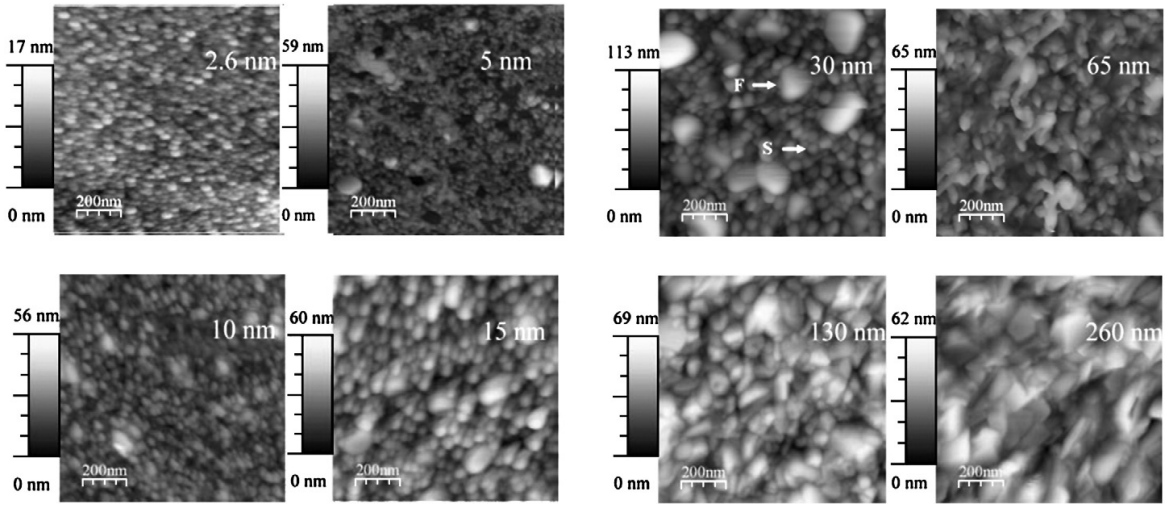

Fig. 3. AFM tapping mode images of titanium dioxide films of various thicknesses. F and S indicate typical facetted and spherical grains, respectively.

also depended on the purge times and precursor doses [24] and not only on the reactor temperature and/or substrate effect.

Tapping-mode atomic force microscopy images were taken in order to study the morphology and surface area. Fig. 3 shows the AFM images of 2.6 nm, 5 nm, 10 nm, 15 nm, 65 nm, 130 nm, and 260 nm thick titanium dioxide films. It can be seen that there is a change of morphology as the film thickness increases. The crystallites change from an initial spherical appearance to larger and more facetted. Surface area calculations based on the AFM topography images are presented in Table 1 and show no major variation with film thickness. The grain size calculations based on Scherrer's equation are shown in Table 2. We can see that the grain size for the spherical phase varies between 9 nm and 14 nm and generally does not grow much when the film thickness increases. Similarly, the size of the facetted grains does not increase much in the film thicknesses between 65 nm and 260 nm but stays within the range 46–51 nm.

Water contact angle measurements were carried out to measure the photoactivity of the thin films. Glass plates coated with titanium dioxide thin films were irradiated with UV light and the results are presented in Fig. 4. In the water contact angle measurements high photoactivity means that the photogenerated holes attract hydroxyl groups from water and produce hydroxyl radicals ($^{\bullet}OH$). The greater the number of hydroxyl molecules on the surface, the greater is its hydrophilicity and this is shown as a small contact angle between the water droplet and the TiO_2 surface. In Fig. 4, the results show that the contact angle falls from 52° to a minimum of 6° at 15 nm film thickness and then rises again reaching >20° at 260 nm indicating maximum photoactivity at 15 nm.

The photocatalytic activity of the films was tested by the methylene blue (MB) degradation test. The test was run for 4 h. The effect of surface adsorption alone on reducing the MB concentration was tested by immersing the samples in the solution without photoactivation. Three different samples were used: 15 nm TiO_2 film, 170 nm TiO_2 film, and an uncoated soda lime glass plate. The results showed that the adsorption was not significant in reducing the methylene blue concentration. The results for the photocatalytic activity are shown in Fig. 5 (and also in Fig. 2) and they followed the first-order reaction kinetics for methylene blue degradation by photoactivated titanium dioxide film. We can see that the film with

Table 1
Normalized surface area based on the AFM topography as a function of film thickness.

Film thickness, (nm)	Normalized surface area
2.6	1.0
5	1.0
10	1.02
15	1.10
30	1.05
65	1.25
130	1.07
260	1.05

Table 2
Relation between grain size of the crystals and film thickness.

Film thickness, nm	Crystal phase	Grain size, nm
10	(101) anatase	9.2
15	(101) anatase	13.3
65	(101) anatase	9.9
65	(110) rutile	48.0
130	(101) anatase	10.3
130	(110) rutile	45.7
260	(101) anatase	13.5
260	(110) rutile	50.6

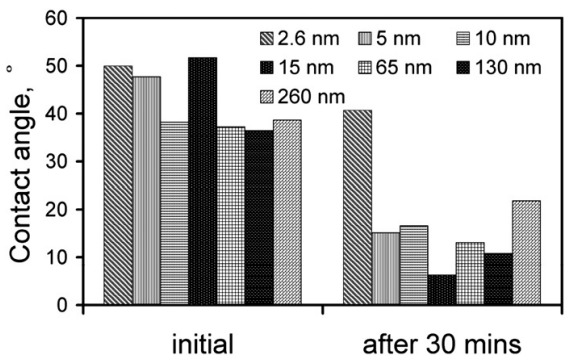

Fig. 4. Initial water contact angles of titanium dioxide thin films and their value after 30 min UV irradiation time for films of various thicknesses.

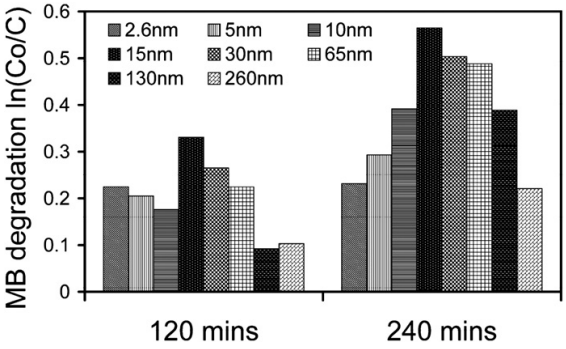

Fig. 5. Methylene blue degradation after 120 and 240 min for films of various thicknesses. C_0 and C indicate the initial MB concentration and the concentration after the degradation test, respectively.

the thickness of 15 nm shows the highest photocatalytic activity with a decrease for thicker and thinner films. This correlates with the contact angle results (Fig. 4) where the highest activity was also reached with the thickness of 15 nm. The strong connection between the photoactivity and photocatalytic activity is apparent. When the highly photoactive TiO_2 surface is in contact with a water solution the formation of the large number of hydroxyl radicals which gives high photoactivity also react with organic methylene blue molecules in solution causing them to degrade.

4. Discussion

Comparison between the XRD results and the AFM topography show that the larger, facetted grains appear when the amount of rutile in the films starts to increase. In Fig. 1, we can see that the first indication of a rutile peak appeared at a thickness between 30 and 65 nm. Previously, it has been reported [25–27] that anatase crystals have a spherical aspect whereas rutile crystals are more facetted. In Fig. 2 it is noticeable that a few larger and more elongated facetted crystals, tentatively ascribed to the rutile phase, are first observed at a thickness of 5 nm among the spherical crystals, assumed to be anatase. With only a few rutile crystals the X-ray intensity from them would be too low to be observable. With increasing film thickness these particles increasingly cover the film surface and at 260 nm there are no spherical crystallites left visible. The average particle size which is influenced by these morphology changes increases significantly after reaching the film thickness of 30 nm.

The lower photoactivity of the thicker films can be explained since they are rutile dominant and the rutile phase has been found to be less photoactive than anatase [13]. In the rutile, fast recombination of the photogenerated holes and electrons takes place and there are only a few chances for hydroxyl groups to adsorb onto rutile surface. The low photoactivity (Fig. 4) for the thinnest films (e.g. 2.6 nm) may be due to the possibility that the anatase film has not yet totally covered the substrate surface although the AFM data suggest a continuous coating. The best performing film of 15 nm shows a contact angle decrease to 6° after 30 min. XRD measurement indicated the 15 nm film to be only anatase but AFM topography showed that there is also a small amount of the rutile phase present. Several studies have postulated that the best photocatalytic activity for titanium dioxide is reached with an optimum ratio of anatase and rutile [15–18,28]. Ohno et al. [15] suggested that a certain small number of rutile particles within the dominant anatase phase or an overgrowth of rutile on the anatase crystallites will have the optimum synergistic effect on the photoactivity. Zhang et al. [29] found that titanium dioxide thin films which have a ratio of rutile to anatase between 0.5 and 0.7 produces the best photocatalytic activity. They proposed that when rutile and anatase coexist in certain proportions the rutile phase would emerge only on the surface and the anatase phase would exist inside. In our case, the peak performance range is from thicknesses of 15 to 65 nm; this can be explained with the XRD and the morphology measurements on the film which show the existence of the two phases. It has been postulated that the existence of the two crystalline phases leads to a separation of photogenerated holes and electrons which reduces their recombination rate. For example, Bickley et al. [30] suggested that electrons transfer from anatase to the lower bandgap rutile crystals which serve as electron trapping sites and thus separate the electrons and holes. In contrast, in their study of the morphology of Degussa P-25 powder which is a mixed structure (3:1 rutile:anatase) commercial photocatalytic material, Ohno et al. [15] explained that the reason for the high activity of Degussa P-25 is due to the contact between separate particles of rutile and anatase. They further explained that electron transfer would take place from rutile to anatase since in P-25 powder the rutile particles contain Ti^{3+} ions which are the electron donors. Sun and Smirniotis [16] concluded in their study on Degussa P-25 that the synergistic effect between anatase and rutile was not universal but due to the relative Fermi levels of the anatase and rutile particles and the particle shape. Hurum et al. [31] noted that Degussa P-25 consists of clustered individual crystallites where the rutile crystallites are unusually small. This topography corresponds to that of our 15 nm films where the rutile crystallites are still small and this creates an optimum synergy between anatase and rutile for optimal photocatalytic effect. When the rutile crystallites grow larger, the photogenerated carriers created in the rutile have further to travel before reaching a rutile–anatase interface and will be increasingly likely to recombine before they do. It is possible that this phenomenon takes place in our films when the photocatalytic activity decreases as the rutile crystallites grow larger covering the anatase phase. Hurum et al. [31] further explained that the rutile crystallites must be interwoven with anatase crystallites to make possible the electron transfer. A catalytic "hot spot" occurs at the anatase/rutile interface. They suggested a model where under visible illumination the electron transfer would take place from rutile to lower energy anatase lattice trapping sites allowing a more stable charge separation and consequently higher photocatalytic effect. In contrast Kawahara et al. [18] and Liu et al. [32] support the hypothesis where the electron transfer takes place from anatase to rutile which acts as an electron sink and therefore decreases the rate of the recombination of holes and electrons. In this study we cannot prove in which direction the electron transfer takes place but it is clear that the existence of both crystal phases of anatase and rutile has a fundamental effect on the photoactivity and photocatalytic ability of titanium dioxide.

Future work will explore the relationship between the photoactivity and photocatalytic ability and the deposition temperature and the substrate material.

5. Conclusions

Thin films of titanium oxide have been deposited on soda-lime glass substrates by Atomic Layer Deposition. The photoactivity and photocatalytic activity of a series of different thicknesses of titanium dioxide thin films have been measured and related to their crystal structure and morphology. The highest performance in both photoactivity, measured by the water contact angle, and photocatalytic activity, measured by the methylene blue test, was observed with films which consisted of preponderantly anatase phase and small amount of the rutile phase. We conclude that the most critical factor for obtaining a highly active titanium dioxide photocatalyst is the optimization of the anatase/rutile phase ratio. The film thickness is only significant because it has an effect on this ratio and is not important in itself.

Acknowledgments

The authors thank ESR and the State Provincial Office of Eastern Finland for supporting the project under S10148.

References

[1] A. Fujishima, K. Honda, Nature 238 (1972) 38.
[2] A. Fujishima, X. Zhang, C. R. Chim. 8 (2005) 750.
[3] K.V. Giri, G.D. Kalyankar, C.S. Vaidyanathan, Naturwissenschaften 40 (1953) 440.
[4] S.T. Martin, A.T. Lee, M.R. Hoffmann, Environ. Sci. Technol. 29 (1995) 2567.
[5] S. Günes, N.S. Sariciftci, Inorg. Chim. Acta 361 (2008) 581.
[6] P.V.V. Jayaweera, A.G.U. Perera, K. Tennakone, Inorg. Chim. Acta 361 (2008) 707.
[7] M. Ritala, M. Leskelä, in: H.S. Nalwa (Ed.), Handbook of Thin Film Materials, vol. 1, Academic Press, New York, 2002, p. 103.
[8] G. Tian, H. Fu, L. Jing, B. Xin, K. Pan, J. Phys. Chem. C 112 (2008) 3083.
[9] N. Xu, Z. Shi, Y. Fan, J. Dong, J. Shi, M.Z.-C. Hu, Ind. Eng. Chem. Res. 38 (1999) 373.
[10] S. Kelly, F.H. Pollak, M. Tomkiewicz, J. Phys. Chem. B 101 (1997) 2730.
[11] H.-J. Nam, T. Amemiya, M. Murabayashi, K. Itoh, J. Phys. Chem. B 108 (2004) 8254.
[12] C. Murphy, J. Coffer, Appl. Spectrosc. 56 (2002) 16A.
[13] K. Tanaka, M.F.V. Capule, T. Hisanaga, Chem. Phys. Lett. 187 (1991) 73.
[14] Z. Ding, G.Q. Lu, P.F. Greenfield, J. Phys. Chem. B 104 (2000) 4815.
[15] T. Ohno, K. Sarukawa, K. Tokieda, M. Matsumura, J. Catal. 203 (2001) 82.
[16] B. Sun, P.G. Smirniotis, Catal. Today 88 (2003) 49.
[17] A.G. Agrios, K.A. Gray, E. Weitz, Langmuir 19 (2003) 1402.
[18] T. Kawahara, T. Ozawa, M. Iwasaki, M. Tada, S. Ito, J. Colloid Interface Sci. 267 (2003) 377.
[19] H. Tada, M. Tanaka, Langmuir 13 (1997) 360.
[20] K. Takagi, T. Makimoto, H. Hiraiwa, T. Negishi, J. Vac. Sci. Technol. A 19 (2001) 2931.
[21] M. Tazawa, M. Okada, K. Yoshimura, I. Ikezawa, Sol. Energy Mater. Sol. Cells 84 (2004) 159.
[22] M.-L. Kääriäinen, T.O. Kääriäinen, D.C. Cameron, in: D.M. Mattox (Ed.), 50th Annual Technical Conference Proceedings, Society of Vacuum Coaters, Albuquerque, 2007, p. 335.
[23] J. Aarik, A. Aidla, T. Uustare, V. Sammelselg, J. Cryst. Growth 148 (1995) 268.
[24] J. Aarik, A. Aidla, V. Sammelselg, T. Uustare, J. Cryst. Growth 181 (1997) 259.
[25] W.E. Farneth, R.S. McLean, J.D. Bolt, E. Dokou, M.A. Barteau, Langmuir 15 (1999) 8569.
[26] J. Sheng, L. Shivalingappa, J. Karasawa, T. Fukami, J. Mater. Sci. 34 (1999) 6201.
[27] N. Savage, B. Chwieroth, A. Ginwalla, B.R. Patton, S.A. Akbar, P.K. Dutta, Sens. Actuators, B 79 (2001) 17.
[28] S. Bakardjieva, J. Šubrt, V. Štengl, M.J. Dianez, M.J. Sayagues, Appl. Catal. B 58 (2005) 193.
[29] W.-Z. Zhang, T. Zhang, T. Yin, G.-Y. Cao, Chin. J. Chem. Phys. 20 (2007) 95.
[30] R.I. Bickley, T. Gonzalez-Carreno, J.T. Lees, L. Palmisano, R.J. Tilley, J. Solid State Chem. 92 (1991) 178.
[31] D.C. Hurum, A.G. Agrios, K.A. Gray, J. Phys. Chem. B 107 (2003) 4545.
[32] Z. Liu, X. Zhang, S. Nishimoto, M. Jin, D.A. Tryk, T. Murakami, A. Fujishima, Langmuir 23 (2007) 10916.

Paper III

The importance of the majority carrier polarity and p-n junction in titanium dioxide films to their photoactivity and photocatalytic properties

M.-L. Kääriäinen, D.C. Cameron, Surface Science 606 (2012) L22–L25.

Reprinted with permission from Elsevier

Surface Science 606 (2012) L22–L25

Contents lists available at SciVerse ScienceDirect

Surface Science

journal homepage: www.elsevier.com/locate/susc

Surface Science Letters

The importance of the majority carrier polarity and p-n junction in titanium dioxide films to their photoactivity and photocatalytic properties

M.-L. Kääriäinen *, D.C. Cameron

ASTRaL, Lappeenranta University of Technology, Prikaatinkatu 3E, FI-50100 Mikkeli, Finland

ARTICLE INFO

Article history:
Received 7 September 2011
Accepted 9 November 2011
Available online 15 November 2011

Keywords:
p- and n-type titanium dioxide
Atomic layer deposition
Photoactivity
Photocatalytic activity

ABSTRACT

In this paper, undoped polycrystalline titanium dioxide films have been deposited by atomic layer deposition (ALD) using the titanium tetrachloride–water process. These films have been anatase, rutile, or mainly anatase with a varying content of rutile depending on the deposition conditions. The polarity of the majority carriers on the films has been measured with the hot-probe test and, over the range of deposition temperatures used, the anatase or anatase-dominant films have been found to be p-type whereas the rutile films have been n-type. X-ray diffraction (XRD), contact angle measurements, and methylene blue degradation tests were performed to investigate the crystallinity, photoactivity, and photocatalytic properties. All the p-type films showed good photoactivity as determined by their water contact angle while the best photocatalytic activity was shown with anatase films containing a small proportion of rutile. An explanation for the superior photoactivity of anatase due to its p-type polarity is given and the high photocatalytic property for anatase-dominant films is ascribed to the existence of p-n junctions leading to carrier separation.

© 2011 Elsevier B.V. All rights reserved.

1. Introduction

Titanium dioxide is the most studied semiconductor among the photocatalytic materials. The surface reactions and photocatalytic mechanisms have been widely investigated since the discovery of photocatalytic splitting of water [1–6]. Anatase has been accepted to be the most photoactive phase of TiO_2 due to a lower recombination rate of electrons and holes. Synergy between anatase and rutile has been claimed to enhance photocatalytic activity and there have been a number of suggestions as to its mechanism [7–16]. Due to the vast numbers of applications, the researchers in the field of TiO_2 are divided into several areas where their understanding and expertise focus on different aspects. Therefore, there are only few studies on TiO_2 where its electrical properties, structural properties, and photocatalytic characteristics have been studied and compared [17,18]. Generally TiO_2 has been found to be n-type and this behavior has been observed both in rutile and anatase structures [19,20]. Savage et al. [21] created n-type anatase and p-type rutile from titania powders and applied them in gas sensors. Li et al. [22] have reported anatase that changes its polarity depending on the energy of light irradiation. Hossein-Babaei et al. [23] have deposited undoped p-type anatase films by the sol–gel technique for gas sensing applications but have not discussed the photocatalytic aspects. However, there have been no systematic studies of the connection between the polarity of the titanium dioxide, its crystal structure, and its photoactivity and photocatalytic activity. In this letter we have measured these parameters and found the relationship between them. We have laid out the probable processes which give rise to this behavior.

2. Experimental

TiO_2 films with thickness between 10 and 260 nm were grown by atomic layer deposition (ALD) using titanium tetrachloride (99.0%, Fluka) and deionized water as precursors. Nitrogen (>99.999%) was used as a carrier and purging gas. The deposition was carried out in a TFS-500 ALD reactor (Beneq Oy) at 5×10^2–1×10^3 Pa pressure. Two different reaction temperatures of 250 °C and 350 °C were used. The precursors were introduced into the reactor in a sequence of pulse ($TiCl_4$) – rinse (N_2) – pulse (H_2O) – rinse (N_2) of 0.6–1–0.25–0.5 s. Soda-lime glass plates of 5 cm × 5 cm were used as substrate materials. The precursors were kept at 20 °C during the deposition. The film thicknesses were measured with a spectroscopic ellipsometer M-2000FI from J.A. Woollam Co., Inc. The structure and crystalline phases of the films were examined by X-ray diffractometer (XRD) (Phillips X'Pert) using CuKα radiation (λ = 1.54 Å). Water contact angles were measured with a contact angle measuring system DSA 10 (Krüss GmbH). Absorption spectra of the films were measured with UV–VIS spectrophotometer Evolution 500 (Thermo Electron Corporation). An 8 W UV lamp with a wavelength of 254 nm was used as an UV radiation source. Photocatalytic degradation measurements were conducted with methylene blue (MB) tests, the details of which were described in earlier publication [7]. The polarity

* Corresponding author. Tel.: +358 40 536 2585.
E-mail address: marja-leena.kaariainen@lut.fi (M.-L. Kääriäinen).

0039-6028/$ – see front matter © 2011 Elsevier B.V. All rights reserved.
doi:10.1016/j.susc.2011.11.009

of the majority carriers was determined using the hot probe measurement. The measurement is prepared by connecting a couple of wires to a sensitive electrometer. A heated probe, called a hot probe is connected to the positive terminal and the other, called a cold probe is connected to the negative terminal of the meter. When the probes are placed on a n-type semiconductor a positive current is obtained while placed on a p-type semiconductor a negative current occurs [24]. The polarity was measured after taking the samples from dark storage and again after 30 min of UV irradiation.

A commercial product, Pilkington Activ™, was studied for comparison in photoactivity, photocatalytic activity, and polarity. The thickness of titanium dioxide film on Pilkington Activ™ glass is approximately 15 nm [25] and its crystalline structure has been shown to be anatase [26].

3. Results and discussion

Two series of TiO_2 thin films with various thicknesses were deposited by ALD. The photoactivity and photocatalytic properties were investigated to explore the relationship between these properties and the structural and electronic properties of the films. Fig. 1 shows the X-ray spectra of the TiO_2 films deposited at 250 °C and 350 °C.

The 250 °C films grew initially as rutile but thicknesses of 25 nm and above were all anatase. The 350 °C showed initial anatase growth followed by an anatase-rutile transformation beginning around 15 nm with increasing amounts of rutile present as the thickness increased becoming rutile dominant between 90 nm and 260 nm. There are no major differences in crystal quality between the 260 °C and 350 °C series as shown by the similar peak widths.

Contact angle measurements (Fig. 2) showed that the 15 nm rutile film from 250 °C series possesses the worst photoactivity whereas the anatase and anatase dominant films were very hydrophilic after UV exposure. That is, the photoactivity depends solely on the dominant crystal phase and there is no major difference between the effectiveness of anatase or anatase dominating films deposited at 250 °C or 350 °C. The photocatalytic results show that a different situation applies.

Fig. 3 shows MB-degradation test results. The 350 °C series of anatase-dominant films showed higher photocatalytic activity than the 250 °C series and the best photocatalytic performance was reached with a 15 nm thick anatase film that had only a very small amount of rutile phase [7]. The Pilkington Activ™ anatase sample demonstrated the best performance but all the 250 °C anatase films were inferior. Semiconductor polarity was measured by the hot probe test and it was found that all the anatase and anatase-dominant films were p-type (Table 1). Also the Pilkington Activ™ anatase film was p-type. Rutile (15 nm 250 °C) and rutile dominant (260 nm 350 °C) films were both n-type. All the films maintained their polarity during the 30 min of UV irradiation.

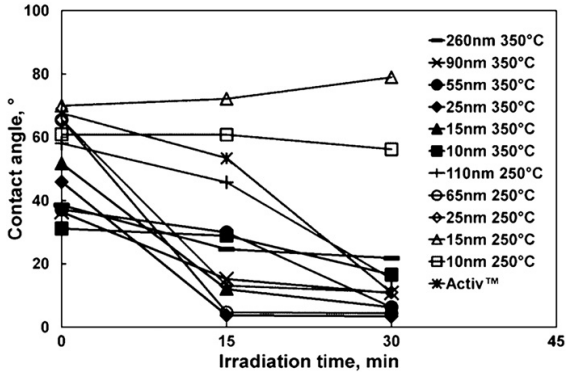

Fig. 2. Water contact angles for titanium dioxide films with various thicknesses deposited at 250 °C and 350 °C.

Based on the results it is clear that the p-type anatase performs better in photoactivity than n-type rutile. However, in photocatalytic activity p-type anatase alone is evidently not enough to produce a good performance. The results indicate that better performance is produced if there is an anatase-dominant anatase-rutile mixture. The Pilkington Activ™ p-type anatase is slightly better than the 15 nm thick 350 °C series film, however, it is possible that Activ™ also includes small amounts of rutile which are not seen in the XRD spectrum [26]. It is notable that the popularly-used Degussa P25 material is also an anatase dominant anatase-rutile mixture [8]. Since anatase was shown to be p-type and rutile n-type, this suggests that the reason for the improved performance of the mixture of anatase and rutile is the formation of p-n junctions which cause carrier separation. To understand the connection between TiO_2 polarity, photoactivity, and photocatalytic activity we discuss the photocatalytical reactions and how the structure of TiO_2 may contribute to them.

TiO_2 photoexcitation takes place when an electron (e^-) is excited by photon energy ($h\nu$) from valence band (V_b) to conduction band (C_b) and a hole (h^+) is formed into the valence band. After excitation there are several options that can occur [4]: the electron and the hole

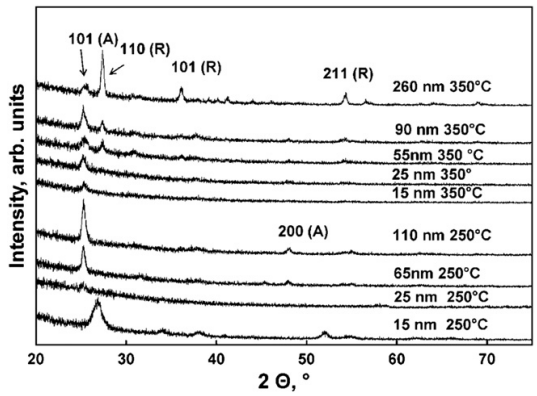

Fig. 1. X-ray diffraction spectra for titanium dioxide films with various thicknesses deposited at 250 °C and 350 °C (A = anatase, R = rutile).

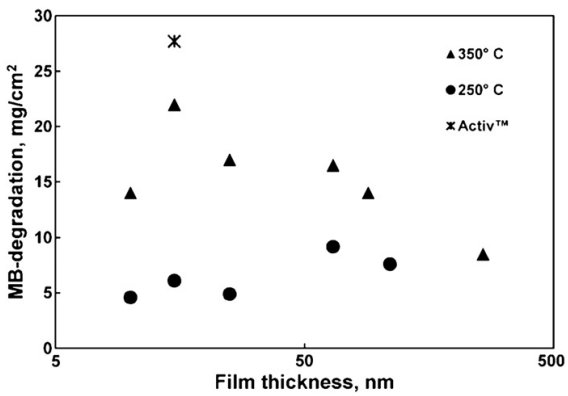

Fig. 3. Methylene blue degradation test for titanium dioxide films with various thicknesses deposited at 250 °C and 350 °C.

Table 1
Polarity of titanium dioxide films with various thicknesses deposited at 250 °C and 350 °C, and Pilkington Activ™ film.

	Polarity	
	0 min UV	30 min UV
15 nm 250 °C	N-type	N-type
25 nm 250 °C	P-type	P-type
65 nm 250 °C	P-type	P-type
110 nm 250 °C	P-type	P-type
15 nm 350 °C	P-type	P-type
25 nm 350 °C	P-type	P-type
55 nm 350 °C	P-type	P-type
90 nm 350 °C	P-type	P-type
260 nm 350 °C	N-type	N-type
Activ™	P-type	P-type

can recombine dissipating the input photon energy to heat, become trapped in metastable semiconductor surface states, or they can interact with electron donors and acceptors that are adsorbed on the TiO_2 surface. The recombination occurs in a few nanoseconds if there is a lack of scavengers that could trap the electrons or the holes. A trapped electron from the conduction band is a good reductant and a hole from the valence band is an outstanding oxidant enabling redox reactions to take place. The following basic mechanisms for the photogeneration of radicals in atmospheric and aqueous environments have been proposed when there are water and oxygen present on the TiO_2 surface [4,5,27]. 1) $TiO_2 + h\nu \rightarrow h^+ + e^-$ (generation), 2) $h^+ + H_2O_{absorbed} \leftrightarrow H^+ + {}^{\bullet}OH$ (reaction), 3) $h^+ + OH^- \leftrightarrow {}^{\bullet}OH$ (reaction), 4) $e^- + O_{2absorbed} \leftrightarrow {}^{\bullet}O_2^-$ (reaction), 5) $h^+ + Ti^{4+}OH \rightarrow (Ti^{4+}OH^{\bullet})^+$ (hole trapping), 6) $e^- + Ti^{4+}OH \leftrightarrow Ti^{3+}OH$ (electron trapping).

Investigators have discovered differences between the atomic configuration of anatase and rutile and hence their electronic properties. Anatase has been found to have an indirect bandgap whereas rutile has a direct one [28]. This could contribute to slower recombination rate of anatase, and consequently higher photoactivity and photocatalytic activity, assuming electron–hole pairs can be efficiently created. When the polarity of TiO_2 has been studied, rutile and also anatase has been generally found to be n-type [19]. Creating oxygen vacancies has been one common doping method to create an n-type semiconductor. In fact oxygen vacancies have been found to be more common on rutile than on anatase [29] and the reason for this has been suggested to lie in their significantly different atomic surface structure [30]. Studies have further proved that photoactivation reactions are different on anatase and rutile. On rutile which has oxygen vacancies, water has been discovered to dissociate to form pairs of closely bridging hydroxyl (OH) groups [31]. $Ti^{4+}(OH)$ can form $Ti^{3+}OH$ by the capture of electrons. These Ti(OH) groups have been discovered to be good electron traps for photogenerated electrons [32] forming $Ti^{3+}(OH)$ groups which further may attract holes becoming recombination centers [6]. Recombination stops the reaction chain and this may be a reason why n-type rutile has lower photoactivity compared to anatase. In contrast molecular water has been found on anatase (101) [33] which is due to the lack of oxygen vacancies. If the anatase is p-type, it will be superior in photoactivity. In a p-type semiconductor the holes are the majority carriers. Therefore p-type anatase can provide a plentiful supply of holes to the surface which attract the hydroxyl part of the water allowing water molecules to adsorb on the surface. Under UV irradiation, more holes are available at the surface and hence the larger number of adsorbed hydroxyl groups attract more water making the surface even superhydrophilic.

The results show p-type anatase to be very photoactive but in photocatalytic performance it is not much better than n-type rutile. This implies that p-type anatase would also suffer from the problem of recombination which means there are not enough excited electrons to create hydroxyl radicals for further photoactivity reactions. However, when a rutile phase begins to grow along anatase the photocatalytic performance is improved. Therefore, we propose that p-type anatase and n-type rutile form p-n junctions in the TiO_2. In a p-n junction the conduction and valence bands of anatase will have higher energies than those of rutile. When it is illuminated by UV-light, transfer of photogenerated electrons will take place from the p-type (anatase) conduction band to the n-type (rutile) conduction band, whereas the transfer of photogenerated holes will take place from the valence band of n-type (rutile) to the valence band of p-type (anatase). This results in the electron–hole separation which reduces recombination and gives a larger supply of holes to the surface to enhance the photocatalytic reactions.

4. Conclusions

The relationship between deposition temperature, the crystal structure and the majority carrier polarity in titanium dioxide deposited by atomic layer deposition has been investigated. The films are polycrystalline being either anatase, rutile, or anatase-rutile mixtures. The anatase-dominant films are always p-type whereas the rutile-dominant films are always n-type. The crystal quality shows no major difference in films deposited at 250 °C and 350 °C. All the anatase or anatase-dominant films showed good photoactivity while rutile films showed poor photoactivity. However, good photocatalytic activity was only observed in anatase films containing some rutile. It is proposed that the superior photocatalytic property of anatase-dominant mixture of phases is due to the formation of p-n junctions in the TiO_2 which causes carrier separation and hence a reduction in recombination.

Acknowledgements

The authors thank ESR and the State Provincial Office of Eastern Finland for supporting the project under S10148.

References

[1] A. Fujishima, K. Honda, Nature 238 (1972) 38.
[2] A.L. Linsebigler, G. Lu, J.T. Yates, Chem. Rev. 95 (1995) 735.
[3] R.F. Howe, M. Grätzel, J. Phys. Chem. 91 (1987) 3906.
[4] M.R. Hoffmann, S.T. Martin, W. Choi, D.W. Bahnemann, Chem. Rev. 95 (1995) 69.
[5] D.W. Bahnemann, M. Hilgendorff, R. Memming, J. Phys. Chem. B 101 (1997) 4265.
[6] C. Di Valentin, G. Pacchioni, A. Selloni, Phys. Rev. Lett. 97 (2006) 166803.
[7] M.-L. Kääriäinen, T.O. Kääriäinen, D.C. Cameron, Thin Solid Films 517 (2009) 6666.
[8] T. Ohno, K. Sarukawa, K. Tokieda, M. Matsumura, J. Catal. 203 (2001) 82.
[9] B. Sun, P.G. Smirniotis, Catal. Today 88 (2003) 49.
[10] A.G. Agrios, K.A. Gray, E. Weitz, Langmuir 19 (2003) 1402.
[11] T. Kawahara, T. Ozawa, M. Iwasaki, M. Tada, S. Ito, J. Colloid Interface Sci. 267 (2003) 377.
[12] S. Bakardjieva, J. Šubrt, V. Štengl, M.J. Dianez, M.J. Sayagues, Appl. Catal., B 58 (2005) 193.
[13] W.-Z. Zhang, T. Zhang, T. Yin, G.-Y. Gao, Chin. J. Chem. Phys. 20 (2007) 95.
[14] R.I. Bickley, T. Gonzales-Carreno, J.T. Lees, L. Palmisano, R.J. Tilley, J. Solid State Chem. 92 (1991) 178.
[15] D.C. Hurum, A.G. Agrios, K.A. Gray, J. Phys. Chem. B 107 (2003) 4545.
[16] Z. Liu, X. Zhang, S. Nishimoto, M. Jin, D.A. Tryk, T. Murakami, A. Fujishima, Langmuir 23 (2007) 10916.
[17] A. Fujishima, T.N. Rao, D.A. Tryk, J. Photochem. Photobiol. C Photochem. Rev. 1 (2000) 1.
[18] D.S. Warren, Y. Shapira, H. Kisch, A.J. McQuillan, J. Phys. Chem. C Lett. 111 (2007) 14286.
[19] M.D. Earle, Phys. Rev. 61 (1942) 56.
[20] C. Shifu, Z. Wei, L. Wei, Z. Sujuan, Appl. Surf. Sci. 255 (2008) 2478.
[21] N. Savage, B. Chwieroth, A. Ginwalla, B.R. Patton, S.A. Akbar, P.K. Dutta, Sens. Actuators B 79 (2001) 17.
[22] Q. Li, X. Wang, Z. Jin, D. Yang, S. Zhang, X. Guo, J. Yang, Z. Zhang, J. Nanopart. Res. 9 (2007) 951.
[23] F. Hossein-Babaei, M. Keshmiri, M. Kakavand, T. Troczynski, Sens. Actuators B 110 (2005) 28.
[24] B. Van Zeghbroeck, Principles of Semiconductor Devices, http://ecee.colorado.edu/~bart/book/2011.
[25] A. Mills, A. Lepre, N. Elliott, S. Bhopal, I.P. Parkin, S.A. O'Neill, J. Photochem. Photobiol. A Chem. 160 (2003) 213.
[26] P. Chin, D.F. Ollis, Catal. Today 123 (2007) 177.

SURFACE SCIENCE LETTERS

[27] J. Nelson, A.M. Eppler, I.M. Ballard, J. Photochem. Photobiol. A Chem. 148 (2002) 25.
[28] N. Serpone, D. Lawless, R. Khairutdinov, J. Phys. Chem. 99 (1995) 16646.
[29] W. Hebenstreit, N. Ruzycki, G.S. Herman, Y. Gao, U. Diebold, Phys. Rev. B 62 (2000) R16334.
[30] G.S. Herman, Z. Dohnalek, N. Ruzycki, U. Diebold, J. Phys. Chem. 107 (2003) 2788.
[31] R. Schaub, P. Thostrup, N. Lopez, E. Lægsgaard, I. Stensgaard, J.K. Nørskov, F. Besenbacher, Phys. Rev. Lett. 87 (2001) 266104.
[32] R. Nakamura, Y. Nakato, J. Am. Chem. Soc. 126 (2004) 1290.
[33] A. Vittadini, A. Selloni, F.P. Rotzinger, M. Grätzel, Phys. Rev. Lett. 81 (1998) 2954.

Paper IV

Nitrogen doping in atomic layer deposition grown titanium dioxide films by using ammonium hydroxide

M.-L. Kääriäinen, D.C. Cameron, Thin Solid Films 526 (2012) 212–217.

Reprinted with permission from Elsevier

Thin Solid Films 526 (2012) 212–217

Contents lists available at SciVerse ScienceDirect

Thin Solid Films

journal homepage: www.elsevier.com/locate/tsf

Nitrogen doping in atomic layer deposition grown titanium dioxide films by using ammonium hydroxide

M.-L. Kääriäinen *, D.C. Cameron

ASTRaL, Lappeenranta University of Technology, Sammonkatu 12, FI-50130 Mikkeli, Finland

ARTICLE INFO

Article history:
Received 31 October 2011
Received in revised form 4 November 2012
Accepted 6 November 2012
Available online 16 November 2012

Keywords:
Nitrogen doping
Titanium dioxide
Thin films
Atomic layer deposition
Photoactivity
Photocatalytic activity
Resistivity

ABSTRACT

Titanium dioxide films have been created by atomic layer deposition using titanium chloride as the metal source and a solution of ammonium hydroxide in water as oxidant. Ammonium hydroxide has been used as a source of nitrogen for doping and three thickness series have been deposited at 350 °C. A 15 nm anatase dominated film was found to possess the highest photocatalytic activity in all film series. Furthermore almost three times better photocatalytic activity was discovered in the doped series compared to undoped films. The doped films also had lower resistivity. The results from X-ray photoemission spectroscopy showed evidence for interstitial nitrogen in the titanium dioxide structure. Besides, there was a minor red shift observable in the thickest samples. In addition the film conductivity was discovered to increase with the feeding pressure of ammonium hydroxide in the oxidant precursor. This may indicate that nitrogen doping has caused the decrease in the resistivity and therefore has an impact as an enhanced photocatalytic activity. The hot probe test showed that all the anatase or anatase dominant films were p-type and all the rutile dominant films were n-type. The best photocatalytic activity was shown by anatase-dominant films containing a small amount of rutile. It may be that p–n-junctions are formed between p-type anatase and n-type rutile which cause carrier separation and slow down the recombination rate. The combination of nitrogen doping and p–n junction formation results in superior photocatalytic performance.

© 2012 Elsevier B.V. All rights reserved.

1. Introduction

Titanium dioxide and especially the anatase phase is the most effective photocatalytic material. It can be used in self cleaning surfaces, air and water purification, and dye sensitized films among others [1]. Its drawback is that it has a band gap of 3.0–3.2 eV therefore needing a wavelength of 388 nm or less for photoactivation. As a consequence only about 4% of solar energy can be utilized in TiO_2 photoactivation. It also suffers from the fast recombination of electrons and holes during the photoactivation which reduces its efficiency. In order to improve the visible light activity and to decrease the recombination problem in thin films many studies have been conducted with various dopants [2–11]. Nitrogen doping has been one of the most popular ways of attempting to modify the bandgap. Studies have shown that bandgap red shift towards visible light and lower recombination have been achieved but also opposing, negative results have been seen [12–25]. Often the enhanced photoactivity has not guaranteed improved photocatalytic properties. The different dopants affect various properties of the titanium dioxide such as crystal structure, photoactivity, electrical properties, and chemical behavior in the photocatalytical reactions.

In this work we have used atomic layer deposition (ALD) to create nitrogen doped titanium dioxide films. ALD is a surface controlled process for deposition of thin films with atomic layer accuracy. Each atomic layer formed in the sequential process is a result of saturated surface controlled chemical reactions. A very common process to deposit titanium dioxide with ALD uses titanium chloride and water as precursors. In an earlier study it was shown that the photocatalytic activity of titanium dioxide film could be enhanced by using ammonium hydroxide as an oxidizer instead of water [26]. In the present work we have investigated the doped films further by creating three separate series of nitrogen doped and undoped films with different doping levels. The structure of the titanium dioxide films, their photoactivity, photocatalytic properties, film composition, major carrier polarity, and film resistivity have been measured and discussed to clarify and explain the enhanced photocatalytic activity.

2. Experimental section

The doped and undoped titanium dioxide films were deposited in a TFS-500 ALD reactor (Beneq Oy). Soda–lime glass plates of 5 cm × 5 cm were used as substrate materials. Generated nitrogen of 99.999% purity was used as a carrier and purging gas (INMATEC IMT-PN 1150, INMATEC GaseTechnologie GmbH & Co.KG). The reaction temperature was 350 °C. The precursors for nitrogen doped titanium dioxide deposition were titanium tetrachloride (99.0%, Fluka) and two different ammonium hydroxide water solutions of 28 wt.% (A) and 19 wt.% (B) (28 wt.%, ALDRICH). The latter solution (B) was diluted from the

* Corresponding author. Tel.: +358 40 536 2585.
E-mail address: marja-leena.kaariainen@lut.fi (M.-L. Kääriäinen).

0040-6090/$ – see front matter © 2012 Elsevier B.V. All rights reserved.
http://dx.doi.org/10.1016/j.tsf.2012.11.005

28 wt.% solution with deionized water. The precursors were kept at 20 °C during the deposition. Due to the higher vapor pressure of ammonium hydroxide solution its volumetric flow rate was restricted by needle valve so that there would not be a large difference between the partial pressure of ammonium hydroxide in the doped runs and the partial pressure of water in the undoped TiO_2 runs. The feeding pressures of 28 wt.% and 19 wt.% ammonium hydroxide solutions were measured to be 1150 Pa and 880 Pa, respectively. In the undoped runs the feeding pressure of water was 800 Pa. In order to find out the amount of dissolved ammonium hydroxide and the amount of water in the precursor feeding line the partial pressures were calculated by using Raoult's law. In the system using the 28 wt.% solution the partial pressures for ammonium hydroxide and water were 1070 Pa and 79 Pa, respectively. When using the 19 wt.% solution the partial pressure for ammonium hydroxide was 785 Pa and for water was 95 Pa. The reactor was operated approximately at 250 Pa. Consequently it was presumed that only ammonium hydroxide was fed to the precursor line and water remained in the precursor bottle since its partial pressures were lower than the reactor pressure. In all runs a sequence of pulse–rinse–pulse–rinse of 0.6–1–0.25–0.5 s was used for $TiCl_4$, N_2, ammonium hydroxide or H_2O and N_2 gases.

The film thicknesses were measured with a spectroscopic ellipsometer M-2000FI from J.A. Woollam Co., Inc. The structure and crystalline phases of the films were examined by X-ray diffractometer (XRD) (Phillips X'Pert) using CuKα radiation (λ = 1.54 Å). The XRD patterns were acquired with a glancing angle of 0.2° for the incident beam for a range 2Θ = 20–60° with a step size of 0.02°. Morphology was studied with a Hitachi S4800 field emission scanning electron microscope (SEM) with an operating voltage of 5 kV. Transmission spectra of the films were measured with UV–vis spectrophotometer Evolution 500 (Thermo Electron Corporation) and band gaps were evaluated by Swanepoel method [27]. Film composition was examined by X-ray photoelectron spectroscopy (XPS) (PHI 5400) with MgKα radiation (energy of 1253.6 eV) in a pressure of $1 \cdot 10^{-9}$ Torr. Sputtering was performed using Ar^+ ions with beam energy of 3 keV and a current of 2 μA. The beam was rastered over 3×3 mm^2 hence the beam current density was 0.22 $\mu A/mm^2$. Binding energy was referenced in all samples to carbon 1s line assuming energy of 284.8 eV. Resulting XPS peaks were fitted by using XPSPEAK4.1 software applying a Shirley type background and Gaussian peaks.

Water contact angles were measured with a contact angle measuring system DSA 10 (Krüss GmbH). An 8 W UV lamp with a wavelength of 254 nm was used as a UV radiation source. Photocatalytic degradation measurements were conducted with methylene blue (MB) tests, the details of which were described earlier [28]. The hot probe tests were performed for major carrier polarity. The film resistivity measurements were done by four-point-probe measurements.

A commercial product, Pilkington Activ™, was studied for comparison in photoactivity, photocatalytic activity, and film resistivity. The thickness of titanium dioxide film on Pilkington Activ™ glass is approximately 15 nm [29] and Chin et al. [30] reported its crystalline structure to be anatase.

3. Results and discussion

The deposition rate was 0.55 Å/cycle for both A (28 wt.% NH_4OH) and B (19 wt.% NH_4OH) films. This rate is the same as in the titanium dioxide films deposited with water as a precursor. Three series of films with thickness 2.6 nm, 5 nm, 10 nm, 15 nm, 30 nm, 65 nm, 130 nm, and 260 nm were deposited for undoped, doped A, and doped B films. XRD analyses for the films are shown in Fig. 1. The thinnest films of 2.6 nm, 5 nm, and 10 nm are not shown in the XRD results because the patterns were very weak but according to SEM images crystalline grains are shown with these films (not presented). The XRD patterns show that all series are similarly polycrystalline and an anatase to rutile transformation takes place at approximately the same thickness in all

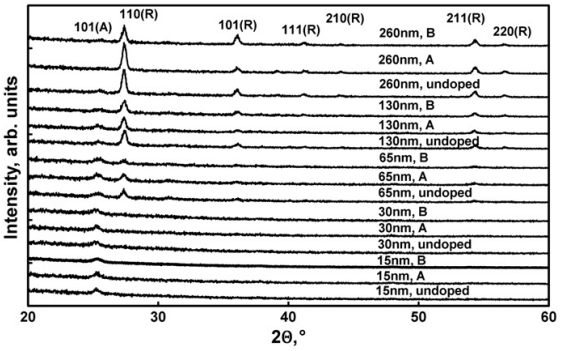

Fig. 1. X-ray diffraction patterns for doped A-, doped B-, and undoped titanium dioxide films with various thicknesses.

films. The film structure is first anatase but somewhere after thickness of 30 nm also rutile starts to show and finally becomes the dominant crystal structure for 130 nm and 260 nm films.

The grain size was calculated using Scherrer's equation. Table 1 shows the grain sizes for the undoped TiO_2 films and the films of doped A and B series. There are no major differences between the grain growth in the different film series. In all films anatase grain sizes are between 9 and 15 nm and rutile grain sizes are between 39 and 51 nm.

A scanning electron microscopy (SEM) image of the 15 nm thick film of series A is shown in Fig. 2. Most of the grains are protruding upwards and are spherical in shape (S). There are also areas where the grains are more facetted (F) and lying down. In our earlier study [28] it was speculated that the spherical grains are anatase and the more facetted grains are rutile since they become more evident as the rutile XRD diffraction peak grows and eventually dominate. The 15 nm thick films in all series (doped A, doped B, and undoped) looked similar (B and undoped not shown). The grain size for 15 nm thick films was 12–13 nm from Scherrer's formula and the SEM images show similar results for the spherical grains.

The band gaps were evaluated based on the transmittance spectra by plotting $(\alpha \upsilon h)^{1/2}$ as a function of band gap energy, E [27] and the values are presented in Table 2. The 260 nm films show a change in band gap from the undoped value of 3.2 eV to 3.1 eV for the doped samples which may be an indication of nitrogen doping.

In order to evaluate the nitrogen doping, an X-ray photoelectron spectroscopy analysis was performed on doped and undoped samples. Titanium dioxide films with thickness of 260 nm were analyzed

Table 1
Relation between grain size of the crystals and film thickness in doped A-, doped B-, and undoped series.

Film thickness, nm	Crystal phase	Grain size, nm		
		A	B	Undoped
10	(101) Ana	–	–	9
15	(101) Ana	13	12	13
30	(101) Ana	15	12	14
65	(101) Ana	12	10	10
65	(110) Rut	43	39	48
130	(101) Ana	9	11	10
130	(110) Rut	47	44	46
260	(101) Ana	–	12	14
260	(110) Rut	51	49	51

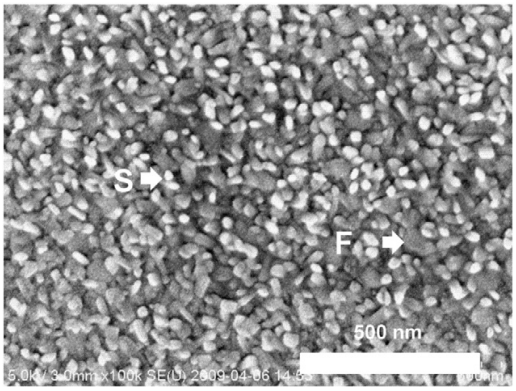

Fig. 2. SEM image of 15 nm thick doped A-series TiO_2 film. F and S indicate facetted and spherical grains, respectively.

for doped A, doped B, and undoped series. The survey spectrum of the film surface was taken for all three samples and the atom concentrations were evaluated. The possible effect of surface contamination was removed by sputtering the samples into 10 nm depth. The evaluations of peak shape were carried out on the unetched samples to ensure no change in chemical bonding due to sputtering. The nitrogen atom concentrations on the film surfaces were 0.4% for all samples. The concentration in the sputtered samples A, B, and undoped were 0.7%, 0.8%, and 0.9%, respectively. Subsequently within its resolution, the measurements using sputtering did not show evidence of nitrogen substitution. The N(1s) peaks for doped A-, B-, and undoped series are shown in Fig. 3a. There were no peaks at 396 eV which could be associated with nitrogen substituting for oxygen [31]. Instead peaks at higher energies can be found showing a broad peak within a range of 396–403 eV. Peaks within this area have been shown to indicate nitrogen doping by several researchers and they can be attributed to interstitial nitrogen [15,25,32–36]. Curve fitting was performed with a FWHM of 1.7 eV for all peaks in doped A and B and undoped samples. Doped A-sample showed peaks at 399.1 eV (larger peak 1) and 400.7 eV (peak 2), B-sample at 398.9 eV (larger peak 1) and 400.5 eV (peak 2), and undoped sample at 398.6 eV (peak 1) and 400.0 eV (larger peak 2). Saha and Tomkins [31] showed that the TiN peak is found at 397 eV. In the doped and undoped samples the binding energies are higher due to the high electronegativity of oxygen in TiO_2-structure [34]. Nevertheless it is visible that the dominating N(1s) peak in the doped samples is at lower binding energy than in the undoped sample. This may be seen as an evidence for nitrogen doping since peak close to 399 eV has been attributed to anionic N^- in O–Ti–N linkages [34]. Titanium Ti(2p) region is shown in Fig. 3b. Titanium peak Ti($2p_{3/2}$) appeared at 458.8 eV in all doped and undoped samples and is attributed to Ti^{4+} as in Ti(IV) oxide. In O(1s) region two peaks were found after deconvolution for doped and undoped samples (Fig. 3c). The dominating peak 1 was found at 529.9 eV for all samples representing lattice oxygen in TiO_2. A shoulder for peak 1 around 532 eV (peak 2) has been attributed to chemisorbed and hydrogen bonded surface water [36]. In the undoped sample the peak 2 was noticeable and located at 531.8 eV hence being an indication of chemisorbed water. In both doped A and doped B samples peak 2 was shallower and located at somewhat lower energies at 531.4 eV and 531.6 eV, respectively. To be precise there seems to be less chemisorbed water on the doped samples than on the undoped sample. The doping has apparently affected the hydrophilicity which is shown in the discussion for photoactivity. Carbon spectra for C(1s) are shown in Fig. 3d. The main peak for doped samples was at 286.1 eV and it seemed to be shifted from undoped main peak of 285.6 eV. The peak at 286.1 eV could be attributed to C–N–bonds but their formation within the TiO_2 film is unlikely since the level of carbon impurities was low in the deposition process. Other peaks for all doped and undoped films appear around 287 eV and 290 eV which may be ascribed to variable bonds between carbon and oxygen. However it is probable that the C(1s) peaks emerged due to surface contamination during the sample handling.

Table 2
Band gaps of the TiO_2 films from doped A-, doped B-, and undoped series.

Film thickness, nm	Band gap, eV		
	A	B	Undoped
2.6	3.7	3.7	3.7
5	3.7	3.7	3.7
10	3.7	3.7	3.7
15	3.7	3.6	3.7
30	3.6	3.5	3.6
65	3.5	3.7	3.4
130	3.3	3.3	3.3
260	3.1	3.1	3.2

The photoactivity of the films was measured with the water contact angle test. The thin films had been kept in storage in aluminum foils and polyethylene bags which protect the films from light. The films were irradiated with UV light instantly after taking them out of storage. The contact angles were measured immediately and after 15 and 30 min of irradiation. The results are shown in Fig. 4. A commercial product of Pilkington Activ™ glass was also tested (Fig. 4). In the doped A- and B-series the contact angle in the 15 nm anatase film reached a value of less than 10° already within 15 min of UV-irradiation; A-sample showing superhydrophilicity. In doped A-series the value of 15 nm film increased slightly within further irradiation. The increase may have been due to oxygen absorption that changes the surface characteristics of the film. The hydroxyl groups that are found to be active species in hydrophilicity [37] are less attracted to an oxidized surface making it more hydrophobic. The increase in contact angle was also seen with the films of 2.6 nm and 5 nm of doped A-, and B-series (not shown here). The SEM images showed (not presented here) that the films of 2.6 nm, 5 nm and 10 nm in doped A-series and 2.6 nm and 5 nm in doped B-series possessed spherical grains but they did not cover the whole film surface. This probably resulted in increased oxygen absorption within the films leading to lower hydrophilicity. The Activ™ film had been kept in darkness but not in the aluminum foil and had been freely exposed to air. This is most probably the reason why one could not see any effect of oxygen absorption and in 30 min the contact angle decreased down to 11° showing good photoactivity. It is noticeable that in the undoped series all the films had reasonably good photoactivity including the rutile dominated films. In the doped B-series only the anatase films showed a good photoactivity. In the A-series where the doping effect had been apparently higher, only the 15 nm anatase film had a good photoactivity. The XPS results indicated interstitial N-doping and the doped films possessed less chemisorbed water than the undoped film. Substitutional N-doping has been found to favor the formation of oxygen vacancies whereas interstitial doping may prevent it [38,39]. Oxygen vacancies create a hydrophilic surface since they dissociate water forming bridging hydroxyl groups on the TiO_2 surface [40]. In addition oxygen vacancies have been found to be more common on rutile than on anatase [41]. Therefore N-doping may have decreased the amount of oxygen vacancies especially in the anatase–rutile-mixture films. This might explain the clear decrease of hydrophilicity in the doped A- and B-series.

The majority carrier polarity of doped A- and B-series, and undoped series was measured by the hot probe test and the results are shown in

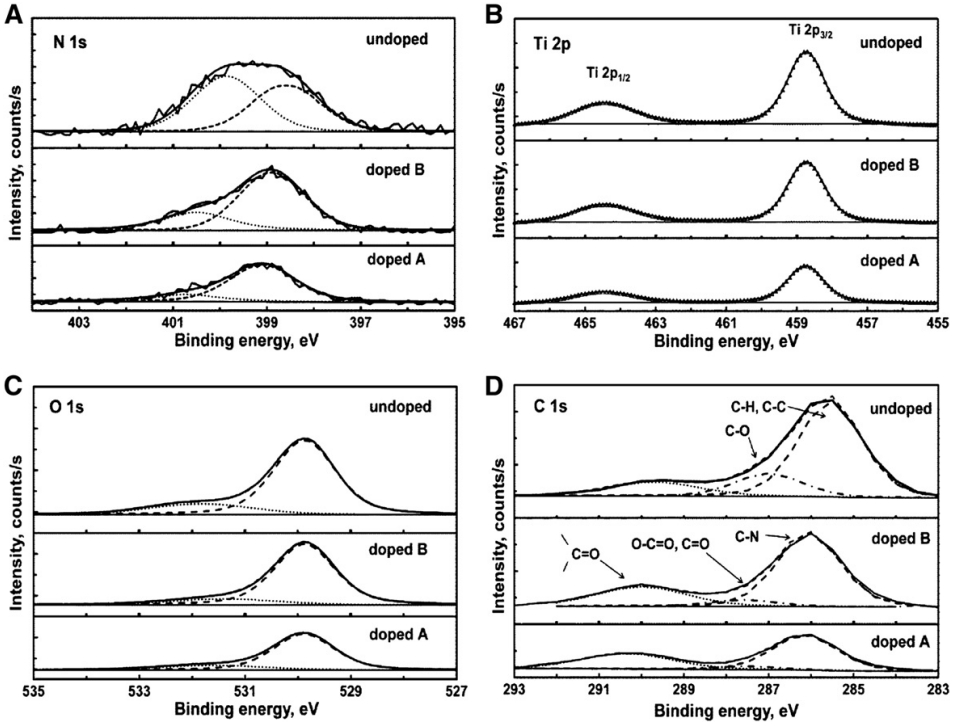

Fig. 3. Fitted XPS spectra for doped A-series, doped B-series, and undoped series 260 nm thick films.

Table 3. It can be seen that in all series the anatase dominant films are p-type and rutile dominant films are n-type. In our previous paper we reported parallel results and proposed a theory that p-type anatase or anatase dominant TiO_2 film is superior in hydrophilicity compared to n-type rutile TiO_2 due to larger number of holes in the structure [42]. Similarly this study shows that in all film series (p-type) anatase films possess higher photoactivity than (n-type) rutile.

The photocatalytic activity of the films was tested by the methylene blue (MB) degradation test. The test was run for 4 h. The effect of surface adsorption alone on reducing the MB concentration was tested in the dark by immersing the samples in the solution. The methylene blue concentration was not reduced during the test and therefore no significant adsorption had taken place. Fig. 5 shows the results for the photocatalytic activity for the series of doped A, doped B, and undoped TiO_2. The highest photocatalytic activity in all series is found with 15 nm thick film. Pilkington Activ™ performed quite well but the 15 nm and 30 nm thick films of series A degraded a higher amount of methylene blue. Recently Kääriäinen and Cameron [42] proposed that for a good photocatalytic performance TiO_2 needs p-type anatase phase and n-type rutile phase-structure to form p–n junctions which decrease the recombination of the electron–hole pairs. In Fig. 5 it is seen that in all series the anatase dominated film with a small amount of rutile produces the best photocatalytic activity. Therefore it can be concluded that the p–n junction works also in these doped A-, doped B-, and undoped series. The photocatalytic activity increased to 260% when comparing the doped A-series and undoped series. The A-series was doped with a higher feeding pressure of ammonium hydroxide than in B-series and this may explain why the B-series performed inferior to A-series.

Film resistivity was measured in order to find out about the electrical differences in films using a four-point-probe. The results are shown in Fig. 6. It can be seen that the undoped films possess the highest resistivity and the A series has the lowest resistivity. At very low film thicknesses of 2.6 nm to 10 nm the resistivity was very high and could not be evaluated. At higher thicknesses the resistivity decreases in all series as would be expected. The difference in resistivity is clear at a thickness of 260 nm where the resistivity is highest with the undoped sample and lowest with the doped A-series sample. Therefore it is clear that the nitrogen doping has increased the conductivity in A- and B-series. Furthermore higher electron (or hole) concentration in the TiO_2 may change the occupancy of trapping sites within the bandgap thus reducing the recombination of photogenerated electron–hole pairs. Together with the existence of p–n junctions, the longer lifetime of photoactivated carriers will lead more charge carriers reaching the surface of the crystals and enabling more oxidation–reduction events there.

4. Conclusions

A nitrogen doping trial of titanium dioxide was attempted by using ammonium hydroxide solution as a nitrogen and oxygen source in atomic layer deposition. The band gap evaluation showed a minor red shift for the thickest doped films. X-ray photoelectron spectroscopy analysis showed that interstitial nitrogen was found in the doped samples. The photoactivity was reduced especially in doped rutile dominated samples. However the doping improved the photocatalytic performance significantly. The film resistivity measurements demonstrated that the doped TiO_2 series had higher conductivity than the undoped TiO_2. The higher conductivity is most probably due to the nitrogen doping which provided an excess of negative charge carriers, particularly in the rutile films. According to hot probe test all the anatase or anatase dominant films were p-type and all the rutile dominant films were shown to be n-type. The best photocatalytic performance in all doped and undoped films took place with films that were anatase dominated containing a

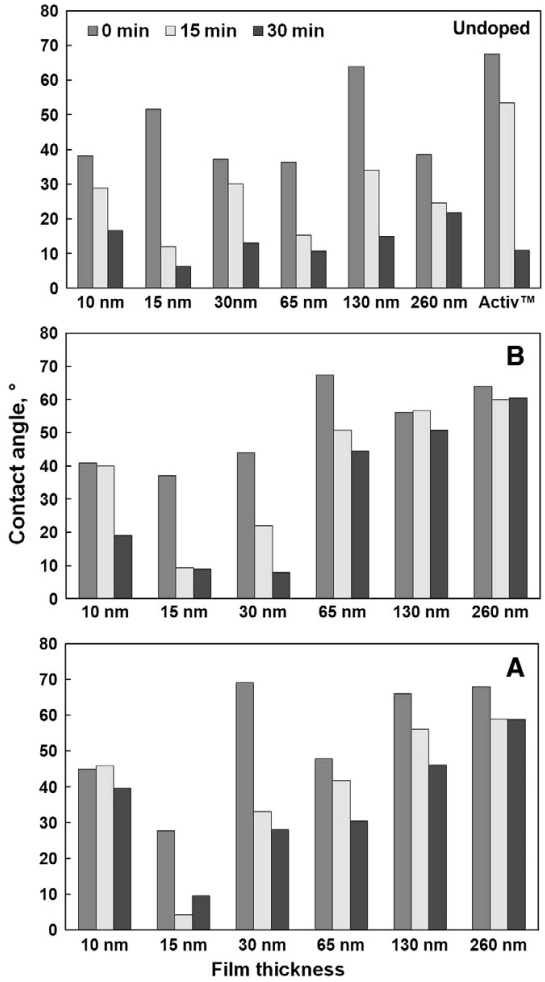

Fig. 4. Water contact angles of titanium dioxide thin films for doped A-series, doped B-series, and undoped series measured at 0 min, 15 min, and 30 min under UV-irradiation.

small amount of rutile. The reason may be the creation of p–n junctions which are formed of p-type anatase and n-type rutile which slow down the recombination effect. Together the doping effect and p–n junctions result in superior photocatalytic performance.

Acknowledgments

The authors thank ESR and the State Provincial Office of Eastern Finland for supporting the project under S10148. The authors thank also Mr. Markku Heinonen from the University of Turku, Department of Physics and Astronomy for performing the XPS characterization.

Table 3
Major carrier polarities of the TiO_2 films from doped A-, doped B-, and undoped series.

Film thickness, nm	Major carrier polarity		
	A	B	Undoped
15	p-Type	p-Type	p-Type
30	p-Type	p-Type	p-Type
65	p-Type	p-Type	p-Type
130	n-Type	n-Type	n-Type
260	n-Type	n-Type	n-Type

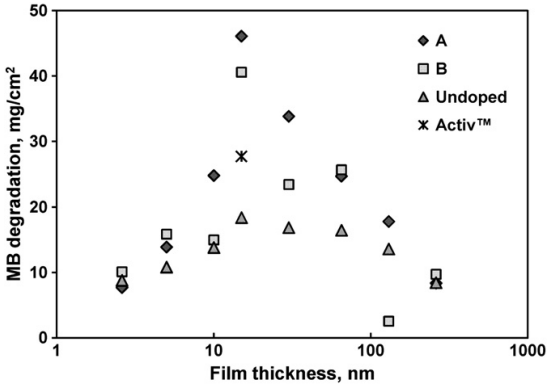

Fig. 5. Methylene blue degradation of doped A-series, doped B-series, and undoped series films.

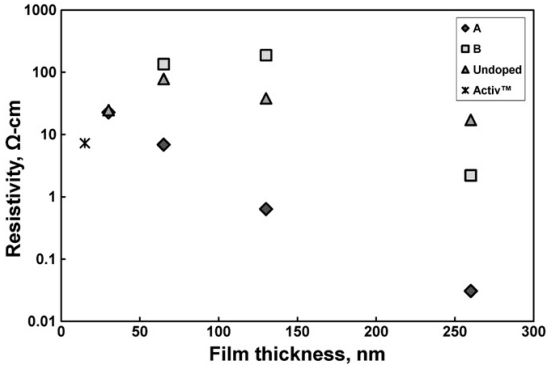

Fig. 6. Film resistivity of doped A-series, doped B-series, and undoped series films.

References

[1] X. Chen, S.S. Mao, Chem. Rev. 107 (2007) 2891.
[2] I.C. Ladiu, V. Danciu, V. Coşoveanu, A. Rustoiu-Csavdari, P. Lianos, Rev. Roum. Chim. 47 (2002) 1247.
[3] D. Buso, J. Pacifico, A. Martucci, P. Mulvaney, Adv. Funct. Mater. 17 (2007) 347.
[4] C.-S. Chi, J. Choi, Y. Jeong, O.Y. Lee, H.-J. Oh, Thin Solid Films 519 (2011) 4676.
[5] H. Yu, X.-J. Li, S.-J. Zheng, W. Xu, Mater. Chem. Phys. 97 (2006) 59.
[6] J. Yu, M. Zhou, H. Yu, Q. Zhang, Y. Yu, Mater. Chem. Phys. 95 (2006) 193.
[7] W. Zhang, Y. Li, S. Zhu, F. Wang, Catal. Today 93–95 (2004) 589.
[8] K.-J. Zhang, W. Xu, X.-J. Li, S.-J. Zheng, G. Xu, J.-H. Wang, Trans. Nonferrous Met. Soc. China 16 (2006) 1069.
[9] A.A. Ismail, D.W. Bahnemann, L. Robben, V. Yarovyi, M. Wark, Chem. Mater. 22 (2010) 108.
[10] H. Lin, H. Kozuka, T. Yoko, J. Sol–Gel Sci. Technol. 19 (2000) 529.
[11] Q. Xiao, Z. Si, J. Zhang, C. Xiao, Z. Yu, G. Qiu, J. Mater. Sci. 42 (2007) 9194.
[12] T. Lindgren, J.M. Mwabora, E. Avendaño, J. Jonsson, A. Hoel, C.-G. Granqvist, S.-E. Lindquist, J. Phys. Chem. B 107 (2003) 5709.
[13] F. Peng, L. Cai, L. Huang, H. Yu, H. Wang, J. Phys. Chem. Solids 69 (2008) 1657.
[14] M. Qiao, Q. Chen, S. Wu, J. Shen, J. Sol–Gel Sci. Technol. 55 (2010) 377.
[15] J.S. Jang, H.G. Kim, S.M. Ji, S.W. Bae, J.H. Jung, B.H. Shon, J.S. Lee, J. Solid State Chem. 179 (2006) 1067.
[16] S. Livraghi, M.R. Chierotti, E. Giamello, G. Magnacca, M.C. Paganini, G. Cappelletti, C.L. Bianchi, J. Phys. Chem. C 112 (2008) 17244.
[17] A. Trenczek-Zając, K. Kowalski, K. Zakrzewska, M. Radecka, Mater. Res. Bull. 44 (2009) 1547.
[18] H.-L. Qin, G.-B. Gu, S. Liu, Mater. Chem. Phys. 112 (2008) 346.
[19] D.J. Mowbray, J.I. Martinez, J.M. García Lastra, K.S. Thygesen, K.W. Jacobsen, J. Phys. Chem. C 113 (2009) 12301.
[20] K. Prabakar, T. Takahashi, T. Nezuka, K. Takahashi, T. Nakashima, Y. Kubota, A. Fujishima, Renew. Energy 33 (2008) 277.
[21] G. Hyett, M.A. Green, I.P. Parkin, J. Photochem. Photobiol. A Chem. 203 (2009) 199.

[22] Y. Kuroda, T. Mori, K. Yagi, N. Mkihata, Y. Kawahara, M. Nagao, S. Kittaka, Langmuir 21 (2005) 8026.
[23] N. Sato, M. Matsuda, M. Yoshinaga, T. Nakamura, S. Sato, A. Muramatsu, Top. Catal. 52 (2009) 1592.
[24] V. Pore, M. Heikkilä, M. Ritala, M. Leskelä, S. Areva, J. Photochem. Photobiol. A Chem. 177 (2006) 68.
[25] R. Asahi, T. Morikawa, T. Ohwaki, K. Aoki, Y. Taga, Science 293 (2001) 269.
[26] M.-L. Kääriäinen, T.O. Kääriäinen, D.C. Cameron, in: D.M. Mattox (Ed.), 50th Annual Technical Conference Proceedings, Society of Vacuum Coaters, Albuquerque, 2007, p. 335.
[27] R. Swanepoel, J. Phys. E Sci. Instrum. 16 (1983) 1214.
[28] M.-L. Kääriäinen, T.O. Kääriäinen, D.C. Cameron, Thin Solid Films 517 (2009) 6666.
[29] A. Mills, A. Lepre, N. Elliott, S. Phopal, I.P. Parkin, S.A. O'Neill, J. Photobiol. Photochem. A 160 (2003) 213.
[30] P. Chin, D.F. Ollis, Catal. Today 123 (2007) 177.
[31] N.C. Saha, H.G. Tompkins, J. Appl. Phys. 72 (1992) 3072.
[32] X. Chen, C. Burda, J. Phys. Chem. B 108 (2004).
[33] Y. Nosaka, M. Matsushita, J. Nishino, A.Y. Nosaka, Sci. Technol. Adv. Mater. 6 (2005) 143.
[34] Y. Cong, J. Zhang, F. Chen, M. Anpo, J. Phys. Chem. C 111 (2007) 6976.
[35] X. Zhou, F. Peng, H. Wang, H. Yu, J. Yang, Mater. Res. Bull. 46 (2011) 840.
[36] W. Zhang, J. Yang, Y. Luo, S. Monti, V. Carravetta, J. Chem. Phys. 129 (2008) 064703.
[37] M.R. Hoffmann, S.T. Martin, W. Choi, D.W. Bahnemann, Chem. Rev. 95 (1995) 69.
[38] C. Di Valentin, G. Pacchioni, S. Livraghi, E. Giamello, J. Phys. Chem. B 109 (2005) 11414.
[39] C. Di Valentin, E. Finazzi, G. Pacchioni, A. Selloni, S. Livraghi, M.C. Paganini, E. Giamello, Chem. Phys. 339 (2007) 44.
[40] R. Schaub, P. Thostrup, N. Lopez, E. Lægsgaard, I. Stensgaard, J.K. Nørskov, F. Besenbacher, Phys. Rev. Lett. 87 (2001) 266104.
[41] W. Hebenstreit, N. Ruzycki, G.S. Herman, Y. Gao, U. Diebold, Phys. Rev. B 62 (2000) R16334.
[42] M.-L. Kääriäinen, D.C. Cameron, Surf. Sci. 606 (2012) L22.

Paper V

Zinc release from atomic layer deposited zinc oxide thin films and its bactericidal effect on *Escherichia Coli*

M.-L. Kääriäinen, C.K.Weiss, S. Pütz, S. Ritz, D.C. Cameron, V. Mailänder, K. Landfester

Submitted manuscript

Zinc release from atomic layer deposited zinc oxide thin films and its bactericidal effect on *Escherichia Coli*

M.-L. Kääriäinen*[1], C. K. Weiss[2], S. Ritz[2], S. Pütz[2], D. C. Cameron[1], V. Mailänder[2,3], and K. Landfester[2]

[1]*ASTRaL, Lappeenranta University of Technology, Sammonkatu 12, FI-50130 Mikkeli, Finland*
*marja-leena.kaariainen@lut.fi, tel. +358 40 536 2585
[2]*Max Planck Institute for Polymer Research, Ackermannweg 10, D-55128 Mainz, Germany*
[3]*III. Medical Clinic, University Medicine of the Johannes-Gutenberg University Mainz, Langenbeckstr. 1, D-55131 Mainz, Germany*

Abstract

Zinc oxide films have been grown by atomic layer deposition (ALD) at different reaction temperatures and in various thicknesses. Zinc-ion release has been examined from the ZnO films in water and in phosphate buffered saline solution (PBS). Additionally, the bactericidal effect has been studied on *Escherichia Coli*. The thickness of the ZnO film or its crystal orientation did not affect the rate of dissolution. ALD grown aluminum oxide films were deposited on top of the ZnO films and they acted as an effective block effect against zinc dissolution. The bactericidal effect was not dependent on the film thickness but both 45 nm and 280 nm thick ZnO films significantly reduced bacterial attachment and growth in dark conditions by 99.7% and 99.5%, respectively. The results indicated that photoirradiation is not required for bactericidal effects and that the elution of zinc ions is probably responsible for the antibacterial properties of the ZnO films. The duration of the antibacterial effect of ZnO can be controlled by accurate control of the film thickness, which is a feature of ALD, and the onset of the antibacterial effect can be delayed by a time which can be adjusted by controlling the thickness of the Al_2O_3 blocking layer. This gives the possibility of obtaining complex antibacterial release profiles through a nanolaminate structure of these two materials.

Keywords: zinc oxide thin film; atomic layer deposition; zinc release, bactericidal zinc

1. Introduction

The field of zinc oxide (ZnO) thin films has been extensively studied and there are several methods such as reactive magnetron sputtering, electron beam evaporation, and chemical vapor deposition that have been used in their production [1-4]. During recent years, atomic layer deposition (ALD) has gained immense interest for producing metal oxides and a large number of studies have been conducted on ZnO, for example, [5-8]. ZnO in thin film form has been generally found to be an n-type semiconductor with a bandgap of about 3.3 eV, i.e. absorption begins near the UVA area.

ZnO thin films have a great variety of potential applications such as light emitting diodes (LEDs), laser diodes (LDs), solar cells, liquid crystal displays, thin film transistors, and gas sensors [8-12]. ZnO is also applicable to air and water purification and waste remediation [13] due to its photoactive and photocatalytic properties which make it similar in effect to titanium dioxide [7-10] with a bandgap of 3.2 eV (anatase). In addition ZnO is antibacterial and has already been studied for several decades in bactericidal tests [18-24], and orthopedic and dental clinical treatments [25-27]. A variety of ZnO nanostructures have been studied both in surface energy modifications, photocatalytic treatments, and bacteriocidal tests [28-31]. Although nanostructures such as powders have been found to be very efficient in use there are risks in their use of causing toxicological and environmental effects [32]. Thin films which are firmly attached to their supports (substrates) may be a good option for air and water purification and antibacterial purposes since they are easily removable from the location where they are utilized. Thin films may be also safer since they probably do not release nanoparticles from their surface.

ALD is a surface controlled gas phase chemical vapor deposition process where thin films can be deposited in a layer by layer manner [33]. The film growth in ALD is self-limiting, contributing several advantages. The thickness of the films can be controlled by the number of reaction cycles, thereby enabling the precise growth of ultra thin layers. ALD can be used to deposit stoichiometric films with large area uniformity and conformality even on complex surfaces with deformities. Layer-by-layer growth allows one to change the film composition abruptly after each step. This gives the possibility of depositing multicomponent films such as nanolaminates or mixed oxides.

In this article we have studied the zinc release from ALD -grown zinc oxide thin films which have been immersed in water or body fluid simulant. Zinc release has also been tested with ZnO films which have 5-15 nm of aluminum trioxide (Al_2O_3) deposited on top in order to control the zinc elution from the ZnO film. Al_2O_3 acts as a temporary blocking layer to prevent zinc eluting from the ZnO film. In addition, bactericidal tests have been conducted with ZnO thin films of different thicknesses.

2. Experimental

Zinc oxide films were grown by atomic layer deposition (ALD) using diethylzinc ($Zn(C_2H_5)_2$) (DEZ) and deionized water as precursors at reaction temperatures of 120 °C and 200 °C. The sequence of the deposition was: pulse (DEZ) – rinse (N_2) – pulse (H_2O) – rinse (N_2) with timings of 0.7–1.5–0.5–1.0 s. Different film thicknesses between 45 nm and 280 nm were deposited. An additional series of films at both temperatures was also created where aluminum trioxide (Al_2O_3) films of 5-15 nm were deposited on top of the ZnO films. Trimethylaluminum and deionized water were used at 220° C in Al_2O_3 deposition. Generated nitrogen of 99.999% purity was used as a carrier and purging gas (INMATEC IMT-PN 1150, INMATEC GaseTechnologie GmbH & Co.KG). The deposition was carried out in a TFS-500 ALD reactor (Beneq Oy) at 5×10^2 - 1×10^3 Pa pressure. The precursors were kept at 20 °C during the deposition. The film thicknesses were measured with a spectroscopic ellipsometer M-2000FI from J.A.Woollam Co., Inc. on co-deposited samples on polished silicon substrates. The structure and crystalline phases of the films were examined by X-ray diffractometry (XRD) (Phillips X'Pert) using CuKα radiation (λ=1.54Å). The XRD patterns were acquired with a glancing angle of 0.2° for the incident beam for a range 2Θ=25–60° with a step size of 0.02° and with Bragg-Brentano geometry. Morphology was studied with a Hitachi S4800 field emission scanning electron microscope (SEM). Zinc release from zinc oxide films was studied by immersing the samples in deionized water and phosphate buffered saline solution (PBS) which is commonly used as body fluid simulant in biological studies. The ZnO films were placed in closed plastic containers and immersed in 5 ml of liquid. The samples were kept in dim light for 24 h and the films were removed from the liquid. The same procedure was performed for blank borosilicate samples in order to provide control samples for the measurement. In the long test series, the films were kept in 10 ml water or PBS. Solution containing the eluted material was collected for analysis every 24 hrs and the sample

was immersed in fresh solution. The test was continued for 38 days. The zinc release was analyzed from the elute-containing solution with inductively coupled plasma mass spectrometry (ICP-OES) using an ACTIVA M spectrometer from Horiba Jobin Yvon.

Antimicrobial activity test (non-growing conditions): as ZnO is a photocatalytic semiconductor, bactericidal tests were performed in the dark to separate the photocatalytic from the chemical Zn release -effect. A fresh shake culture of *Escherichia coli* (*E.coli* K-12 wildtype, K-12 DSM 498, ATCC 23716) was prepared in sterile LB medium by shaking at 37 °C and 200 rpm for 18 h. An exponential growing culture was obtained by dilution with sterile LB medium to an absorbance of 0.1 at 600 nm and shaking to an absorbance of 0.5 at 600 nm which correspond to a concentration of 1.0 x 10^8 CFU mL^{-1} (determined by plating and counting of serial dilutions). The bacteria solutions were further adjusted with KH_2PO_4 buffer (0.3 mM, pH 7.2, sterile) to ~2.5 x 10^5 CFU mL^{-1}. ZnO films (triplicate, 2.5 x 2.5 cm, 6.25 cm^2) were submerged in 7 mL bacteria dilution. Uncoated borosilicate glass (2.5 x 2.5 cm, 6.25 cm^2) served as control surfaces. Samples were incubated on a horizontal shaker (Innova 44, New Brunswick Scientific) at 37 °C and 150 rpm for 1 h. The bacteria concentration were determined at time T_0 and T_{1h} by serial dilutions in saline (undiluted, 1:25, 1:125), plating of an 50 µL aliquot on agar plates and incubation for 24 h at 37 °C to give an estimate of viable cell count as CFU mL^{-1}. The mean value and standard deviation (SD) was calculated from the serial dilutions of each sample). The percent of bacterial reduction was calculated from treated sample (A) directly compared to untreated control (B) at T_{1h} where reduction is defined by *R*, % (CFU mL^{-1}) = ($B_{CFU\ mL^{-1}} - A_{CFU\ mL^{-1}}$)/$B_{CFU\ mL^{-1}}$ x 100.

Bacterial attachment: a fresh shake culture of *E.coli* was prepared as described above and the bacteria were diluted with minimal LB medium to 1.5 x 10^6 CFU mL^{-1}. Samples (2.5 cm x 2.5 cm, 6.25 cm^2) and silicon wafer control were placed in a 6-well culture plate (Greiner, Germany) and submerged with 2 mL bacteria dilution, covered with a lid, sealed with parafilm and incubated on a horizontal shaker (Innova 44, New Brunswick Scientific) at 37 °C for 24 h. Then the samples were placed in a fresh 6 well culture plate and washed 4 times with saline. Bacteria attaching to the films were stained with Live/Dead BacLight Bacterial Viability Kit (Life Technologies, Germany) according to the supplier's protocol. The bacteria were imaged on an inverted microscope (Olympus IX-70) equipped with a 100 W mercury lamp, a 20x phase contrast objective and a CCD camera (F-View, Olympus) for digital imaging. Living bacteria stained with SYTO 9 (green) were excited with a band pass filter at

470 nm to 490 nm and the emission was detected by 520 nm. Dead bacteria cells stained with propidium iodide were excited with a band pass filter at 530 – 550 nm and the emission was detected by 590 nm. Image processing performed with CellSens Dimensions 1.5 (Olympus) and ImageJ (Fiji).

3. Results and Discussion

ZnO thin films with various thicknesses were deposited by ALD at reaction temperatures of 120 °C and 200 °C. Figure 1 shows the X-ray diffractograms of the ZnO films.

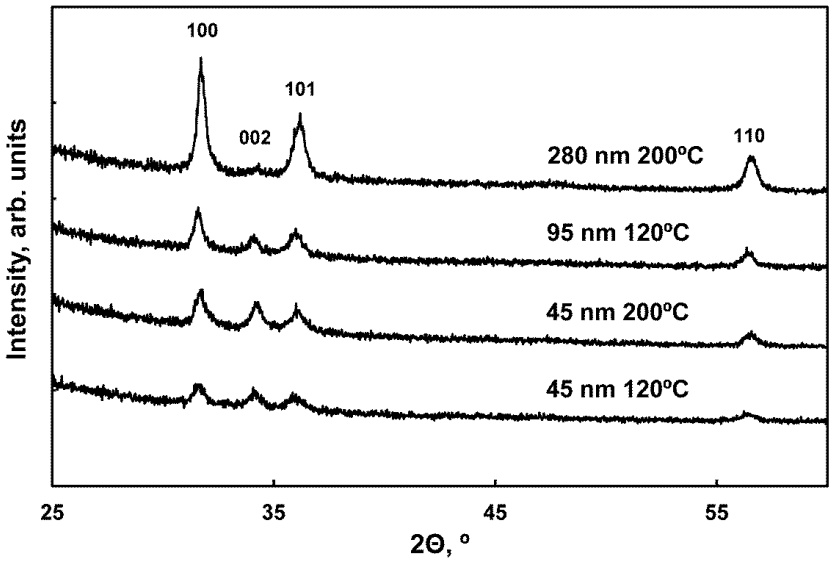

Figure 1. X-ray diffraction spectra using a glancing angle for zinc oxide with various thicknesses deposited at 120 °C and 200 °C.

Using a glancing angle of 0.2°, the crystal structure of ZnO was found to be the hexagonal, wurtzite phase. The ZnO films were polycrystalline and the dominating peak was (100) but also (002), (101), and (110) orientations were found in all the films. The XRD patterns were also acquired with Bragg-Brentano geometry and the results showed the same trend with (100) being the strongest peak (not presented here). In contrast to these results studies have

shown that (002) is the thermodynamically most stable surface (002) and it has been the most common in the ALD grown ZnO films over a range of temperatures (130-300°C) and substrates (glass, Si (001), sapphire (0001)) [7, 34-37]. The evolution of the peak height suggests that the crystals are randomly oriented in the initial growth stages but as film thickness increases there are few (002) planes parallel to the substrate (or indeed at an angle to diffract the glancing angle beam).

ZnO films prepared at both deposition temperatures were used in 24 h dissolution tests. ZnO films were immersed in both water and PBS solutions. The results are shown in Figure 2. The uncertainty of ICP-OES measurements was calculated by measuring the Zn signal using uncoated borosilicate samples in both water and PBS systems. These measurements gave a baseline of 0.028 mg L^{-1} in water and 0.021 mg L^{-1} in PBS solution. Based on Figure 2, zinc dissolution in the PBS buffer is low. It is likely that $Zn_3(PO_4)_3$ is generated with the phosphate from PBS. Zinc phosphate has a low solubility leading to a limit in the measurable concentration of Zn^{2+} in the supernatant. However, calculation of the maximum possible zinc concentration based on the phosphate concentration show that the maximum concentration is much higher than the measured values which can then be taken to be proportional to the true concentration of eluted zinc. The dissolution in water seems to show a bigger variation between the samples. However, allowing for measurement uncertainty, there is no clear trend in the data to suggest that the elution rate is dependent on film thickness.

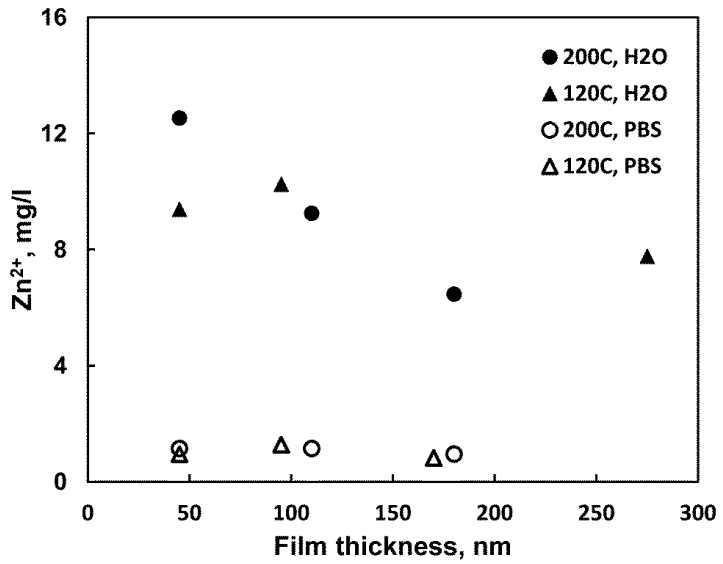

Figure 2. Zinc ion concentration in the supernatant after 24 h from various ALD grown ZnO films in water and PBS solution measured by ICP-OES.

ALD grown ZnO films of 45 nm thickness were further coated with Al_2O_3 ALD films in order to study the blocking effect of the overlayer on the zinc release. Three different thicknesses of 5 nm, 10 nm, and 15 nm of Al_2O_3 were deposited on the 45 nm ZnO films. The aluminum release was also measured by ICP-OES but the results showed no measurable aluminum dissolution in either water or PBS solution. Considering the density of ZnO of 5.7 g/cm^3 (the value for bulk material) and the area of the thin film sample (25 cm^2) zinc mass release was converted into a decrease in the ZnO film thickness. The accumulated decrease in the thickness of ZnO films with various Al_2O_3 coatings for each sampling day is presented in Figures 3 (water solution) and 4 (PBS solution).

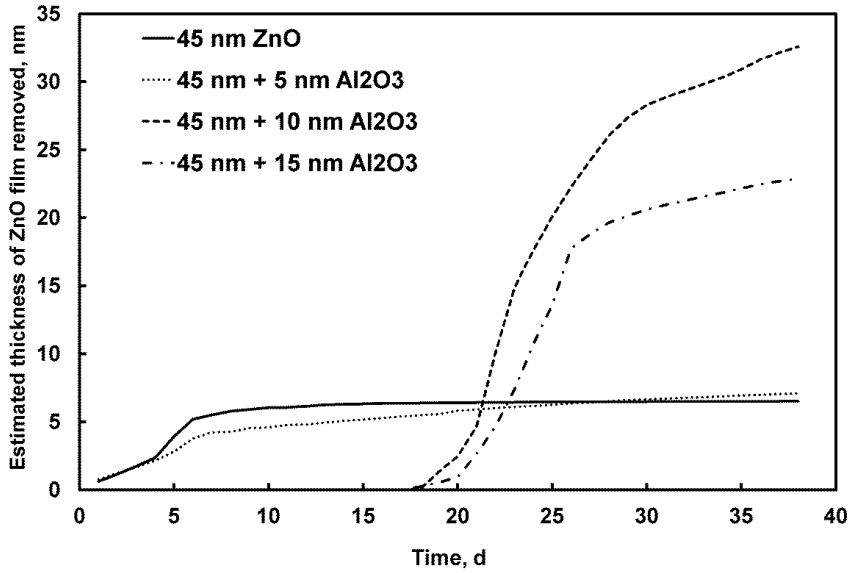

Figure 3. The decrease in ZnO film thickness during the long test in deionized water.

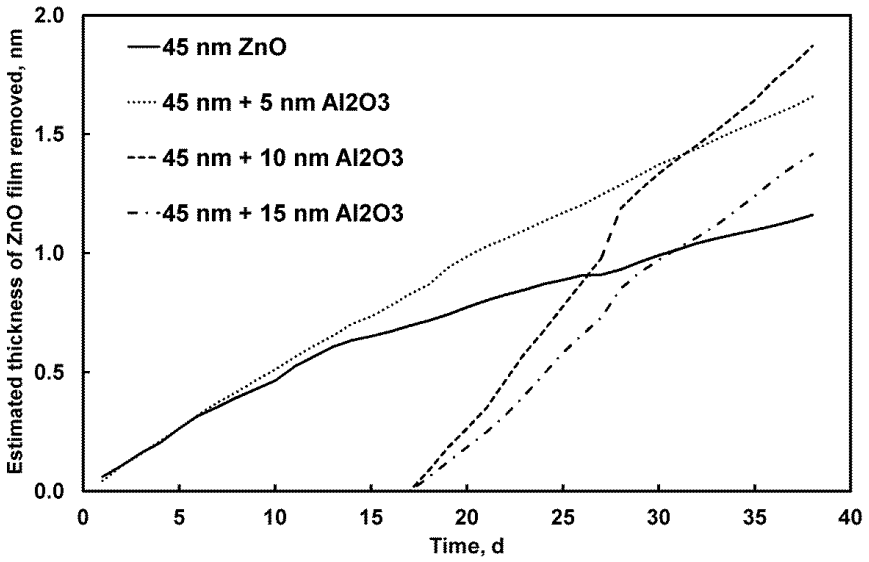

Figure 4. The decrease in ZnO film thickness during the long test in PBS solution.

In Figure 3, a plateau shows that the rate of elution has decreased almost to zero at approximately 10 days for the uncoated ZnO. The film with the 5 nm Al_2O_3 blocking layer initially shows a similar rate of elution but then there is a reduced rate and the amount of eluted material slowly increases up to the end of the test. As discussed below, it is likely that the 5 nm Al_2O_3 film does not produce complete conformal coverage of the underlying zinc oxide thus the zinc oxide is immediately exposed to the solution at certain points on immersion. The blocking effect becomes clear with 10 nm and 15 nm Al_2O_3 coatings. The zinc release is blocked for 18 days after which the release is much bigger than with plain ZnO film. In 35 days 30 nm of the ZnO film with 10 nm Al_2O_3 is gone and 20 nm is gone from the ZnO with 15 nm Al_2O_3 film. The measurements of the amount of zinc eluted are subject to the experimental uncertainty as mentioned above so the difference in the total amount eluted for the 10 nm and 15 nm blocking layers may not be completely reliable. The rate of zinc release is much faster for the aluminium oxide-coated films compared with the uncoated ones. This may be due to some complex behavior where both ions are involved. In Figure 4 the release rates into PBS are lower than in the water tests which agrees with the results of Figure 2. In all cases, the zinc is eluted at approximately a constant rate once the blocking layer becomes ineffective but in this case a plateau is not reached. After 35 days 1.0-1.8 nm of the ZnO films is gone. As mentioned earlier the low zinc concentrations may be partly due to the formation of zinc phosphates which cannot be detected as zinc in ICP-OES. As for Figure 3, the elution rate is faster where there is a thicker aluminium oxide blocking layer. It is interesting and important to note that the blocking effect of the aluminium oxide layer on the zinc release ends around the same day in both water and PBS solution. It is clear, therefore, that the duration of an antibacterial effect can be controlled by the thickness of the deposited film and moreover that the deposition of a blocking layer on top of the zinc oxide can be used to control the onset of any antibacterial effect. Allowing for experimental uncertainty, there may be little difference between the elution rates for the uncoated/5 nm coated film pair and also between the 10/15 nm coated film pair. If we consider that the 5 nm film may have some thin areas or pinholes due to particle contamination of the substrate before growth then the ZnO will be exposed in both samples immediately. However, for the film with the 5 nm blocking layer, the dissolution rate is somewhat slowed by the restriction in the rate of diffusion of the solution towards the ZnO and also the rate of diffusion of the Zn ions away from the ZnO.

A scanning electron microscopy (SEM) image of the 110 nm thick film deposited at 200 ºC is presented in Figure 5. The image on the left shows original polycrystalline ZnO film before the dissolution test. The image in the middle and on the right shows the 110 nm ZnO film

after 24 h immersion in deionized water and PBS solution, respectively. The immersion in water seems to have dissolved the ZnO surface more evenly than PBS solution. The image of immersion in PBS solution shows holes as if certain crystals have been dissolved or removed whereas others still remain attached.

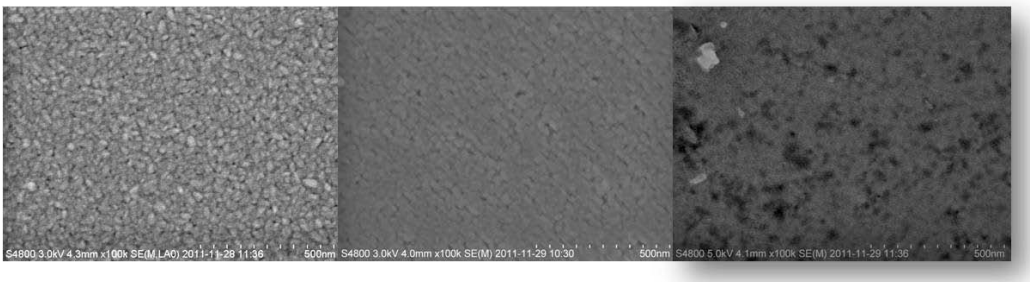

Figure 5. SEM images of 110 nm ZnO film before 24 h immersion (left), after immersion in deionized water, and after immersion in PBS-solution.

Investigation of biofilm formation to test the non-specific binding of *E.coli* was performed on ZnO films of 45 nm and 280 nm thicknesses. The surfaces were incubated with ~ 3 x 10^6 CFUs of *E.coli* for 24 h, washed and stained with dyes for living (Syto9, green) and dead (propidium iodide, red) cells. Figure 6 shows exemplary the remaining bacteria on the films and indicate a general reduction of *E.coli* attachment on ZnO surfaces produced by ALD, independent of the thickness.

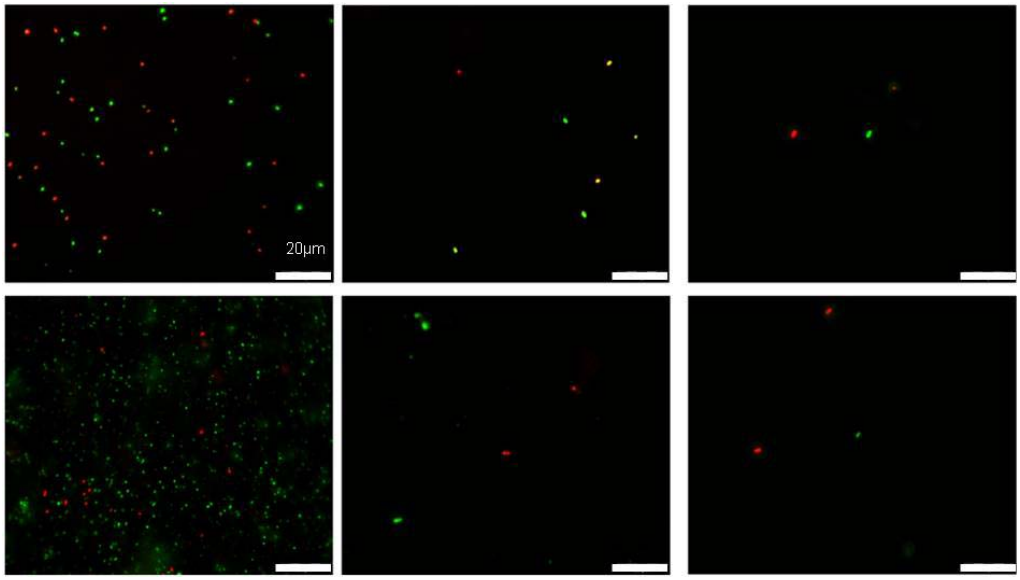

Figure 6. Biofilm formation of *E.coli* on ZnO films of 45 nm (right column), 280 nm (middle column), and borosilicate glass control (left column). Samples were submersed with *E.coli* suspension ($1.25x10^6$) in minimal LB-medium for 24 h in the dark. Bacteria were stained with fluorescent dyes discriminating between live (green) and dead (read) bacteria. Scale bar is 20 µm.

Antimicrobial activity was studied by an adapted version of a Standard Test Method for Determining the Antimicrobial Activity of Immobilized Antimicrobial Agents under Dynamic Contact Conditions (E2149-10; ASTM International). Two zinc oxide films with a thickness of 45 nm and 280 nm from 200 °C series and a borosilicate glass control were subjected to orbital rotation (200 rpm) for 1 h submerged in buffer solutions containing *E.coli* (K12, strain 498, DSMZ) concentrations of ~ 2.5 x 10^5 colony forming units (CFU) per mL at 37 °C. Using buffer solution instead of growth medium provides metabolic stasis of the population and prevents the overlay with the growth phase of the bacteria (and therefore reduces the variability). The resultant solutions spread on agar plates are shown in the Figure 7.

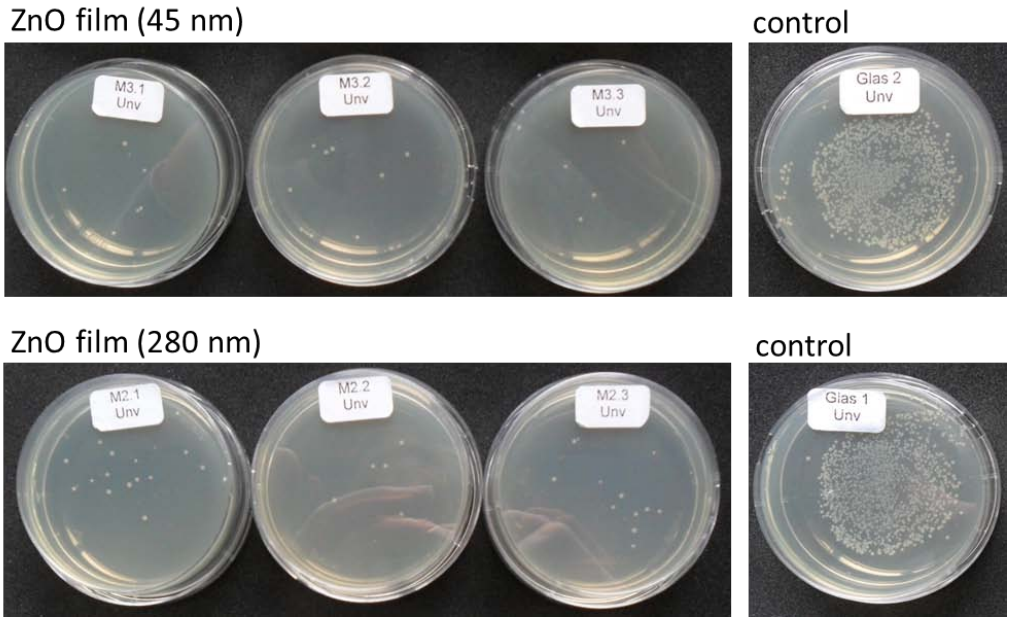

Figure 7. Antimicrobial activity of ZnO films. Images showing *E.coli* colonies (CFUs, colony forming units) on agar plates which have been in contact with ZnO films (45 nm and 280 nm) and borosilicate glass control for 24 h in the dark.

The calculated bacterial reduction for 45 nm and 280 nm ZnO film was R = 99.7% and 99.5%, respectively. The difference in the antibacterial performance of the two different films was not significant. Considering that the antibacterial tests were performed in the dark, antibacterial activity of the ZnO films due to photocatalytic effects can be excluded. The bactericidal effect must therefore arise from the ZnO film material and structure itself. Zn^{2+} ions have previously been found to produce an antibacterial effect [20,21]. Other studies have shown that the elution of Zn^{2+} has been enhanced under acidic conditions and in the presence of biological components such as amino acids and peptides [19]. The antibacterial tests showed no dependence of efficacy on film thickness. This is consistently supported by the ICP-OES analysis which shows similar concentrations of hydrated Zn^{2+} ions for the 45 nm and 280 nm films.

4. Conclusions

Zinc ion release from ALD grown ZnO films and its bactericidal effect on *E.coli* have been investigated. ZnO films were deposited in two different reaction temperatures and with various thicknesses. There was no evidence found that the film thickness or ZnO crystal orientation would affect the dissolution of zinc from ZnO films. Aluminum oxide showed an effective blocking effect; a layer of only 10 nm blocked the zinc release for 18 days in water and 16 days in PBS. Hence it may be used as a controller for zinc release. Both 45 nm and 280 nm thick ZnO films proved to be highly efficient in antibacterial efficiency and destroyed *E. coli* by 99.7% and 99.5%, respectively. The zinc ions rather than photocatalytically generated species are responsible for the antibacterial effect. A combination of controlled ZnO and Al_2O_3 thin films can be used to design a time sequence of antibacterial activity where the onset of the activity can be delayed by the thickness of the Al_2O_3 layer. This also indicates that a multilayer nanolaminate structure of alternating ZnO and Al_2O_3 films could be used to tailor a complex sequence of high and low antibacterial activity which would be useful in medical applications.

Acknowledgements

We want to thank Carolin Hogl for expert technical assistance. The authors thank ESR and the State Provincial Office of Eastern Finland for supporting the project under S10148 and also project 245500 Bacteriosafe funded by the EU under Framework 7.

References

[1] T. Minami, T. Miyata, T. Yamamoto, H. Toda, J. Vac. Sci. Technol., A 18 (2000) 1584.

[2] Y. Kashiwaba, K. Sugawara, K. Haga, H. Watanabe, B.P. Zhang, Y. Segawa, Thin Solid Films 411 (2002) 87.

[3] E. Fortunato, P. Barquinha, A. Pimentel, A. Gonçalves, A. Marques, L. Pereira, R. Martins, Thin Solid Films 487 (2005) 205.

[4] H. Cheng, C. Chen, C. Lee, Thin Solid Films 498 (2006) 142.

[5] A.W. Ott, R.P.H. Chang, Mater. Chem. Phys. 58 (1999) 132.

[6] E.B. Yousfi, J. Fouashe, D. Lincot, Appl. Surf. Sci. 153 (2000) 223.

[7] S.K. Kim, C.S. Hwang, S.-H. K. Park, S.J.Yun, Thin Solid Films 478 (2005) 103.

[8] S. J. Lim, S.-J. Kwon, H. Kim, J.-S. Park, Appl. Phys. Lett. 91 (2007) 183.

[9] Ü. Özgür, Ya.I. Alivov, C. Liu, A. Teke, M.A. Reshchikov, S. Doğan, V. Avrutin, S.-J. Cho, H. Morkoç, J. Appl. Phys. 98 (2005) 041301.

[10] D. Banerjee, J.Y. Lao, D.Z.Wang, J.Y. Huang, Z.F. Ren, D. Steeves, B. Kimball,M. Sennett, Appl. Phys. Lett. 83 (2003) 2061.

[11] A. Karuppasamy, A. Subrahmanyam, Mater. Lett. 61 (2007) 1256.

[12] S.J. Pearton, D.P. Norton, K. Ip, Y.W. Heo, T. Steiner, Prog. Mater. Sci. 50 (2005) 293.

[13] S.A. Ruffolo , M.F. La Russa , M. Malagodi, C.O. Rossi, A.M. Palermo, G.M. Crisci Appl Phys A 100 (2010) 829.

[14] M.-L. Kääriäinen, T.O. Kääriäinen, D.C. Cameron, Thin Solid Films 517 (2009) 6666.

[15] M.-L. Kääriäinen, D.C. Cameron Surface Science 606 (2012) L22.

[16] M.-L. Kääriäinen, D.C. Cameron Thin Solid Films 526 (2012) 212.

[17] R. Schiller, C.K. Weiss, K. Landfester, Nanotechnology 21 (2010) 405603.

[18] H. Babich and G. Stotzky Appl. Environ. Microb. Dec. 1978, p. 906.

[19] J.W. Moreau, P.K. Weber, M.C. Martin, B. Gilbert, I.D. Hutcheon, J.F. Banfield, Science 316 (2007) 1600.

[20] N.M Franklin, N.J. Rogers, S.C. Apte, G.E. Batley, G.E. Gadd, P.S. Casey, Environ. Sci. Technol. 41 (2007) 8484.

[21] T. Xia, M. Kovochich, M. Liong, L. Madler, B. Gilbert, H. Shi, J.I. Yeh, J.I. Zink, A.E. Nel, ACS Nano 2 (2008) 2121.

[22] J. Sawai, J Microbiol. Methods 54 (2003) 177.

[23] Y. Liu, L. He, A. Mustapha, H. Li, Z.Q. Hu, M. Lin, J. Appl. Microbiol. 107 (2009) 1193.

[24] Z. Huang, X. Zheng, D. Yan, G. Yin, X. Liao, Y. Kang, Y. Yao, D. Huang, B. Hao, Langmuir 24 (2008) 4140.

[25] W.R. Moore, J.M. Genet, Oral Surgery 53 (1982) 508.

[26] W. Geurtsen, G. Leyhausen, Clin. Oral Invest. 1 (1997) 5.

[27] Y.-Y.Chang, C.-H. Lai, J.-T. Hsu, C.-H. Tang, W.-C. Liao, H.-L. Huang, Clin. Oral Invest. Jan (2011), DOI 10.1007/s00784-010-0504-9

[28] K. Mcguire, Z.W. Pan, Z.L. Wang, D. Milkie, J. Menéndez, A.M. Raoa, J. Nanosci. Nanotech. 2 (2002) No. 5.

[29] O. Akhavan, M. Mehrabian, K. Mirabbaszadeh, R. Azimirad, J. Phys. D: Appl. Phys. 42 (2009) 225305.

[30] L. Wang, Y. Zheng, X. Li, W. Dong, W. Tang, B. Chen, C. Li, X. Li, T. Zhang, W. Xu, Thin Solid Films 519 (2011) 5673.

[31] J. Li, X. Liu, Y. Ye, H. Zhou, J. Chen, Colloid. Surface. A (2011) 109.

[32] C. Buzea, I.I. Pacheco Blandino, K. Robbie, Biointerphases 2 (2007) MR17.

[33] M. Ritala, M. Leskelä, in: H.S. Nalwa (Ed.), Handbook of Thin Film Materials, vol. 1, Academic Press, New York, 2002, p. 103.

[34] J. Lim, C. Lee, J. Alloys Compd. 449 (2008) 371.

[35] S.J. Lim, S. Kwon, H. Kim, Thin Solid Films 516 (2008) 1523.

[36] E. Guziewicz, M. Godlewski, T.A. Krajewski, Ł. Wachnicki, G. Łuka, W. Paszkowicz, J.Z. Domagała, E. Przezdziecka, E. Łusakowska, B.S. Witkowski, Acta Phys. Pol. A116 (2009) 814.

[37] E. Guziewicz, M. Godlewski, T.A. Krajewsk, Ł. Wachnicki, G. Łuka, J.Z. Domagała, W. Paszkowicz. B.J. Kowalski, B.S. Witkowski, A. Dużyńska2, A. SuchockiPhys. Stat. Solid. B 247 (2010) No. 7.

ACTA UNIVERSITATIS LAPPEENRANTAENSIS

479. OYOMNO, WERE. Usable privacy preservation in mobile electronic personality. 2012. Diss.

480. LINNALA, MIKKO. Simulation and optimization tools in paper machine concept design. 2012. Diss.

481. KORPIJÄRVI, JUHA. Aging based maintenance and reinvestment scheduling of electric distribution network. 2012. Diss.

482. KORHONEN, JUHAMATTI. Active inverter output filtering methods. 2012. Diss.

483. KLODOWSKI, ADAM. Flexible multibody approach in bone strain estimation during physical activity: quantifying osteogenic potential. 2012. Diss.

484. VUORENMAA, MARKKU. Osaamisen johtaminen pk-yrityksen kansainvälisen kasvun elinkaarella. 2012. Diss.

485. RAUTIAINEN, MARITA. Dynamic ownership in family business systems – a portfolio business approach. 2012. Diss.

486. LILIUS, REIJO. THE FINNISH IT INDUSTRIES IN TRANSITION Defining and measuring the Finnish software product and IT services industries by applying theoretical frameworks . 2012. Diss.

487. TUOMINEN, PASI. The purpose of consumer co-operation: implications for the management and governance of co-operatives. 2012. Diss.

488. SAARI, ESA. Suurnopeus-turbokoneroottoreiden termodynaaminen ja mekaaninen mallinnus sekä rakenneanalyysi. 2012. Diss.

489. PAANANEN, MIKKO. On innovative search: the use of internal and external sources of innovation among Finnish innovators. 2012. Diss.

490. BELOVA, POLINA. Quasiclassical approach to the vortex state in iron-based superconductors. 2012. Diss.

491. HIETANEN, IIRO. Design and characterization of large area position sensitive radiation detectors. 2012. Diss.

492. PÄSSILÄ, ANNE. A reflexive model of research-based theatre Processing innovation of the cross-road of theatre, reflection and practice-based innovation activities. 2012. Diss.

493. RIIPINEN, TOMI. Modeling and control of the power conversion unit in a solid oxide fuel cell environment. 2012. Diss.

494. RANTALAINEN, TUOMAS. Simulation of structural stress history based on dynamic analysis. 2012. Diss.

495. SALMIMIES, RIINA. Acidic dissolution of iron oxides and regeneration of a ceramic filter medium. 2012. Diss.

496. VAUTERIN, JOHANNA JULIA. The demand for global student talent: Capitalizing on the value of university-industry collaboration. 2012. Diss.

497. RILLA, MARKO. Design of salient pole PM synchronous machines for a vehicle traction application. 2012. Diss.

498. FEDOROVA, ELENA. Interdependence of emerging Eastern European stock markets. 2012. Diss.

499. SHAH, SRUJAL. Analysis and validation of space averaged drag model for numerical simulations of gas-solid flows in fluidized beds. 2012. Diss.

500. WANG, YONGBO. Novel methods for error modeling and parameter identification of redundant hybrid serial-parallel robot. 2012. Diss.

501. MAXIMOV, ALEXANDER. Theoretical analysis and numerical simulation of spectral radiative properties of combustion gases in oxy/air-fired combustion systems. 2012. Diss.

502. KUTVONEN, ANTERO. Strategic external deployment of intellectual assets. 2012. Diss.

503. VÄISÄNEN, VESA. Performance and scalability of isolated DC-DC converter topologies in low voltage, high current applications. 2012. Diss.

504. IKONEN, MIKA. Power cycling lifetime estimation of IGBT power modules based on chip temperature modeling. 2012. Diss.

505. LEIVO, TIMO. Pricing anomalies in the Finnish stock market. 2012. Diss.

506. NISKANEN, ANTTI. Landfill gas management as engineered landfills – Estimation and mitigation of environmental aspects. 2012. Diss.

507. QIU, FENG. Surface transformation hardening of carbon steel with high power fiber laser. 2012. Diss.

508. SMIRNOV, ALEXANDER. AMB system for high-speed motors using automatic commissioning. 2012. Diss.

509. ESKELINEN, HARRI, ed. Advanced approaches to analytical and systematic DFMA analysis. 2013.

510. RYYNÄNEN, HARRI. From network pictures to network insight in solution business – the role of internal communication. 2013. Diss.

511. JÄRVI, KATI. Ecosystem architecture design: endogenous and exogenous structural properties. 2013. Diss.

512. PIILI, HEIDI. Characterisation of laser beam and paper material interaction. 2013. Diss.

513. MONTO, SARI. Towards inter-organizational working capital management. 2013. Diss.

514. PIRINEN, MARKKU. The effects of welding heat input usability of high strength steels in welded structures. 2013. Diss.

515. SARKKINEN, MINNA. Strategic innovation management based on three dimensions diagnosing innovation development needs in a peripheral region. 2013. Diss.

516. MAGLYAS, ANDREY. Overcoming the complexity of software product management. 2013. Diss.

517. MOISIO, SAMI. A soft contact collision method for real-time simulation of triangularized geometries in multibody dynamics. 2013. Diss.

518. IMMONEN, PAULA. Energy efficiency of a diesel-electric mobile working machine. 2013. Diss.

519. ELORANTA, LEENA. Innovation in a non-formal adult education organisation – multi-case study in four education centres. 2013. Diss.

520. ZAKHARCHUK, IVAN. Manifestation of the pairing symmetry in the vortex core structure in iron-based superconductors. 2013. Diss.